

Chapter 1

Introduction

William A. Imbriale, John Huang, and Mark S. Gatti

Spaceborne Antennas for Planetary Exploration traces the development of the antennas used on JPL Spacecraft from their inception on the very first United States Explorer Mission in 1958 to the present. To completely cover all types of spacecraft antennas would be a daunting task indeed, and is not the intent of this monograph. Rather, the focus is only on antennas that have flown on Jet Propulsion Laboratory (JPL) spacecraft or were used for JPL scientific instruments that have flown on other spacecraft. The monograph primarily deals with the RF design and performance of the antennas and associated front-end equipment, but it also includes a chapter on mechanical development. It describes all the new designs and technological innovations introduced by JPL. There is also a thorough treatment of all the analytical and measurement techniques used in the design and performance assessment. This monograph can serve as an introduction to newcomers in the field or a reference for the advanced practitioner. The technical terms in the text assume that the reader is familiar with basic engineering and mathematical concepts including material typically found in a senior-level course in electromagnetics.

This book is complementary to [1], which describes the JPL ground network antennas. However, whereas the ground antennas are primarily for telecommunication, the antennas on spacecraft can serve the dual purpose of a science instrument and/or a means of communicating the science and telemetry data to Earth. JPL's support of the National Aeronautics and Space Administration (NASA) space program has several distinct eras. The very first mission was an Earth orbiter, quickly followed by unmanned exploration of the Moon in preparation for NASA manned flight to the Moon. Missions to the

Moon included the Ranger series that captured pictures of the surface as it flew into the Moon, and the Surveyor spacecraft that successfully landed on the surface of the Moon. The first interplanetary spacecraft were flybys, initially targeting the inner planets of Venus, Mercury, and Mars. The flyby era concluded with the “Grand Tour” Voyager Mission that flew by Jupiter, Saturn, Uranus and Neptune.¹ The next phase of space exploration was planetary orbiters that collected data at Venus, Mars, Jupiter, and Saturn. Probably, the most challenging and exciting missions to date have been the Mars landers, and several of these missions are currently ongoing. In the planning stage are sample-return missions. In addition to planetary exploration missions, there have been a number of missions that have explored planet Earth, including synthetic aperture radar (SAR) missions that have mapped the entire planet.

This monograph is organized around the various eras and has contributions from many of the engineers involved in the development of the missions. The contributors are all identified in the title of the section. Chapter 1 gives a brief introduction and presents the methods of analysis, with supporting mathematical details of the various antenna types described throughout the remainder of the monograph. It also describes some design and measurement techniques. John Huang contributed the sections on microstrip antennas, and Mark Gatti provided the section on near-field measurements. Chapter 1, combined with the first chapter of [1], gives a very thorough reference on spacecraft and ground antenna analysis techniques, and it could be used in a graduate course on electromagnetics.

Chapter 2, “The Early Years,” describes some of the antennas used on the very first Earth-orbiting and Moon missions, such as the Explorer, Pioneer, Ranger, and Surveyor spacecraft.

Chapter 3, “The Planetary Flybys,” describes the antennas used on the first missions that flew by the planets. It includes the Mariner series of spacecraft that flew by Mars, Venus, and Mercury, as well as the Grand Tour Voyager Mission.

Chapter 4, “The Mars Missions,” by Joe Vacchoine, is a comprehensive chapter that covers all the Mars missions including the early orbiters and landers, as well as the more recent orbiters, landers, and rovers. It includes a complete description of the antennas on the Mars Exploration Rover (MER) landers.

Chapter 5, “The Orbiters,” with contributions from Roberto Mizzoni and Mark Gatti, describes the antennas on the past and current orbiter missions (not including the Mars Missions) such as the Magellan (Venus Radar Mapper), and the Jupiter and Saturn orbiters. It describes the failed deployable mesh antenna

¹ In 1965 Gary Flandro proposed that, due to a once-per 175-year alignment of planets on one side of the Sun in the 1970s, a multi-planet “Grand Tour” opportunity existed to allow a single spacecraft to explore the four outer planets of the Solar System.

on the Galileo Spacecraft as well as the complicated four-frequency combined radar and communications antenna on the Cassini spacecraft.

Chapter 6, “Spaceborne SAR Antennas for Earth Science,” by Yunjin Kim and Rolando Jordan, describes the Earth science SAR missions.

Chapter 7, “Instrument Packages,” by Richard Cofield, describes antennas used on various instrument packages for science spacecraft. It includes antennas used on scatterometers and radiometers. Richard Hodges contributed the section on the Wide Swath Ocean Altimeter. There is some overlap in subject material with Chapter 6 as a SAR antenna is also a science instrument, but each chapter has a slightly different perspective and describes different instruments.

Chapter 8, “Mechanical Development of Antenna Systems,” by Greg Davis and Rebekah Tanimoto, discusses the various mechanical aspects of spacecraft antenna design. It also discusses the test program necessary to qualify a spacecraft antenna.

Chapter 9, “Miscellaneous Other Antennas,” describes a few unique antennas that did not readily fit into the other chapters. Included is the Solar Probe antenna and the Deep Impact antenna by Dan Hoppe.

Finally in Chapter 10, John Huang discusses future spacecraft antenna research and development.

1.1 Technology Drivers

William A. Imbriale

Antennas on board JPL spacecraft are used for telecommunications, as science instruments, or for both purposes. Technology required for science instruments is dictated by the specific science objectives and tends to be mission specific. Technology drivers for deep-space telecommunications are more universal and apply to all missions. The following discusses the main requirements for deep-space telecommunications antennas.

The communication links to deep space are asymmetric, with considerably more data on the downlink (space to Earth) than on the uplink (Earth to space) because the downlink contains the science, and telemetry data and the uplink is primarily used for commanding the spacecraft. The key element of the telecommunications-link performance is the ground-received power signal-to-noise ratio (SNR), which is given by

$$S/N \approx \frac{P_T G_T G_R}{4\pi R^2 N} = \frac{4\pi P_T A_T A_R}{\lambda^2 R^2 k B T_s} \quad (1.1-1)$$

where

- P_T = spacecraft transmit power
- G_T = transmit gain
- G_R = receive gain

R	=	distance to the spacecraft
N	=	total noise
A_T	=	the effective area of the transmit (spacecraft) antenna
A_R	=	the effective area of the receive ground antenna
T_s	=	receive system-noise temperature
λ	=	wavelength
k	=	Boltzman's constant
B	=	bandwidth

Thus, data rate is proportional to the spacecraft effective isotropic radiated power (EIRP), or the product of antenna gain and radiated power. High-power spacecraft transmitters and large-aperture antennas are a priority for increasing direct-to-Earth telecommunications performance. Hence, a design that makes the maximum use of the transmit antenna area (high efficiency) is desired. However, not only should the antenna have high gain, but it must be pointed in the right direction. In theory, the main beam pointing could be accomplished electronically or mechanically. But to date, JPL has not used electronic beam pointing, but has relied on mechanically pointing the beam either by gimbaling the antenna or, in the case of a fixed body-mounted antenna, by pointing the entire spacecraft. The necessity to point a high-gain antenna in the proper direction gives rise to the need for antennas that will work when it is not possible to accurately point the antenna. Thus, there is also the need for omni type antennas (antennas that have almost complete spatial coverage) for times when pointing may be completely unknown (emergency situations) or for medium gain (broader beamwidth) when precise pointing may not be available.

There are also a number of environmental factors that must be considered in spacecraft antenna design. The antenna must operate in the vacuum of space and over wide temperature ranges. Sometimes, as in the case of the Solar Probe antenna (Chapter 9), the extreme temperatures dictate the materials that can be used in the design. The antenna must also survive the launch without damage. This includes the launch loads, vibration, shock, and acoustic conditions. Weight and power consumption are at a premium; hence the requirement for light-weight materials. Size is also a major consideration, as the antenna must fit inside the launch-vehicle shroud. For antennas that are too large to fit in the shroud, it is necessary to fold and stow the antenna for launch and deploy it for use.

There are many cases where a direct-to-Earth link, as described above, is not feasible. These applications include small in-situ landers, microprobes, and aerobots as currently in use or planned for Mars missions. These surface or atmospheric probe missions are characterized by their small size (<100 kg) and highly constrained energy budgets (<200 W-hr/sol). Typically, they cannot afford the mass and energy required for any meaningful data return directly over a deep-space link. Rather, these missions require, and are enabled by,

energy-efficient relay communications commonly referred to as proximity links [2,3]. Choice of frequency band is largely dictated by whether directional or omni links are envisioned. For omni-to-omni links, lower frequencies perform better, and the 400-MHz UHF links currently being utilized represent a compromise between communications performance and radio frequency (RF) component size.

1.1.1 Frequency Bands Allocated to Deep-Space Communications

The International Telecommunication Union (ITU) has allocated frequency ranges for use in deep-space and near-Earth research. These ranges are listed in Table 1-1.

1.1.2 Frequency Bands Recommended for Proximity Links

In addition to the formally allocated space-to-Earth links, the Consultative Committee for Space Data Systems (CCSDS) provides a recommendation for space data system standards in the area of proximity space links [4]. Proximity space links are defined to be short-range, bi-directional, fixed, or mobile radio links, generally used to communicate among probes, landers, rovers, orbiting constellations, and orbiting relays. These links are characterized by short time delays, moderate (not weak) signals, and short, independent sessions. The ultrahigh frequency (UHF) frequency allocation consists of 60 MHz between 390 to 450 MHz. The forward frequency band (portion where the caller transmits and the responder receives) is defined from 435 to 450 MHz. The return band (portion where the responder transmits and the caller receives) is defined as from 390 to 405 MHz. There is a 30-MHz deadband between them.

Table 1-1. Allocated frequency bands (GHz).

Band	Deep-Space Bands for Spacecraft Farther Than 2 Million km from Earth		Near-Earth Bands for Spacecraft Closer Than 2 Million km from Earth	
	Uplink ^a	Downlink ^b	Uplink ^a	Downlink ^b
S	2.110–2.120	2.290–2.300	2.025–2.110	2.200–2.290
X	7.145–7.190	8.400–8.450	7.190–7.235	8.450–8.500
Ka	34.200–34.700	31.800–32.300	Not applicable	Not applicable

^a Earth to space.

^b Space to Earth.

1.2 Analysis Techniques for Designing Reflector Antennas

William A. Imbriale

Reflector antennas have existed since the days of Hertz. They represent one of the best solutions for high gain and lightweight, easily stowable antenna systems. The use of physical optics (PO) analysis provides the required performance estimate accuracy. Almost all of the spacecraft reflector antennas were either designed or analyzed using PO, and the measured performance is within a few percent of the calculated values.

In addition to PO, there are many other techniques required to completely design and characterize the antenna system. Accurate programs to design and analyze the feed horn, and transform far-field patterns to near field for use in the PO analysis are required. Synthesis programs are used to determine the reflector shape for maximum gain. The sections on PO analysis, Feed Horn analysis, Spherical-Wave Analysis and Dual-Reflector Shaping are covered in [1], but these concepts are so fundamental they are also included in this reference for completeness. Tools to design and analyze frequency-selective surfaces are also needed for use in multi-frequency systems. And, programs to characterize the effect of a mesh surface for a lightweight deployable antenna are also required. The basic mathematical details of each of these techniques are given in this section with examples of their use sprinkled throughout the book.

1.2.1 Radiation-Pattern Analysis

Physical optics (PO) is by far the most important analytical tool, and it is used to calculate the scattered field from a metallic reflecting surface—in this case, a reflector antenna. Electrical currents, which excite the scattered field, are induced on the conducting surface by an incident wave assumed to be of a known amplitude, phase, and polarization everywhere in space (from a feed or other reflecting surface, for example). The PO approximations to the induced surface currents are valid when the reflector is smooth and the transverse dimensions are large in terms of wavelengths. The closed reflecting surface is divided into a region S_1 , which is illuminated by direct rays from the source (“illuminated region”) and a region S_2 , which is geometrically shadowed (“shadowed region”) from direct rays from the source (Fig. 1-1). The PO approximations for the induced surface current distribution are

$$\begin{aligned} J_s &= 2(\hat{n} \times H_{inc}) & \text{on } S_1 \\ J_s &= 0 & \text{on } S_2 \end{aligned} \quad (1.2-1)$$

where \hat{n} is the surface normal and H_{inc} the incident field. The expressions are then inserted into the radiation integral [5] to compute the scattered field.

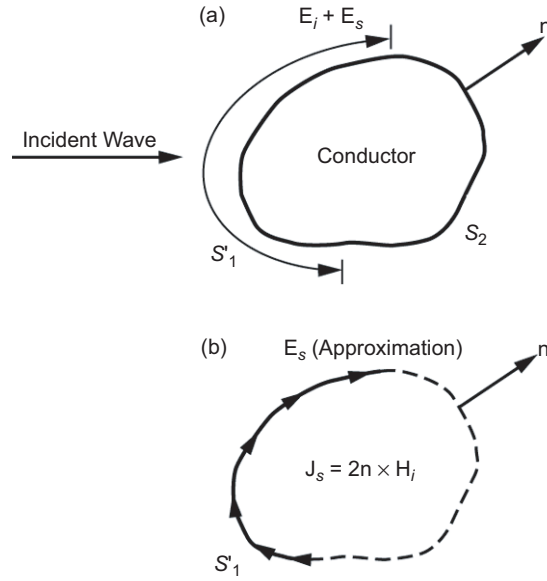


**Fig. 1-1. The physical optics approximation:
(a) original problem and (b) approximation.**

Rusch and Potter [6] provide a good introduction to the early techniques used for analyzing the reflector antennas of the Deep Space Network (DSN). More recently, due primarily to the orders-of-magnitude improvements in computer speed and memory, a very simple but extremely robust algorithm has emerged as the computer program of choice for computing the PO radiation integral. The algorithm is documented in [7 and 8], but because of its extreme importance and to provide a fairly complete reference, it is repeated here.

One of the simplest possible reflector-antenna computer programs is based on a discrete approximation of the radiation integral. This calculation replaces the actual reflector surface with a triangular facet representation so that the reflector resembles a geodesic dome. The PO current is assumed to be constant in magnitude and phase over each facet, so the radiation integral is reduced to a simple summation. This program was originally developed in 1970 and has proven to be surprisingly robust and useful for the analysis of reflectors, particularly when the near field is desired and the surface derivatives are not known. The initial limitation to small reflectors was primarily due to the speed and memory limitations of the then-existing computers.

Two improvements significantly enhanced the usefulness of the computer program: The first was the orders-of-magnitude increase, over time, in computer speed and memory, and the second was the development of a more sophisticated approximation of the PO surface current, which permitted the use of larger facets. The latter improvement is due to the use of a linear-phase

approximation of the surface current. Within each triangular region, the resulting integral is the two-dimensional Fourier transform of the projected triangle. This triangular-shape function integral can be computed in closed form. The complete PO integral is then a summation of these transforms.

1.2.1.1 Mathematical Details. The PO radiation integral over the reflector surface, Σ , can be expressed as [8]

$$\mathbf{H}(\mathbf{r}) = -\frac{1}{4\pi} \int_{\Sigma} \left(jk + \frac{1}{R} \right) \hat{\mathbf{R}} \times \mathbf{J}_s(\mathbf{r}') \frac{e^{-jkR}}{R} ds' \quad (1.2-2)$$

in which \mathbf{r} designates the field point, \mathbf{r}' the source point, $R = |\mathbf{r} - \mathbf{r}'|$ is the distance between them, and $\hat{\mathbf{R}} = (\mathbf{r} - \mathbf{r}')/R$ is a unit vector.

For the purpose of analysis, the true surface, Σ , is replaced by a contiguous set of triangular facets. These facets, denoted Δ_i , are chosen to be roughly equal in size with their vertices on the surface, Σ . Figure 1-2 shows a typical facet and its projection onto the x - y plane. Let (x_i, y_i, z_i) represent the *centroid* of each triangle where the subscript $i = 1, \dots, N$ is associated with a triangle. Then, the field obtained by replacing the true surface, Σ , by the triangular facet approximation is

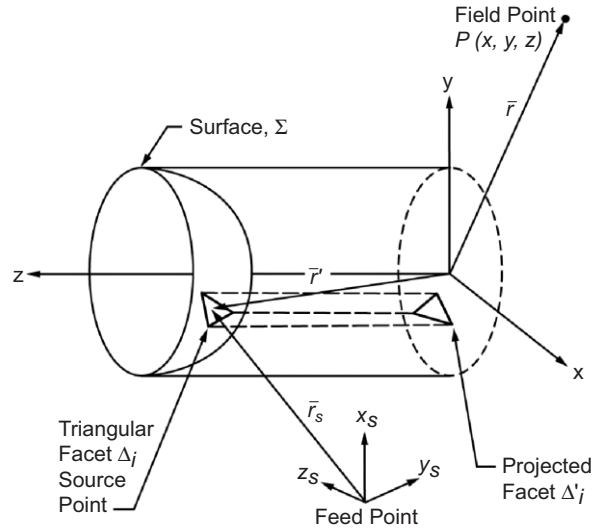


Fig. 1-2. Reflector-analysis coordinate systems and a typical triangular facet.

$$\mathbf{H}(\mathbf{r}) = -\frac{1}{4\partial} \sum_{i=1}^N \int_{\Delta_i} \left(jk + \frac{1}{R} \right) \hat{\mathbf{R}} \times \mathbf{J}(\mathbf{r}') \frac{e^{-jkR}}{R} ds' \quad (1.2-3)$$

In Eq. (1.2-3), \mathbf{J} is now the equivalent surface current evaluated on the triangular facets. Since the triangles are small, it is expected that $\hat{\mathbf{R}}$ and R do not vary appreciably over the area of a given facet. Thus, let $\hat{\mathbf{R}}_i$ and R_i be the value obtained at the centroid (x_i, y_i, z_i) of each facet and approximate Eq. (1.2-3) by

$$\mathbf{H}(\mathbf{r}) = \frac{1}{4\pi} \sum_{i=1}^N \left[jk + \frac{1}{R_i} \right] \hat{\mathbf{R}}_i \times \mathbf{T}_i(\mathbf{r}) \quad (1.2-4)$$

$$\mathbf{T}_i(\mathbf{r}) = \int_{\Delta_i} \mathbf{J}_i(\mathbf{r}') \frac{e^{-jkR}}{R_i} ds' \quad (1.2-5)$$

Assume that the necessary transformations have been performed so that the incident field, \mathbf{H}_s , is given in terms of the reflector coordinate system. Then

$$\mathbf{J}_i(\mathbf{r}') = 2\hat{\mathbf{n}}_i \times \mathbf{H}_s(\mathbf{r}') \quad (1.2-6)$$

Next, assume that the incident field can be represented by a function of the form

$$\mathbf{H}_s = \mathbf{h}_s(\mathbf{r}_i) \frac{e^{-jkr_s}}{4\pi r_{si}} \quad (1.2-7)$$

where r_s is the distance to the source point and r_{si} is the distance from the triangle centroid to the source point. Then, Eq. (1.2-5) can be written

$$\mathbf{T}_i(\mathbf{r}) = \frac{\hat{\mathbf{n}}_i \times \mathbf{h}_s(\mathbf{r}_i)}{2\pi R_i r_{si}} \int_{\Delta_i} e^{-jk(R+r_s)} ds' \quad (1.2-8)$$

Making use of the Jacobian and approximating

$$R(x, y) + r_s(x, y) = \frac{1}{k} (a_i - u_i x - v_i y) \quad (1.2-9)$$

in which a_i , u_i , and v_i are constants, the expression can be rewritten as

$$\mathbf{T}_i(\mathbf{r}) = \frac{\hat{\mathbf{n}}_i \times \mathbf{h}_s(\mathbf{r}_i)}{2\pi R_i r_{si}} J_{\Delta_i} e^{-ja_i} \int_{\Delta_i'} e^{j(u_i x' + v_i y')} dx' dy' \quad (1.2-10)$$

where the surface normal is

$$\mathbf{N}_i = -\hat{\mathbf{x}} f_{xi} - \hat{\mathbf{y}} f_{yi} + \hat{\mathbf{z}} \quad (1.2-11)$$

and the Jacobian is

$$J_{\Delta_i} = |\mathbf{N}_i| = \left[f_{xi}^2 + f_{yi}^2 + 1 \right]^{1/2} \quad (1.2-12)$$

It may now be observed that this integral is the two-dimensional (2-D) Fourier transform of the i^{th} projected triangle Δ_i' , expressed as

$$S(u, v) = \int_{\Delta_i'} e^{j(ux' + vy')} dx' dy' \quad (1.2-13)$$

and can be computed in closed form as described in [9]. The full radiation integral is the sum of all the transforms of the individual triangles.

1.2.1.2 Application to Dual-Reflector Antennas. The PO integration methodology is incorporated in a sequential fashion for the analysis of a dual-reflector antenna system. Initially, the feed illuminates the subreflector, and the currents on the subreflector surface are determined. Subsequently, the near fields scattered from the subreflector are used to illuminate the main reflector, and its induced currents are determined. The main reflector scattered fields are then determined by integrating these currents.

Many coordinate systems are required to allow flexibility in locating and orienting the feed, subreflector, main reflector, and output-pattern generation. The relation among the various coordinate systems is depicted in Fig. 1-3 where (x_F, y_F, z_F) is the feed coordinate system, (x_S, y_S, z_S) is the subreflector coordinate system, and (x_M, y_M, z_M) is the main reflector coordinate system.

1.2.1.3 Useful Coordinate Transformations. In the discussion of the preceding sections (1.2.1.1 and 1.2.1.2), the analysis is performed using two distinct coordinate systems: reflector and feed coordinates. In addition, it is sometimes convenient to display the computed patterns in yet another coordinate system. Consequently, one must know the transformation equations that permit coordinates and vectors described in one coordinate system to be expressed in terms of some other coordinate system. The transformation may require both translation and rotation. The required transformations are described below. They are the Cartesian-to-spherical transformation and coordinate rotations using Eulerian angles.

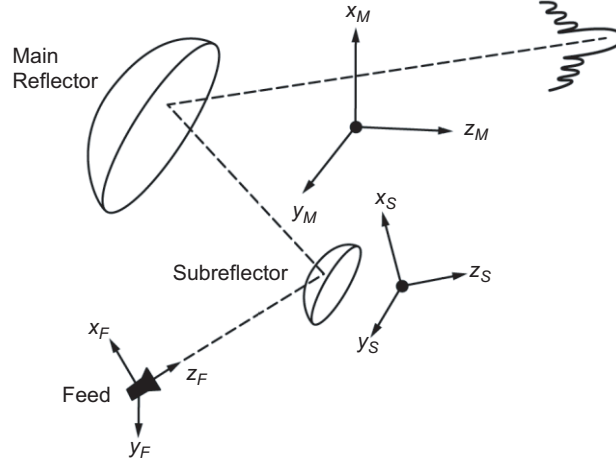


Fig. 1-3. Dual-reflector coordinate systems.

The Cartesian-to-spherical transformation is conveniently summarized in matrix form. With the Cartesian components of a vector, \mathbf{H} , denoted (H_x, H_y, H_z) and the spherical components (H_r, H_θ, H_ϕ) , one finds that the transformation is

$$\begin{bmatrix} H_r \\ H_\theta \\ H_\phi \end{bmatrix} = \begin{bmatrix} \sin \theta \cos \phi & \sin \theta \sin \phi & \cos \theta \\ \cos \theta \cos \phi & \cos \theta \sin \phi & -\sin \theta \\ -\sin \phi & \cos \phi & 0 \end{bmatrix} \begin{bmatrix} H_x \\ H_y \\ H_z \end{bmatrix} \quad (1.2-14)$$

The inverse transformation is just the transpose of the above matrix.

Rotations are handled by the use of the Eulerian angles (α, β, γ) . These angles describe three successive rotations that bring one Cartesian system into alignment with another. Let the two systems be denoted (x_1, y_1, z_1) and (x_2, y_2, z_2) . As illustrated in Fig. 1-4, the angles are defined as follows:

- α describes a positive rotation about the z_1 axis, which brings the x_1 axis into the x' axis aligned with the *line of nodes* (the line of intersection between the (x_1, y_1) and (x_2, y_2) planes)
- β describes a positive rotation about the line of nodes (the x' axis) that brings the z_1 axis to z_2
- γ describes a positive rotation about the z_2 axis, which brings the x' axis to the x_2 axis.

The phrase “positive rotation” means the direction of increasing angular measure as defined by the right-hand rule with respect to the axis about which

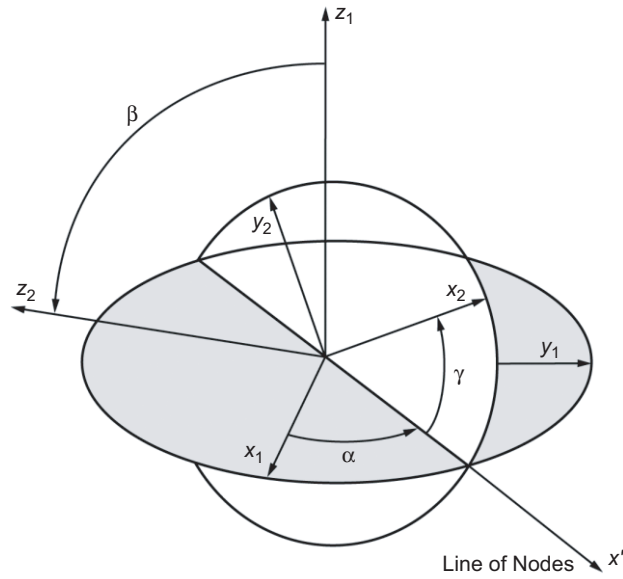


Fig. 1-4. Euler-angle definitions.

the rotation occurs. Each of the rotations just described is performed using the standard rotation of coordinate formulas of plane analytic geometry.

When these expressions are written in matrix form and applied successively as described above, one obtains the following matrix equation that represents a general three-dimensional (3-D) rotation of coordinates.

$$\begin{bmatrix} x_2 \\ y_2 \\ z_2 \end{bmatrix} = \begin{bmatrix} A_{11} & A_{12} & A_{13} \\ A_{21} & A_{22} & A_{23} \\ A_{31} & A_{32} & A_{33} \end{bmatrix} \begin{bmatrix} x_1 \\ y_1 \\ z_1 \end{bmatrix} \quad (1.2-15)$$

where the individual matrix elements are

$$\begin{aligned} A_{11} &= \cos \gamma \cos \alpha - \sin \gamma \cos \beta \sin \alpha \\ A_{12} &= \cos \gamma \sin \alpha + \sin \gamma \cos \beta \cos \alpha \\ A_{13} &= \sin \gamma \sin \beta \\ A_{21} &= -\sin \gamma \cos \alpha - \cos \gamma \cos \beta \sin \alpha \\ A_{22} &= -\sin \gamma \cos \alpha + \cos \gamma \cos \beta \cos \alpha \\ A_{23} &= \cos \gamma \sin \beta \\ A_{31} &= \sin \beta \cos \gamma \\ A_{32} &= -\sin \beta \cos \alpha \\ A_{33} &= \cos \beta \end{aligned}$$

The inverse transformation is just the transpose of the matrix given above.

Although the formulas are presented in terms of coordinate transformations, the transformation matrix is equally valid for the Cartesian components of a vector. Thus, the components of a vector, \mathbf{H} , transform as

$$\begin{bmatrix} H_{x,2} \\ H_{y,2} \\ H_{z,2} \end{bmatrix} = \begin{bmatrix} A_{11} & A_{12} & A_{13} \\ A_{21} & A_{22} & A_{23} \\ A_{31} & A_{32} & A_{33} \end{bmatrix} \begin{bmatrix} H_{x,1} \\ H_{y,1} \\ H_{z,1} \end{bmatrix} \quad (1.2-16)$$

Further information can be found in [10].

1.2.1.4 A Numerical Example of Radiation-Pattern Analysis. In the 1980s, a FORTRAN program was written to perform the linear phase calculations indicated above. The program was extensively verified by comparing the measured data, for example, [11], and many other computer codes.

A simple but interesting example is that of an ellipse, shown in Fig. 1-5. The projected aperture of the ellipse is about 3 m. In the x_p axis, the illuminated function is a $\cos^4 \theta$ pattern function (22.3-dB gain), and the frequency is 31.4 GHz. The ellipse is about 350λ along the major axis. Figure 1-6 compares the constant-phase approximation for three different grid densities: approximately 4000, 10,000, and 23,000 triangles. This illustrates a general trend of the method; that is, depending on the size of the triangles, there is an angular limit over which the solution is valid. Figure 1-7 compares the linear-phase approximation with the constant-phase approximation for the 4000-triangle case and demonstrates that the angular range is larger with the linear-phase approximation.

1.2.2 Feed-Horn Analysis

An equally critical aspect of the analysis of reflector systems is the ability to accurately compute the radiation pattern of the feed. More details on the design of the feeds will be given later, but the analysis technique for computing the radiation patterns of the feed is summarized below.

Two types of feed horns possessing equal E- and H-plane patterns are commonly used. The first is the dual-mode feed horn [12], and the second is the corrugated feed horn [13]. In the dual-mode horn, a dominant mode circular waveguide is connected to another guide of slightly larger diameter, where modes up to transverse magnetic (TM_{11}) may propagate; the higher order modes being generated by the step transition. The step size is chosen to generate the precise amount of TM_{11} mode from the transverse electric (TE_{11}) mode so that when the two modes travel through the flared horn section that follows, the E- and H-plane patterns are equalized. The bandwidth of this feed

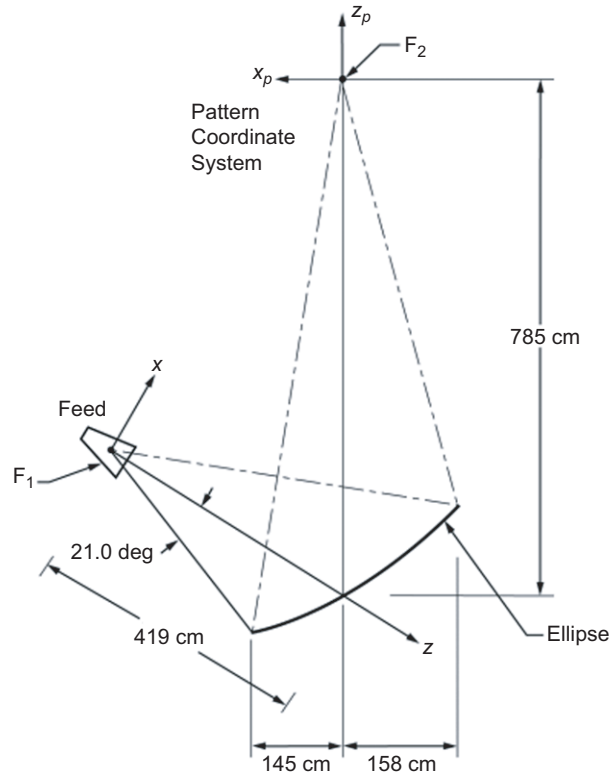


Fig. 1-5. Ellipse geometry.

horn is limited since the two modes must arrive at the horn aperture in phase, and the two modes have phase velocities that vary differently with frequency.

In the corrugated feed horn, the single-mode smooth-wall waveguide is connected to a corrugated waveguide that supports only the hybrid (HE_{11}) mode. Some matching between the waveguides is provided by gradually changing from $\lambda/2$ slot depth to $\lambda/4$ slot depth in a short transition region. Throughout the transition region, only the HE_{11} corrugated waveguide mode may propagate, and the E- and H-plane radiation patterns of this mode become nearly equal when the balanced condition is reached (slot depth = $\sim\lambda/4$). The bandwidth of this horn is larger than that of the dual-mode horn because the transverse electric field patterns and, hence, the radiation pattern of the HE_{11} mode are relatively insensitive to small changes in slot depth around the balanced condition (slot depth = $\sim\lambda/4$). After the HE_{11} mode is established in the single-mode corrugated waveguide, the guide is gradually flared, without changing the slot depth, to the required aperture size.

The corrugated section is analyzed using a computer code developed by Hoppe [14–16]. The analysis follows the method of James [17], expanding the

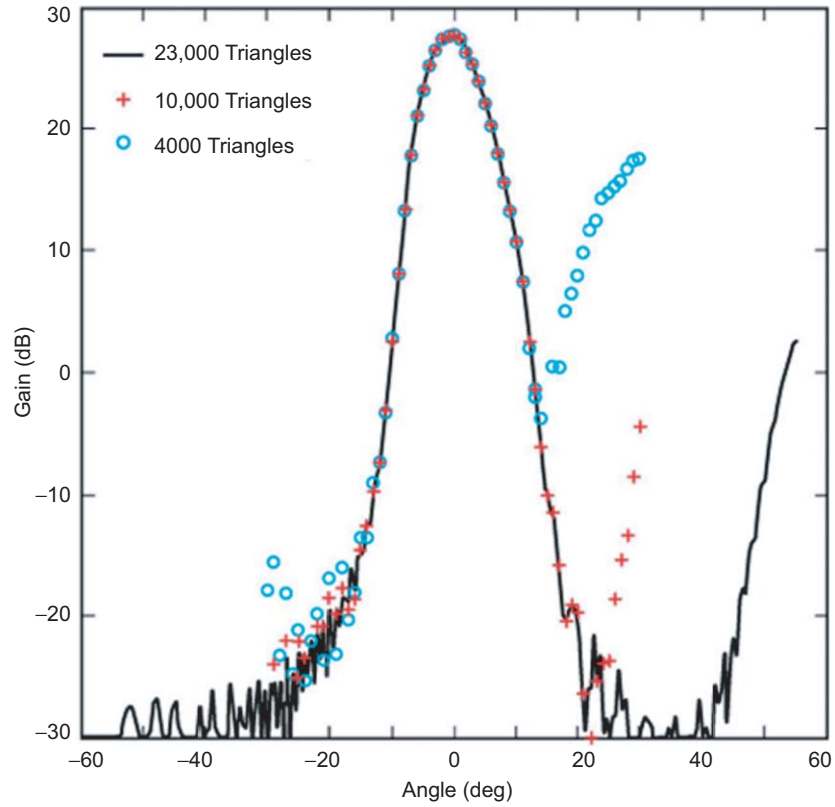


Fig. 1-6. Ellipse example: constant-phase approximation for offset plane.

fields inside each fin and slot in terms of circular waveguide modes, and matching the fields at each slot–fin boundary. All of the possible propagating modes (as well as a sufficient number of evanescent modes) are matched at each boundary, with results for successive edges and waveguide lengths cascading as the analysis moves through the device. In this way, the interactions between the fields of nonadjacent as well as adjacent slots are taken into account. The result of the calculation is a matrix equation relating the reflected and aperture modes to the input modes.

If \mathbf{a}_1 is a vector containing the power-normalized amplitudes of the input modes, then we may calculate the reflected modes, \mathbf{b}_1 , and the aperture modes, \mathbf{b}_2 , using

$$\mathbf{b}_2 = [S_{21}] \mathbf{a}_1 \quad (1.2-17)$$

$$\mathbf{b}_1 = [S_{11}] \mathbf{a}_1 \quad (1.2-18)$$

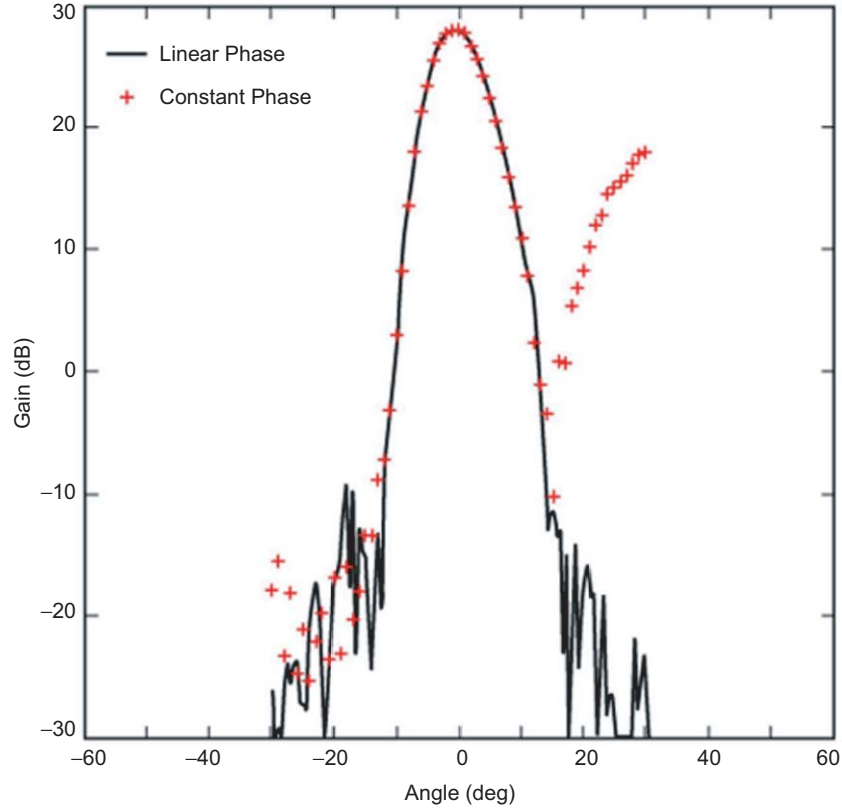


Fig. 1-7. Ellipse example: constant versus linear phase for offset plane.

Here, $[S_{21}]$ and $[S_{22}]$ are the scattering matrices resulting from the computer run. See the appendix of [17]. They depend only on frequency and device dimensions, not input modes. We may therefore specify any input vector \mathbf{a}_1 and calculate the reflected and aperture fields. Using the normalized amplitudes calculated above, and the normalized vector functions giving the field distributions for each mode, we find the aperture field \mathbf{E}_B . The far field is then calculated by the method described by Silver and Ludwig [18,19].

$$\mathbf{E}_c = \frac{-1}{4\pi} \iint_S \left(-j\mu\omega (\hat{n} \times \mathbf{H}_B) \phi + (\hat{n} \times \mathbf{E}_B) \times \nabla \phi \right) ds \quad (1.2-19)$$

where

- \mathbf{E}_B = aperture electric field
- \mathbf{H}_B = aperture magnetic field
- \hat{n} = unit vector normal to aperture surface
- ds = incremented area on aperture surface

ω	=	$2\pi f$ angular frequency
f	=	frequency
μ	=	free-space permeability
∇	=	gradient operator
ϕ	=	e^{-jkr}/r
k	=	$2\pi/\lambda_0$ wave number
r	=	far-field point distance from origin (spherical radius)

When \mathbf{E}_B and \mathbf{H}_B are represented in terms of circular waveguide modes, the resulting integrals have already been evaluated by Silver [18]. Therefore, given an input vector and the scattering matrix, we determine the aperture modes and composite far-field patterns. A spherical-wave analysis is then used to compute the feed-horn near-fields pattern for use in the PO software. Throughout the analysis, care must be taken to ensure proper normalization of the field amplitudes in terms of power. The smooth wall conical feed horn is modeled with the same software by approximating the horn taper with small steps and zero-depth corrugated slots.

The mode-matching technique for analyzing corrugated horns yields excellent agreement with the measured patterns—so much so, in fact, that if the computed and measured patterns do not match, it is most likely due to measurement and/or manufacturing errors. There is a recent example of a fairly complicated X-/X-/Ka-band horn described in [1] and [20] that shows excellent agreement between measured and calculated feed patterns. There are also several very good examples given in later chapters with probably the most complicated horn being the Cassini antenna three-frequency horn described in Chapter 5.

1.2.3 Spherical-Wave Analysis

Spherical-wave-expansion coefficients are frequently used in the analysis of reflector systems. Their basic purpose is to transform far-field patterns to the near-field so that PO may be used for reflectors in the near field of their illumination source.

The theory of spherical waves is described in [21] and will only be briefly outlined here. Any electromagnetic field in a source-free region may be represented by a spherical-wave expansion. In general, the expansion must include both incoming and outgoing waves. If the field satisfies the radiation condition, only outgoing waves will be present, and the expansion will be valid outside the smallest sphere enclosing all sources (the sphere center must be at the coordinate origin used for the expansion). The radial dependence of the spherical waves is then given by the spherical Hankel function $h_n^2(kR)$. Another common case is an expansion valid inside the largest sphere enclosing no sources. In this case, the incoming and outgoing waves are present in equal

amounts, producing a radial dependence given by the spherical Bessel function $j_n(kR)$.

Although the spherical-wave expansion can be applied to either of these two most common cases, the version used most typically for antenna analysis assumes outgoing waves.

In either case, the input data that are used to specify the field is the tangential E-field on the surface of a sphere. For the first case, the data-sphere radius must be greater than or equal to the radius of the sphere enclosing the sources. For far-field data, the data-sphere radius is considered to be infinite. For the second case, the data-sphere radius must be less than or equal to the largest sphere enclosing no sources, and must be greater than zero.

The maximum value of the Hankel function index that is needed to closely approximate the field is roughly equal to ka ($ka + 10$ is typical, but in some cases a lower limit will work), where a is the radius of the sphere enclosing all (or no) sources for the first (and second) case, respectively.

Input data is specified on a grid of points defined by the intersection of constant contours of θ and ϕ . The amplitude and phase of E_θ and E_ϕ are given at each point. The minimum number of θ values is roughly 1.2 times the maximum value of n .

The azimuthal dependence of spherical waves is given by $\sin(m\phi)$ and $\cos(m\phi)$. In general, m runs from 0 to the maximum value of n . As is often the case, symmetry can be used to reduce the number of azimuthal terms. A conical feed radiates only $m = 1$ modes, and reflection from a body of revolution will maintain this behavior. There can be even and odd ϕ dependence, but quite often only one will be present. For the even ϕ dependence, E_θ can be expanded in only $\sin(m\phi)$ terms and E_ϕ in only $\cos(m\phi)$ terms. For the odd case, this is reversed. The minimum number of ϕ values for the data sphere is, in general, $2M + 1$, where M is the maximum value of m .

The output of the computer program is the set of spherical-wave-expansion coefficients. These coefficients may then be used to compute the field anywhere within the region of validity. Therefore, the essential utility the program is to take data consisting of the tangential E-field on a sphere (whose radius may be infinite), and provide the means of computing the field—all three components of E and H—at any other point in the region of validity.

The computer program used is patterned after that in [22].

1.2.4 Dual-Reflector Shaping

The simplest form of a dual reflector system, the Cassegrain, has a parabolic main reflector and a hyperbolic subreflector. The efficiency of these reflectors is primarily determined by (a) the ability of the feed system to illuminate only the reflectors while minimizing the energy that radiates

elsewhere and (b) the ability of the feed plus the subreflector to uniformly illuminate the parabola. Item (a), above, is termed “spillover efficiency” and (b) “illumination efficiency.” The illumination efficiency is 100 percent when the energy density on the entire main reflector aperture is a constant.

Feed-horn patterns always taper gradually from their central maxima to nulls. If all this energy is intercepted by the reflector (for maximum spillover efficiency), the illumination is far from uniform, and the illumination efficiency is very poor. Consequently, any attempt to obtain nearly uniform illumination will result in a great loss of energy in spillover. Therefore, a compromise must be made. A common choice for both a prime focus system and the Cassegrain system is a 10-dB taper of the illumination pattern at the parabolic edge. This selection results in a combination of spillover and illumination efficiency of from about 75 to 80 percent.

It is possible, however, to change the shape of the two reflectors to alter the illumination function and improve efficiency. This methodology is termed dual-reflector shaping and was first introduced by Galindo [23], who demonstrated that one could design a dual-reflector antenna system to provide an arbitrary phase and amplitude distribution in the aperture of the main reflector. Thus, if one chose a uniform amplitude and constant phase, 100 percent illumination efficiency could be achieved. With the feed pattern given, the subreflector size would be chosen to give minimal spillover.

1.2.4.1 Theoretical Solution for the Symmetric Case. The complete solution can be found in [23 and 24], and only the uniform aperture case is summarized below.

The geometry of the symmetric dual-reflector system is shown in Fig. 1-8. Due to circular symmetry, the synthesis reduces to the determination of the intersection curve (of the surface) with the plane through the axis of symmetry, that is, the x,y plane.

The synthesis method uses the analytical expressions of geometrical optics (GO) principles together with the reflector geometry to develop a pair of first-order, nonlinear ordinary differential equations of the form

$$\frac{dy}{dx} = f(x,y) \quad (1.2-20)$$

which leads to cross sections of each reflector when subject to boundary conditions such as

$$y(x = x_{\max}) = 0 \quad (1.2-21)$$

which are then solved by a high-speed digital computer.

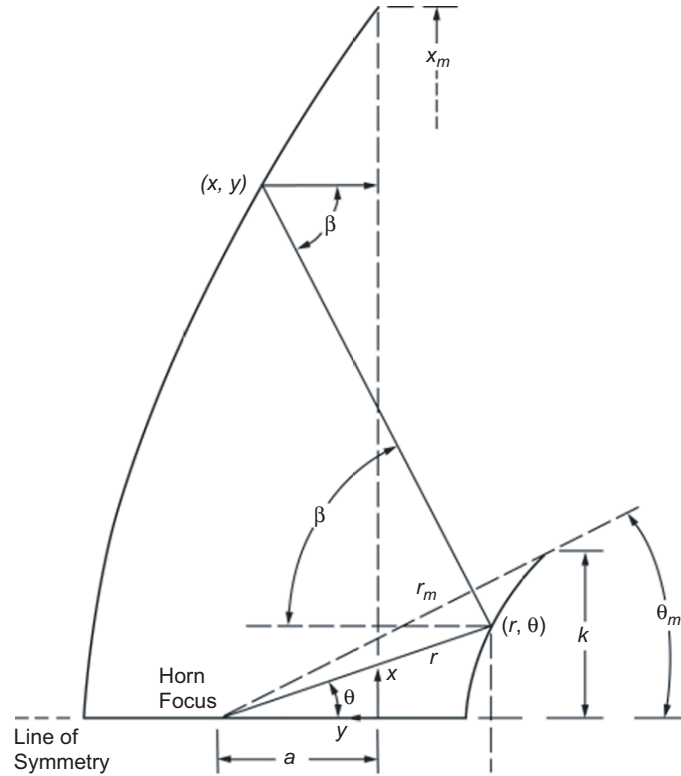


Fig. 1-8. Coordinate system for shaping.

The optical principles that are used to develop the required equations are that (a) the angle of incidence is equal to the angle of reflection (Snell's Law), (b) energy flow is conserved along the ray trajectories, and (c) surfaces of constant phase form normal surfaces to ray trajectories.

The incident field is assumed to have a spherical-phase function, that is, a phase center, and a power-radiation pattern $F(\theta)$. For uniform phase in the aperture, the path length, $r + r' + r''$, must remain constant for all θ . Also, the amplitude function in the aperture $I(x)$ must also be equal to a prescribed distribution (constant for maximum peak gain).

The equation for equal path lengths resulting in the phase front is obtained from trigonometry:

$$r + y + \frac{x - r \sin \theta}{\sin \beta} = C \text{ (constant)} \quad (1.2-22)$$

where (x, y) and (r, θ) are the coordinates of points on the main reflector and subreflector, respectively.

The application of Snell's law to the two surfaces defines a relationship between the angles shown and the first derivatives (slopes) of the surfaces. These are

$$\frac{1}{r} \frac{dr}{d\theta} = \tan \frac{\theta + \beta}{2} \quad (1.2-23)$$

$$\frac{-dy}{dx} = \tan \frac{\beta}{2} \quad (1.2-24)$$

Since the dual-reflector system is symmetrical about the y -axis, the total power within the increment $d\theta$ of the pattern $F(\theta)$ will be $F(\theta)2\pi \sin\theta d\theta$. Similarly, the total power within the increment dx of the main antenna aperture is $I(x)2\pi dx$, where $I(x)$ is the illumination function of the antenna aperture. Making $I(x)$ constant and equating the total power from $\theta=0$ to angle θ to that within x , and normalizing by the total power, one obtains

$$x^2 = x_{\max}^2 \frac{\int_0^\theta F(\theta) \sin \theta d\theta}{\int_0^{\theta_{\max}} F(\theta) \sin \theta d\theta} \quad (1.2-25)$$

These four equations now have five dependent variables (x , y , r , θ , and β) and can be solved to provide equations for the surfaces. This procedure yields an optimum-gain antenna. The antennas used on the Voyager, Galileo, and Cassini spacecraft described in Chapter 5 were all dual-shaped systems.

1.2.4.2 Offset-Shaped Reflector Antennas. The formulation shown in Section 1.2.4.1 (above) is for circularly symmetric reflector geometries. The exact solution has also been developed for offset geometries [25,26]. The offset geometry will have higher efficiency than the symmetric geometry because the central blockage due to the subreflector can be eliminated. In the early 1980s, an antenna with an offset geometry was designed and built that had an efficiency of 84.5 percent—the highest ever recorded [27].

1.2.5 Dichroic Reflector Analysis

The ability to transmit and receive simultaneously at multiple frequency bands is an important requirement for deep-space communications. It is usually accomplished by using either a dual-band feed horn or separate feed horns and a frequency selective surface (FSS), typically referred to as a dichroic reflector. Dichroic reflectors are important components for both ground and spacecraft antennas. The most frequently used type of surface for ground antennas is a flat metal plate that passes the higher frequency and reflects the lower frequency.

The analysis for those types of surfaces is given in reference [1]. However, for spacecraft antennas, the typical use is for a dichroic subreflector that reflects the higher frequencies and passes the lower frequencies. Examples are the Voyager, Galileo, and Cassini (Chapter 5) high-gain antennas. As these dichroic surfaces play an important role in the telecommunications antennas, this section presents a typical technique for analyzing them.

1.2.5.1 Theoretical Formulation. Dichroic surfaces are analyzed using a combination of Floquet modes and the method of moments. The theory is well documented in references [28–30] and will only be summarized here. In particular, the following is derived from reference [28]. Consider the printed dipole array shown in Fig. 1-9. The surface is assumed infinite in the xy plane. Expanding the fields in the three regions in Floquet modes and applying the appropriate boundary conditions allows the development of an integral equation for the unknown current distribution $J(x,y)$ on the dipoles. If $J(x,y)$ is approximated as follows:

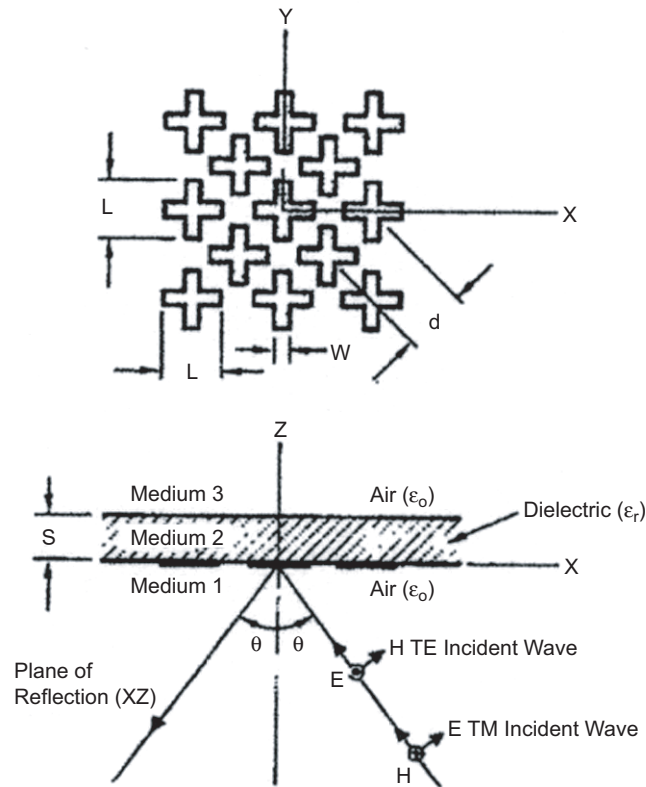


Fig. 1-9. Geometry of the dichroic surface.

$$J(x, y) = \sum_{n=1}^N c_n h_n(x, y), \quad (1.2-26)$$

where the functions $h_n(x, y)$ are complete and orthonormal over a crossed dipole and N is finite for computability, then the integral equation is easily solved using the method of moments. The resulting system of equations is:

$$\begin{aligned} & \sum_{m=1}^2 \left(1 + R_{m00}^{slab} \right) b_m \hat{\mathbf{k}}_{m00} \cdot \mathbf{g}_i^*(\mathbf{k}_{00}) \\ &= \sum_{n=1}^N c_n \frac{1}{d^2} \sum_{m=1}^2 \sum_p \sum_q \\ & \quad \cdot \frac{\hat{\mathbf{k}}_{mpq} \cdot \mathbf{g}_i^*(\mathbf{k}_{pq}) \hat{\mathbf{k}}_{mpq} \cdot \mathbf{g}_n(\mathbf{k}_{pq})}{\eta_{mpq}^{eq}}, \\ & \quad i = 1, 2, \dots, N \end{aligned} \quad (1.2-27)$$

where a time-dependence $\exp(j\omega t)$ is assumed, $m=1$ corresponds to the TM mode, $m=2$ corresponds to the TE mode, and

$$g_l(\mathbf{k}_{pq}) = \int_{\text{dipole}} h_l(x, y) \exp(j\mathbf{k}_{pq} \cdot \boldsymbol{\rho}) dx dy, \quad (1.2-28)$$

d = array spacing,

$\boldsymbol{\rho}$ = $x\hat{x} + y\hat{y}$,

\mathbf{k}_{pq} = $\left(k_0 \sin \theta \cos \phi + \sqrt{2}\pi p / d \right) \hat{x} + \left(k_0 \sin \theta \sin \phi + \frac{\sqrt{2}\pi}{d} + \frac{2\sqrt{2}\pi q}{d} \right) \hat{y}$,

k_0 = $2\pi / \lambda_0$,

λ_0 = free-space wavelength,

(θ, ϕ) = direction of incidence,

b_m = incident field magnitude of m th mode,

$\hat{\mathbf{k}}_{1pq}$ = $\mathbf{k}_{pq} / |\mathbf{k}_{pq}|$,

$\hat{\mathbf{k}}_{2pq}$ = $\hat{z} \times \hat{\mathbf{k}}_{1pq}$,

η_{mpq}^{eq} = $\eta_{mpq}^{\text{air}} + \eta_{mpq}^{\text{diel}} \left(\frac{1 - R_{mpq}}{1 + R_{mpq}} \right)$,

η_{1pq} = $\frac{k\eta}{\gamma_{pq}}$,

$$\begin{aligned}
\eta_{2pq} &= \frac{\gamma_{pq}\eta}{k}, \\
\eta &= \sqrt{\varepsilon/\mu}, \varepsilon, \mu \text{ are the permittivity and permeability of medium,} \\
k &= \text{propagation constant of the medium,} \\
\gamma_{pq} &= \left(k^2 - |\mathbf{k}_{pq}|^2\right)^{1/2}, \quad k^2 > |\mathbf{k}_{pq}|^2, \\
&= -j\left(|\mathbf{k}_{pq}|^2 - k^2\right)^{1/2}, \quad k^2 < |\mathbf{k}_{pq}|^2, \\
R_{mpq} &= \frac{\eta_{mpq}^{\text{diel}} - \eta_{mpq}^{\text{air}}}{\eta_{mpq}^{\text{diel}} + \eta_{mpq}^{\text{air}}} \exp(-j2\gamma_{pq}s), \\
R_{mpq}^{\text{slab}} &= \frac{2\eta_{mpq}^{\text{air}} - \eta_{mpq}^{\text{eq}}}{\eta_{mpq}^{\text{eq}}}.
\end{aligned}$$

Once we select a suitable set of functions \mathbf{h}_n , the unknown coefficients c_n can be easily obtained by solving Eq. (1.2-27). The reflected and transmitted far fields contain only the propagating Floquet modes for which γ_{pq} is real. In a suitable design, by using a small array spacing, the higher order Floquet modes ($|p| > 0, |q| > 0$), which correspond to the grating lobes, are made evanescent. Thus the reflection and transmission coefficients are computed from the following expressions:

$$\mathbf{R}(\theta) = \sum_{m=1}^2 \left\{ R_{m00}^{\text{slab}} b_m - \frac{1}{d^2 \eta_{m00}^{\text{eq}}} \sum_{n=1}^N c_n g_n(\mathbf{k}_{00}) \cdot \hat{\mathbf{k}}_{m00} \right\} \hat{\mathbf{k}}_{m00} \quad (1.2-29)$$

$$\mathbf{T}(\theta) = \sum_{m=1}^2 \left\{ t_{m00} (1 + R_{m00}^{\text{slab}}) b_m - \frac{t_{m00}}{d^2 \eta_{m00}^{\text{eq}}} \sum_{n=1}^N c_n g_n(\mathbf{k}_{00}) \cdot \hat{\mathbf{k}}_{m00} \right\} \hat{\mathbf{k}}_{m00}$$

where

$$t_{mpq} = \frac{\exp\left\{j\left(\gamma_{pq}^{\text{air}} - \gamma_{pq}^{\text{diel}}\right)s\right\} + R_{mpg} \exp\left\{j\left(\gamma_{pq}^{\text{air}} + \gamma_{pq}^{\text{diel}}\right)s\right\}}{1 + R_{mpq}},$$

$$b_1 = 1, \quad b_2 = 0 \quad \text{for TM incidence,}$$

and

$$b_1 = 0, \quad b_2 = 1 \quad \text{for TE incidence.}$$

1.2.5.2 Examples on a Flat Dielectric Sheet. Most of the applications for telecommunications require circular polarization; therefore, an array of crossed dipoles is a popular choice for the element. The array becomes reflective near the dipole resonance and is almost transparent at lower frequencies. In practice, these surfaces are often constructed by printing metal dipoles on supporting dielectric layers. The exact reflection and transmissions characteristics, therefore, depend on the length, width, and spacing of dipoles; the dielectric constants; and the thickness of the layers. The reflection coefficient is also a function of incident angle. When the application is a dichroic subreflector, there is a range of incident angles on the surface. There are two ways to handle the varying incident angles, by redesigning the element to be reflective at the given incident angle, or, more simply, selecting dimensions for the element that work over the entire range of incident angles. Since the exact resonance frequency is fairly sensitive to the parameters and some of the parameters are not accurately known (dielectric constant of the materials, for example), a flat-sheet test sample is sometimes manufactured and tested to verify the design. A comparison of the calculated and measured reflection coefficient is given below.

A computer program was written for calculating the reflection coefficients for a dipole element using a Fourier expansion in Eq. (1.2-26). Upon comparison with the experimental results, it was found that a three-term expansion of the current on each dipole was sufficient. Thus, for the crossed dipole at the origin we have

$$\begin{aligned} \mathbf{h}_1 &= \hat{y} \sqrt{\frac{2}{WL}} \cos(\pi y / L), & \mathbf{h}_2 &= \hat{y} \sqrt{\frac{2}{WL}} \sin(2\pi y / L), \\ \mathbf{h}_3 &= \hat{y} \sqrt{\frac{2}{WL}} \cos(3\pi y / L), & \mathbf{h}_4 &= \hat{x} \sqrt{\frac{2}{WL}} \cos(\pi x / L), \\ \mathbf{h}_5 &= \hat{x} \sqrt{\frac{2}{WL}} \sin(2\pi x / L), & \mathbf{h}_6 &= \hat{x} \sqrt{\frac{2}{WL}} \cos(3\pi x / L), \end{aligned}$$

The computed reflection coefficient for $L=0.97$ cm, $d=0.92$ cm, and $W=1.016$ mm is shown in Fig. 1-10. Fig. 1-10(a) assumes an absence of the dielectric ($\epsilon_r=1$, $s=0$), and Fig. 1-10(b) is with a sheet of dielectric constant $\epsilon_r=4.25$ and thickness $s=0.127$ mm. Figure 1-10(c) shows the measured reflection coefficient of an experimental surface with the same parameters as used in the computation of the curves of Fig. 1-10(b). This experimental surface is shown in Fig. 1-11, and the method of measurement is described in [28]. As

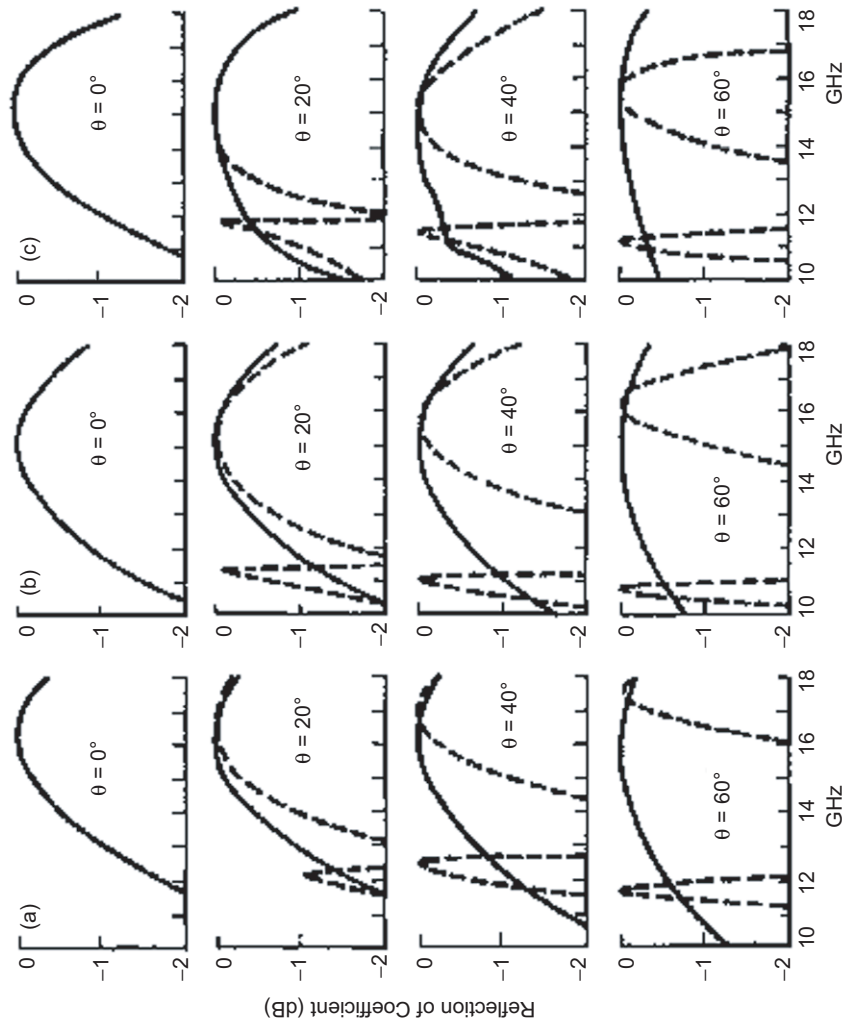


Fig. 1-10. Computed and measured reflection coefficient, —TE, ---TM: (a) theory $\epsilon_r = 1$, $s = 0$ mm; (b) theory $\epsilon_r = 4.25$, $s = 0.127$ mm; and (c) experiment $\epsilon_r = 4.25$, $s = 0.127$ mm.

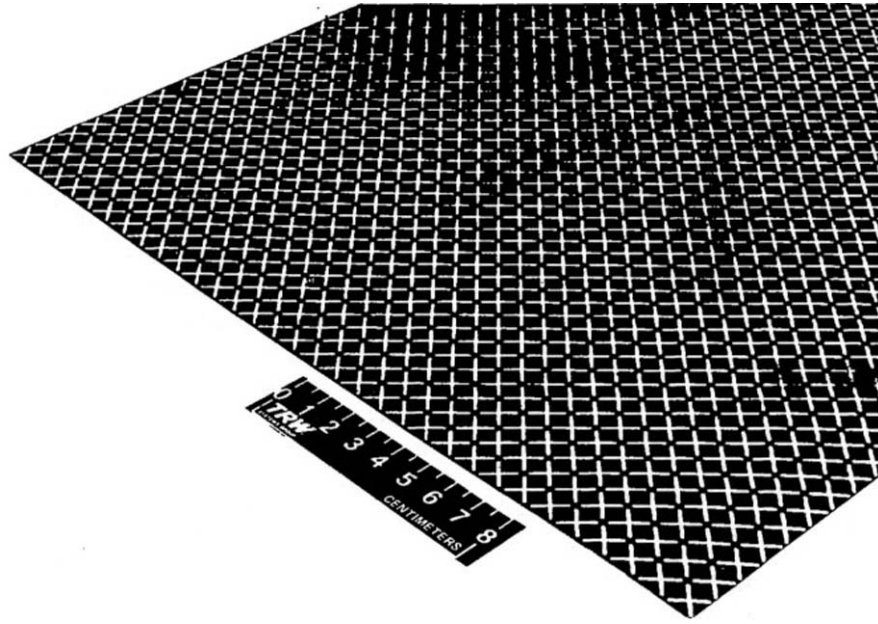


Fig. 1-11. Experimental dichroic surface of copper dipoles printed on 5-mil Kapton sheet ($s = 0.127$ mm).

can be seen in Fig. 1-10, the theoretical results are in close agreement with the experiment. A major influence of the dielectric sheet appears to be in lowering the resonance frequency at which the surface becomes a perfect reflector.

1.2.6 Mesh Analysis

The use of a mesh for the surface of a reflector antenna is a very attractive solution for large deployable antennas such as those on the Tracking and Data Relay Satellite System (TDRSS) and the Galileo spacecraft. These mesh surfaces are typically constructed from gold-plated molybdenum wires, which are woven in a periodic pattern. A commonly used pattern is the tricot knit. The fineness of the wires (typically 1.2 mil [$31\ \mu\text{m}$] in diameter) and the complexity of the weave made the problem of an exact numerical diffraction analysis quite formidable. Nonetheless, Imbriale, Galindo and Rahmat-Samii [31] solved the problem using a Floquet-mode expansion to establish an integral equation for the mesh wire currents that was solved using the method of moments technique with piecewise triangular basis functions. It was observed that it was necessary to give special attention to the junction treatment among different branches of the mesh configuration. For analytic convenience, the mesh was modeled as flat strips on a plane surface. This does not limit the validity of the results since the wire diameters are so small that there are only longitudinal currents. An

equivalent radius of one-fourth the strip width is used to equate round wire and flat strips.

1.2.6.1 Theoretical Formulation. Since the tricot weave is essentially periodic, Floquet's theorem can be applied in the analysis of a plane wave incident upon the mesh. Currents induced along the strip are modeled as a series of overlapping triangular basis functions (splines)—the coefficients of each triangle to be determined by inversion of the matrix obtained when tangential \mathbf{E} is set to zero on the flat strips.

The multiwire junction points are carefully modeled so that the currents are naturally continues through the junctions and no additional conditions are necessary. Conditions of good electrical contact, no contact, or partial contact at the junctions are included in the model. Finite conductivity can be included as well.

The formulation follows very closely the development described in the previous section on dichroic surfaces. In fact, using Floquet's theorem and the method of moments results in the identical set of equations to be solved, i.e., Eq. (1.2-27). The differences stem from the different basis functions used in the formulation and the fact that medium 2 is air instead of a dielectric. However, if the dielectric constant is included in the formulation, the resulting computer code can also be used to analyze dichroic surfaces. In addition, it allows experimental verification of the computer code by comparing with various flat-strip meshes printed on a dielectric sheet.

As indicated above, the reflection and transmission coefficients are computed using Eq. (1.2-29). The major difference in the formulation is the representation of the currents to be used in Eq. (1.2-26).

The actual curved strip is represented as a series of straight segments. The currents are modeled as piecewise triangular along the strip and constant in the transverse direction. The geometry is shown in Fig. 1-12. In particular the currents on the n th segment are

$$\begin{aligned} h_n(x', y') &= \hat{\mathbf{x}}' \frac{(x' + l)}{wl}, \quad -l \leq x' \leq 0, \quad -\frac{w}{2} \leq y' \leq \frac{w}{2} \\ \mathbf{h}_n(x', y') &= \hat{\mathbf{x}}' \frac{(l - x')}{wl}, \quad 0 \leq x' \leq l, \quad -\frac{w}{2} \leq y' \leq \frac{w}{2} \end{aligned} \quad (1.2-30)$$

where

$$x = x_n + x' \cos \Psi - y' \sin \Psi, \quad y = y_n + x' \sin \Psi + y' \cos \Psi.$$

By substituting Eq. (1.2-30) into Eq. (1.2-28) and integrating, we obtain

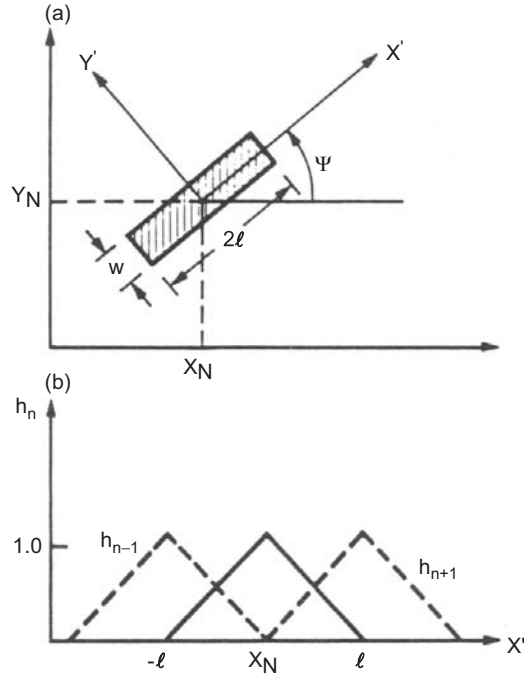


Fig. 1-12. Basic function geometry: (a) geometry of n th segment and (b) triangular basis function.

$$\mathbf{g}_{npg} = \mathbf{g}_{npq}^- + \mathbf{g}_{npq}^+$$

where

$$\begin{aligned} g_{npq}^- &= \hat{\mathbf{x}}' e^{jC} \left[\left(\frac{1}{Z^2} - \frac{jl}{Z} \right) e^{jlz} - \frac{1}{Z^2} \right] \frac{\sin \frac{Vw}{2}}{\frac{Vw}{2}} \times \frac{e^{-jlk}}{l} \\ g_{npq}^+ &= \hat{\mathbf{x}}' e^{jC} \left[\left(\frac{1}{Z^2} - \frac{jl}{Z} \right) e^{-jlz} - \frac{1}{Z^2} \right] \frac{\sin \frac{Vw}{2}}{\frac{Vw}{2}} \cdot \frac{e^{jlk}}{l} \end{aligned} \quad (1.2-31)$$

with

$$Z = k_x \cos \Psi + k_y \sin \Psi,$$

$$V = -k_x \sin \Psi + k_y \cos \Psi, \text{ and } C = k_x x_n + k_y y_n.$$

The complete solution for reflectivity is thus obtained by first using Eq. (1.2-31) and Eq. (1.2-28) and solving for the unknown coefficients c_n using Eq. (1.2-27), and then using the c_n in Eq. (1.2-29) to compute reflectivity.

At the bends in the wire and at wire junctions, special treatment is required to insure that the analytical model provides for the vector continuity of current from one segment to the next segment.

If the vector continuity is not provided, then the current along the strip “senses” a termination of the conductor, and the coefficient of the end point basis function goes to zero.

Setting tangential \mathbf{E} equal to zero is the *only constraint* required if current continuity is insured in the *vector* sense by the addition of a “wedge” current as illustrated in Fig. 1-13.

The *wedge* current in Fig. 1-13a is represented by

$$\mathbf{h}_n = \frac{-\hat{\mathbf{x}} \sin \Psi + \hat{\mathbf{y}} \cos \Psi}{w}. \quad (1.2-32)$$

This is a circular current of constant amplitude as depicted in Fig. 1-13(a). We need to evaluate g_{npq} for this segment. The result is

$$g_{npq} = e^{jC} \int_{\Psi_{n-1}}^{\Psi_n} \left[\frac{-\hat{\mathbf{x}} \sin \Psi + \hat{\mathbf{y}} \cos \Psi}{w} \right] \cdot \left[\frac{e^{jZw} - jZwe^{jZw} - 1}{Z^2} \right] d\Psi \quad (1.2-33)$$

where the integration is carried out numerically with C and Z is as described above.

At the junction of more than one strip, a superposition of all possible wedge currents is required. For example, if two strips cross and make contact, then this junction is treated as a four “port” with six interconnecting wedges necessary to permit current flow from any given strip to any other strip. In general, for N' strips at a common junction point,

$$\left[(N'-1) + (N'-2) + \cdots \right] = \left[\frac{N'(N'-1)}{2} \right]$$

wedge currents are required.

Figure 1-13(b) illustrates a crude schematic of three wire strips meeting at a junction. Hence $N' = 3$ and three connecting “wedge” currents are required. Since wire 3 connects *straight* into wire 2, one wedge current, \mathbf{I}_{32} , degenerates into a *straight connecting section*. Current \mathbf{I}_{c2} and \mathbf{I}_{c3} are circular currents.

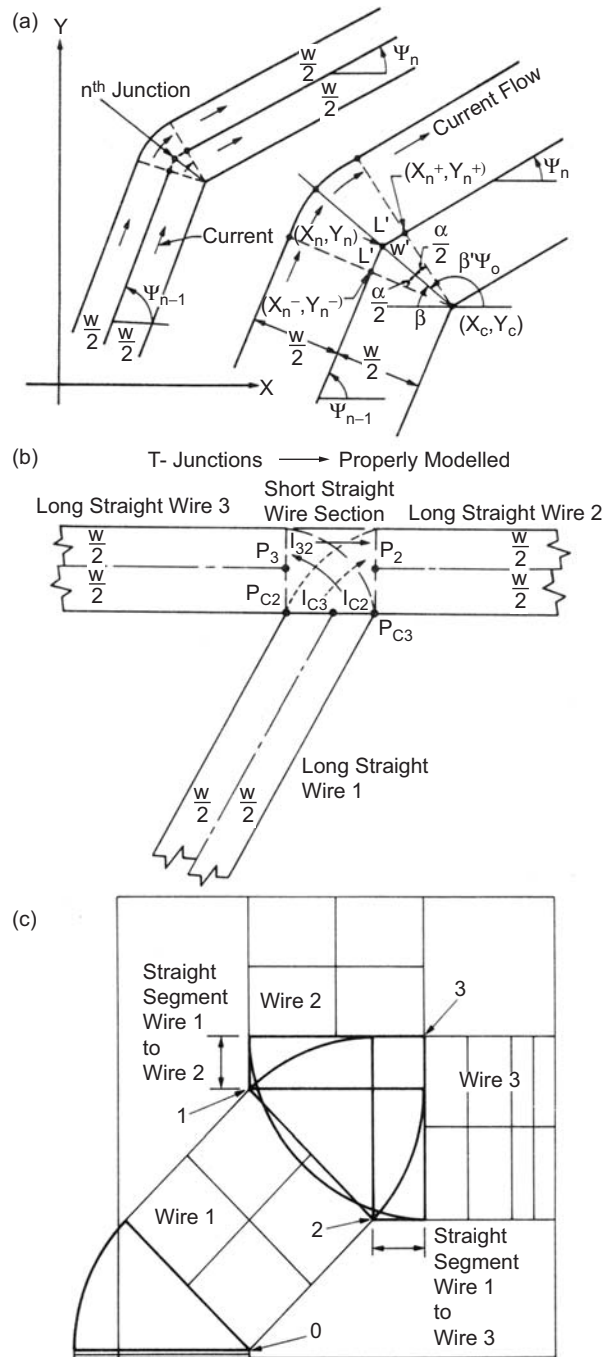


Fig. 1-13. Wire junction geometry: (a) wire bend geometry, (b) three strips meeting at a junction, and (c) General three wire junction with connecting straight sections.

In order to use simple cylindrical currents in the wedge segment, as described earlier, it is necessary to introduce some additional “straight connecting segments” into the geometry. This is illustrated in the three-wire junction of Fig. 1-13(c). The lower left of the figure contains a simple two-wire junction (i.e., a bend) wherein the current wedge is easily introduced and centered at point 0 in the figure.

For the three-wire junction, two straight segments must be introduced in order to use circular wedge currents. For an N' wire junction, we need $(N' - 1)$ straight wire connecting segments at the junction. Figure 1-13(c) indicates the required two straight segments. The cylindrical wedge currents are centered at points 1, 2, and 3 (P_1, P_2, P_3) in the figure. The \mathbf{g}_{npq} for these segments are readily evaluated. It is not necessary to introduce an additional unknown for each connecting straight segment.

A number of examples, including experimental results to validate the theory, are given in reference [31].

1.2.6.2 Galileo Mesh Calculations. The mesh that was used on both the Galileo high-gain antenna and the TDRSS single access antennas was a complex tricot knit, with 10 openings per inch (4 openings per centimeter) and a 1.2-mil (31- μm) diameter wire. Since the analysis uses a flat strip model and the actual mesh is composed of round wire, it was necessary to demonstrate equivalence between wires and strips. It was shown in [31] that the equivalent radius is one-fourth of the strip width. Using the equivalent radius and the complex mesh geometry (shown in Fig. 1-14), a computation for the Galileo type mesh is shown in Fig. 1-15, along with the measured reflectivity at 8 and 15 GHz. In Fig. 1-15 it was assumed that all the junctions make perfect contact, as is the case if there is no corrosion or oxides on the wires. It has been experimentally observed, that under certain unfavorable conditions, a loss of mesh reflectivity of several dB can occur. This has been attributed to lack of electrical contact at the junctions and occurs in part because the tricot knit has wires predominantly in one direction. This phenomenon is further discussed in [31].

1.3 Wire Antennas

William A. Imbriale

Since the dipole antenna is a very simple and lightweight antenna, many of the early spacecraft made use of such antennas (Explorer I for example). For some of the same reasons small rovers and instruments also make use of simple wire-type antennas. For completeness on the analysis tools, this section provides a short summary on the analysis of wire antennas. There are many papers and textbooks that describe the use of the method of moments for the

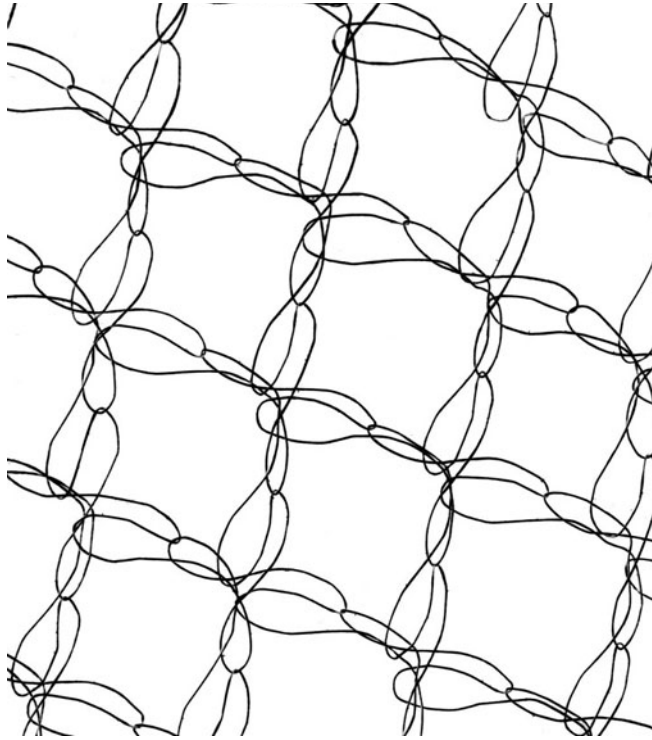


Fig. 1-14. Complex tricot knit geometry.

solution of wire antennas, with [32] probably the classic reference. The following formulation follows the development given in [33] and [34].

1.3.1 Theoretical Formulation

In the moments solution the method of subsectional basis functions is applied with both the expansion and testing functions being sinusoidal distributions. This allows not only a simplification of near-field terms but also the far-field expression of the radiated field from each subsegment, regardless of length. Sinusoidal basis functions are extremely useful for the analysis of large arrays of dipoles since the use of one subsegment per dipole is equivalent to the induced electromotive force (EMF) method of calculating mutual impedances and therefore give a physically meaningful result. For an array of N dipoles, this allows the use of the minimum matrix size of $N \times N$ to achieve a good “first order” approximation to the solution.

1.3.1.1 Basic Theory. Figure 1-16 shows a straight section of wire of circular cross section and defines the coordinate system. The wire with radius a extends from $z = 0$ to $z = L$ along the z -axis. It is assumed that the radius is small

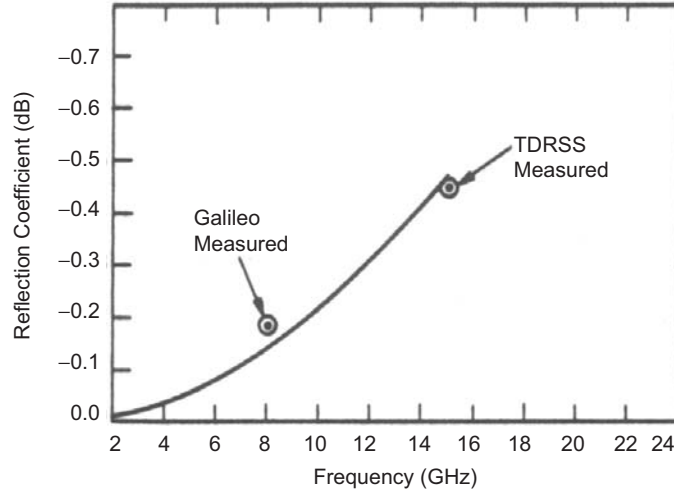


Fig. 1-15. Computed and measured Galileo mesh reflectivity.

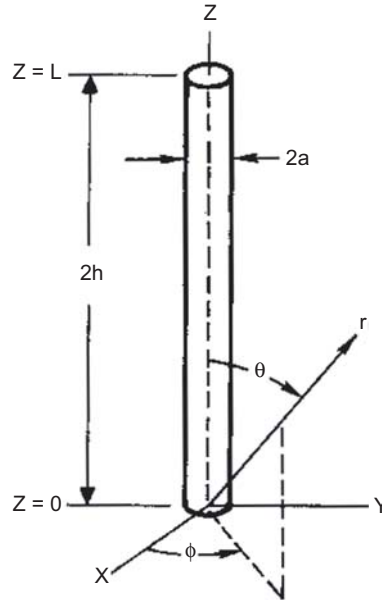


Fig. 1-16. Straight wire and coordinate system.

compared to a wavelength, but the ratio of a to L need not be small. The only significant component of current on the wire is the axial component, which can be expressed in terms of the net current $I(z)$ at any point z along the wire. The current distribution is modeled as an infinitely thin sheet forming a tube of

radius a , with the density of current independent of the circumferential position on the tube. An integral equation for the problem is given by

$$L\{I(z)\} = j(4\pi\omega\epsilon)^{-1} \left(d^2 / dz^2 + k^2 \right) \oint_c \int_0^L \left[\exp(-jkR) / R \right] \cdot I(z') dz' dc = E_z^i(z) \quad (1.3-1)$$

where $E_z^i(z)$ is the z component of the impressed electrical field at the wire surface, $I(z')$ is surface current density, $\oint_c dc$ represents the integration around the circumference, R is the distance from the source point to the field point, and L is a shorthand notation for the integral operator.

The integral equation is solved using the method of moments with sinusoidal subsectional currents and Galerkin's method [34].

Let the wire be broken up into N segments (each of length $2H$, and let $I(z)$ be expanded in a series of sinusoidal functions

$$I(z) \approx \sum_{n=1}^{N-1} I_n S(z - nH), \quad (1.3-2)$$

where I_n are constants and

$$S(z) = \begin{cases} \sin k(H - |z|), & |z| < H \\ 0, & |z| > H \end{cases}.$$

Substitute Eq. (1.3-2) into Eq. (1.3-1), multiply each side by $S(z - mH)$, $m=1,2,\dots,N-1$ and integrate from z to L on z . This results in the matrix equation

$$[Z][I] = [V] \quad (1.3-3)$$

where the elements of $[I]$ are I_n , those of $[Z]$ are

$$Z_{mn} = \int_0^L S(z - mH) L\{S(z - nH)\} dz \quad (1.3-4)$$

and those of $[V]$ are

$$V_m = \int_0^L S(z - mH) E_z^i(z) dz. \quad (1.3-5)$$

Inverting the $[Z]$ matrix to solve for $[I]$ and substituting in Eq. (1.3-2) gives the solution for the unknown current.

In solving thin wire antennas, the integration around the current tube is normally removed by replacing the integral with the value of the integrand at one point. This then reduces the equation to a single integral and obviates the singularity of the integrand, which occurs when the source and field points coincide during the calculation of the self and first adjacent mutual terms. The singularity is, of course, integrable; and by suitably expanding the integrand, special series for these terms can be obtained and the integral performed in closed form. However, many authors have used an “average” value equal to the radius a . This approximation is described as assuming the current to be totally located on the center axis and the distance a is used to represent an average distance from the current filament to the true current surface. A thorough discussion of this singularity and its effect on numerical convergence is given in [33]. However, if the radius is sufficiently small and the number of subsegments limited to the condition when a/H is small, then this approximation is sufficient. The Z_{mn} term for an infinitely thin current filament is given as

$$Z_{mn} = 30 \int_{H_{m-1}}^{H_{m+1}} [-j \exp(-jkR_1)/R_1 - j \exp(-jkR_2)/R_2 + 2j \cos kH_n \cdot \exp(-jkR_0)/R_0] \cdot \sin[k(H_m - |z|)] dz, \quad (1.3-6)$$

where R_1 and R_2 are the distances from the end points, and R_0 the distance from the center of subsegment H_n to the field point on H_m when integrating over subsegment H_m . For the self-term and the first adjacent subsegment where the source and field terms coincide, the impedance term is computed by separating the source and field E by the radius a .

1.3.1.2 Far-Field Evaluation. The radiation pattern of a wire antenna is obtained by superposition of the fields of the many small subsegments with sinusoidal current distributions. Utilizing the general expression for the electric field of a subsegment of any half-length H oriented along the z -axis the far-zone field is given by

$$E(\theta, \phi) = j\eta(4\pi r)^{-1} \exp(-jkr) \sum_{n=1}^N I_n [\cos(kH \cos \theta) - \cos kH] \cdot \exp(jk\eta H) / \sin \theta \hat{u}_\theta, \quad (1.3-7)$$

where η is the intrinsic impedance of free space and \hat{u}_θ is a unit vector.

The power gain pattern of the radiation field is

$$g(\theta, \phi) = 4\pi r^2 \eta^{-1} |E(\theta, \phi)|^2 / P_{in}, \quad (1.3-8)$$

where P_{in} is the power input to the antenna

$$P_{in} = \text{Re}[\tilde{V}][I^*], \quad (1.3-9)$$

where $[\tilde{V}]$ denotes the transpose of $[V]$, and $*$ denotes conjugation.

1.3.2 Arbitrarily Shaped Wires and Wire Junctions

The procedure for solving arbitrarily shaped wires is similar to that used for straight wire as the wire is divided into subsections, over each of which a sinusoidal current distribution is assumed, and a generalized impedance matrix $[Z]$ obtained to describe interactions between subsections. The junction of two or more straight segments can be thought of as the intersection of two or more half subsegments superimposed on one another. Thus, Kirchhoff's current law is not invoked at the junction; it is a consequence of Maxwell's equations.

To complete the description of arbitrarily shaped wires we need to obtain the mutual impedances between two full subsegments, between a full subsegment and a half subsegment, and between two half subsegments. The details for computing these impedance terms are given in [34].

1.4 Microstrip Antenna: Analysis, Design, and Application

John Huang

1.4.1 Introduction

Since the invention of the microstrip antenna a half-century ago [35,36], the demand for its application [37–43] has been increasing rapidly, especially within the past two decades. Because of microstrip antennas' many unique and attractive properties, there seems to be little doubt that they will continue finding many applications in the future. These properties include low profile, light weight, compact and conformable to mounting structure, easy to fabricate, and integratable with solid-state devices. Although, the microstrip antenna is well known for its shortcoming of narrow bandwidth, recent technology advances have improved its bandwidth from a few percent to tens of percent. To understand a microstrip antenna's performance and to simplify its design process, several numerical analysis techniques have been developed and converted to computer-aided-design (CAD) tools. Some of these analysis techniques also allow the designer to know the physical insight of the antenna's electrical operating mechanism. It is the purpose of this section to discuss some of the microstrip antenna's technical features, its advantages and disadvantages,

as well as its material considerations for space application. Analysis techniques, design processes, and CAD tools are briefly presented. Several spacecraft applications of the microstrip antenna are also highlighted.

1.4.2 Technical Background

This subsection presents the technical background of the microstrip antenna, which is separated into three areas: features of the microstrip antenna, advantage and disadvantage tradeoffs, and material considerations.

1.4.2.1 Features of the Microstrip Antenna. A microstrip antenna [44,45], as shown in Fig. 1-17, consists of a radiating metallic patch or an array of patches situated on one side of a thin, nonconducting, substrate panel with a metallic ground plane situated on the other side of the panel. The metallic patch is normally made of thin copper foil or is copper-foil-plated with a corrosion resistive metal, such as gold, tin, or nickel. Each patch can be designed with a variety of shapes, with the most popular shapes being rectangular or circular. The substrate panel generally has a thickness in the range of 0.01 to 0.05 free-space-wavelength (λ_0). It is used primarily to provide proper spacing and mechanical support between the patch and its ground plane. It is also often used with high dielectric-constant material to load the patch and reduce its size. The substrate material should be low in insertion loss with a loss tangent of less than 0.005, in particular for large array application. Generally, substrate materials [45] can be separated into three categories in accordance with their dielectric constant:

- 1) Having a relative dielectric constant (ϵ_r) in the range of 1.0 to 2.0. This type of material can be air, polystyrene foam, or dielectric honeycomb.
- 2) Having ϵ_r in the range of 2.0 to 4.0 with material consisting mostly of fiber-glass reinforced Teflon.
- 3) With an ϵ_r between 4 and 10. The material can consist of ceramic, quartz, or alumina.

Although there are materials with ϵ_r much higher than 10, one should be careful in using these materials. As is discussed later, they can significantly reduce the antenna's radiation efficiency.

A single microstrip patch can be excited either by a coaxial probe or by a microstrip transmission line as shown in Fig. 1-17. For an array of microstrip patches, the patches can be combined either with microstrip lines located on the same side of the patches or with microstrip-lines/striplines designed on separate layers placed behind the ground plane. For the separate-layer configuration, each patch and its feed line are electrically connected either by a small-diameter metal post or by an aperture-coupling slot [46]. Regardless of the different layer configurations, tens or hundreds of patch elements in an array can be fabricated

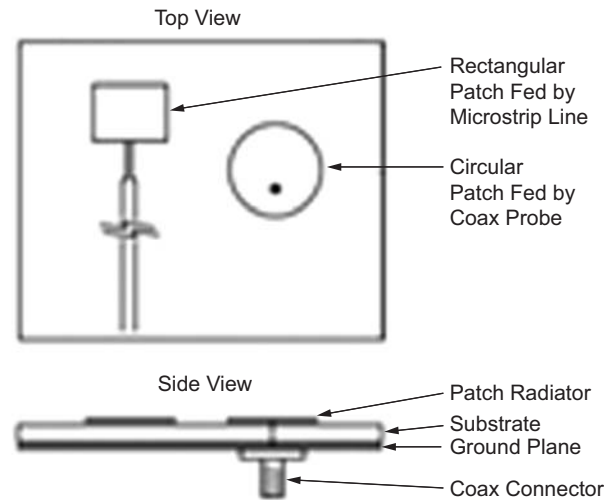


Fig. 1-17. Rectangular and circular microstrip patch antenna configurations.

by a single low-cost chemical etching process, and each single patch element does not need to be fabricated individually (as many other types of radiating elements do), which will lead to an overall lower antenna manufacturing cost.

1.4.2.2 Advantage and Disadvantage Trade-offs. There are advantages as well as disadvantages associated with the microstrip antenna. By understanding them well, one can readily design a microstrip antenna with optimum efficiency, minimum risk, and lower cost for a particular application.

The advantages of microstrip antennas when compared to conventional antennas (helix, horn, reflector, etc.) are:

- The extreme low profile of the microstrip antenna makes it lightweight, and it occupies very little volume of the structure or vehicle on which it is mounted. It can be conformally mounted onto a curved surface so it is aesthetically appealing and aerodynamically sound. Large aperture microstrip arrays on flat panels can be made mechanically foldable for space applications [47,48].
- The patch element or an array of patch elements, when produced in large quantities, can be fabricated with a simple etching process, which can lead to greatly reduced fabrication cost. The patch element can also be integrated or made monolithic with other microwave active/passive components.
- Multiple-frequency operation is possible by using either stacked patches [49] or a patch with a loaded pin [50] or a stub [51].

- There are other miscellaneous advantages, such as the low antenna-radar cross section (RCS) when conformally mounted on aircraft or missiles, and the microstrip antenna technology can be combined with the reflectarray technology [52] to achieve very large aperture requirement.

The disadvantages of the microstrip antennas are:

- The microstrip antenna generally has a narrow bandwidth of less than 5 percent. However, with technology advancement, up to 50 percent bandwidths have been achieved. Some of the techniques used are multiple stacked patches, thicker substrates with aperture slot coupling [53,54], external matching circuits [55], a sequential rotation element arrangement [56,57], parasitic coupling [58], U-slot feed [59], and L-shaped probe feed [60]. It is generally true that wider bandwidth is achieved with the sacrifice of increased antenna physical volume.
- The microstrip antenna can handle relatively lower RF power due to the small separation between the radiating patch and its ground plane (equivalent to small separation between two electrodes). Generally, a few tens of watts of average power or less is considered safe. However, depending on the substrate thickness, metal edge sharpness, and the frequency of operation, a few kilowatts of power for microstrip lines at X-band have been reported [61]. It should be noted that for space application, the power-handling capability is generally less than that for ground application due to a mechanism called multipacting breakdown [62].
- The microstrip array generally has a larger ohmic insertion loss than other types of antennas of equivalent aperture size. This ohmic loss mostly occurs in the dielectric substrate and the metal conductor of the microstrip line power-dividing circuit. It should be noted that a single patch element generally incurs very little loss because it is only a one-half wavelength long. The loss in the power-dividing circuit of a microstrip array can be minimized by using several approaches, such as the series feed power-divider lines [45, 63], waveguide and microstrip combined power dividers, and honeycomb or foam low-loss substrates. For very large arrays, transmit/receive (T/R) amplifier modules can be used on elements or subarrays to mitigate the effect of large insertion loss.

1.4.2.3 Material Consideration. The purpose of the substrate material of a microstrip antenna is primarily to provide mechanical support for the radiating patch elements and to maintain the required precision spacing between the patch and its ground plane. With higher dielectric constant of the substrate material, the patch size can also be reduced due to a loading effect to be discussed later. Certainly, with reduced antenna volume, higher dielectric

constant also reduces bandwidth. There is a variety of types of substrate materials. As discussed in Section 1.4.2.1, the relative dielectric constant of these materials can be anywhere from 1 to 10. Materials with dielectric constants higher than 10 should be used with care. They can significantly reduce the radiation efficiency by having overly small antenna volumes. The most popular type of material is Teflon-based with a relative dielectric constant between 2 and 3. This Teflon-based material, also named PTFE (polytetrafluoroethylene), has a structure form very similar to the fiberglass material used for digital circuit boards, but it has a much lower loss tangent or insertion loss. The selection of the appropriate material for a microstrip antenna should be based on the desired patch size, bandwidth, insertion loss, thermal stability, cost, etc. For commercial application, cost is one of the most important criteria in determining the substrate type. For example, a single patch or an array of a few elements may be fabricated on a low-cost fiberglass material at the L-band frequency, while a 20-element array at 30 GHz may have to use higher-cost, but lower loss, Teflon-based material. For a large number of array elements at lower microwave frequencies (below 15 GHz), a dielectric honeycomb or foam panel may be used as substrate to minimize insertion loss, antenna mass, and material cost with increased bandwidth performance. A detailed discussion of substrate material can be found in reference [45].

1.4.2.3.1 Space Application. When a microstrip antenna is used in space, its substrate material must survive three major effects related to the space environment: radiation exposure, material outgassing, and temperature change. These effects are separately discussed below.

Radiation exposure. Exposure to cosmic high-energy radiation is an important factor in space applications. Cosmic radiations, such as beta, gamma, and X-rays, are similar to nuclear radiation in many respects. They can damage materials after the prolonged exposure typical of a long space mission. The most popular substrate material, as discussed earlier, for the microstrip antenna is the Teflon-based PTFE. This material is generally combined with glass microfibers or ceramic filler to strengthen its mechanical properties. In either case, the component that is most susceptible to space radiation exposure damage is the PTFE. This is because of the low cohesive forces between PTFE molecular chains [64,65]. The primary effect of radiation on PTFE is the reduction of molecular weight by breaking the large polymer molecule into smaller parts. Oxygen is essential to some of the possible radiation induced reactions. Thus, the damage due to radiation is minimized in an oxygen-free environment such as space. The effect of molecular weight reduction is primarily on mechanical properties. There will be an increase in brittleness and reduction in tensile strength, modulus, and elongation. The electrical properties, such as dielectric constant and loss tangent, are also affected by electrical charge distributions in the resin which decays with time; and thus, the radiation

dose rate is important. The degree to which PTFE is affected is essentially a function of the amount of energy absorbed and is generally regardless of the types of radiation. For examples, beta, gamma, X-ray, etc. all have about the same effect. The radiation dose unit is the “rad” with one rad being equal to 100 ergs/gram. Table 1-2 is a summary of radiation doses in rads related to damage levels to PTFE.

Frequently, the dose rate of 10 rads/hour is quoted for the Van Allen Radiation Belt. At this rate, PTFE could operate for 5 to 50 years before a threshold level of damage would occur.

Material outgassing. Outgassing is another phenomenon that needs to be concerned when flying material in space. Outgassing causes a material to lose its mass in the form of gases or volatile condensable matter when subject to a vacuum, especially when it is heated as the antenna is exposed to sunlight in space. Losing mass will certainly affect the material’s mechanical and electrical properties. Several substrate materials manufactured by Rogers Corporation have passed the outgassing test and are approved for space usage. Rogers’ composites of PTFE with either glass microfibers, ceramic filler, or Thermoset Microwave Material (TMM) temperature stable hydrocarbon have all shown outstanding resistance to outgassing (see Table 1-3), according to data

Table 1-2. Radiation amount in rads for damage to PTFE material.

	In Air	In Vacuum
Threshold level	$2-7 \times 10^4$	$2-7 \times 10^5$ or more
50% tensile strength remains	10^6	10^7 or more
Retains 100% elongation	$2-5 \times 10^5$	$2-5 \times 10^6$

Table 1-3. Outgassing test results of Rogers substrate material.

Material Type	Rogers Duroid 5870	Rogers Duroid 5880	Rogers Duroid 6002	Rogers Duroid 6010	TMM 3	TMM 10
Material Composition	PTFE with Glass Microfiber	PTFE with Glass Microfiber	PTFE with Ceramic Filler	PTFE with Ceramic Filler	Thermoset Polymer Composite	Thermoset Polymer Composite
Dielectric constant	2.3	2.2	2.9	10.0	3.0	10.0
% TML	0.05	0.03	0.02	0.03	0.04	0.06
% CVC	0.0	0.0	0.01	0.0	0.0	0.0
% WVR	0.04	0.02	0.01	0.02	0.03	0.04

compiled by NASA test procedure SP-R-0022A [66,67]. The test procedure consists of vacuum heating of 100- to 300-mg specimens in an enclosure. The total mass loss (TML), collected volatile condensable materials (CVCM), and water vapor recovered (WVR) are expressed as a percentage of the original specimen mass. In general, materials with a TML greater than 1 percent or a CVCM greater than 0.1 percent should be avoided in space application.

Temperature change. The effect of temperature in space on electrical and physical properties of the substrate material must be taken into consideration when designing a microstrip antenna. Since the space is a vacuum without conduction medium, the temperature of an object could be extremely cold, e.g., -100 deg C, when it is not exposed to the sunlight or it could become very hot, e.g., $+100$ deg C, when it is directly illuminated by the Sun over a period of time. The effects of these extreme temperatures could cause change to the microstrip substrate material include dielectric constant (ϵ) and substrate thickness, which will together cause an impedance change of the microstrip patch or transmission line. Table 1-4 gives examples of the expected response of microstrip transmission line to temperature change [45,68] for both non-woven-glass PTFE and ceramic-loaded PTFE.

In addition to the above two substrate materials, Rogers corporation developed a substrate material that is very insensitive to temperature changes and is named the Thermoset Microwave Material (TMM). It is a highly filled inorganic resin composite with tightly controlled dielectric constant value. Over a temperature range of ± 100 deg C, the TMM only changed its dielectric constant value by less than 0.5 percent. At the high temperature of 300 deg C, the TMM exhibited a thermal expansion amount of 1/3 of that of the PTFE material. This TMM is highly recommended for space applications where there is a concern regarding wide ranges of temperature variation.

Table 1-4. Example of microstrip substrate property change vs. temperature change in vacuum.

Temperature (deg C)	Percent Change from 20 deg C Value; Frequency = 18 GHz, 50-ohm Line					
	Non-Woven-Glass PTFE			Ceramic-Loaded PTFE		
	Thickness	ϵ	Impedance	Thickness	ϵ	Impedance
-100	-1.31	1.36	-1.60	-0.26	5.06	-2.2
-60	-0.89	1.02	-1.20	-0.19	3.38	-1.4
+70	1.31	-0.53	1.20	0.15	-2.27	1.0
+110	2.37	-0.87	2.20	0.19	-3.42	1.6
+150	3.42	-1.50	3.40	0.26	-4.47	2.0

1.4.3 Analysis, Design, and CAD Tools

1.4.3.1 Analysis Techniques. The main reason for developing an analytic model for the microstrip antenna is to provide a means of designing the antenna without costly and tedious experimental iteration. Also, it may help the designer to know the physical mechanisms of how the microstrip antenna operates. With an analysis technique, the engineer should be able to predict the antenna performance qualities, such as the input impedance, resonant frequency, bandwidth, radiation patterns, and efficiency. There are many different analysis techniques that have been developed for analyzing the microstrip antennas. However, the most popular ones can be separated into four groups: transmission-line circuit model, multimode cavity model, moment method, and finite difference time domain (FDTD) approach. They are briefly discussed below:

1.4.3.1.1 Transmission-Line Circuit Model. A microstrip patch, operating at its fundamental mode, is essentially a $\frac{1}{2}\lambda$ -long microstrip transmission line and can be represented by an equivalent circuit network [69,70]. For a rectangular or square patch, its radiation is basically generated from its two edges with two equivalent slots along the resonating dimension, as shown in Fig. 1-18. Thus, the microstrip radiator can be characterized by two slots separated by a transmission line, where each slot is represented by a parallel circuit of conductance (G) and susceptance (B). The complete patch antenna can be represented by the equivalent network shown in Fig. 1-19 [69]. This transmission line model is simple, intuitively appealing, and computationally fast, but it suffers from limited accuracy. For examples, this model lacks the radiation from the non-radiating edges of the patch, and it has no mutual coupling between the two radiating slots. Although, this model has led to a much improved version [70], it lacks the flexibility and generalization of analyzing other shapes of patches.

1.4.3.1.2 Multimode Cavity Model. Any microstrip radiator can be thought as an open cavity bounded by the patch and its ground plane. The open edges can also be represented by radiating magnetic walls. Such a cavity will support multiple discrete modes in a manner similar to that of a completely enclosed metallic cavity. As an example, for a rectangular patch with relatively dielectric constant of ϵ_r , substrate thickness of h , and patch dimensions of $w \times l$ as that shown in Fig. 1-18, its total electric field in the cavity can be expressed as the sum of the fields associated with each sinusoidal mode [71]:

$$E_z(x, y) = \sum_m \sum_n C_{mn} \cdot \cos\left(\frac{m\pi}{w}\right)x \cdot \cos\left(\frac{n\pi}{l}\right)y \quad (1.4-1)$$

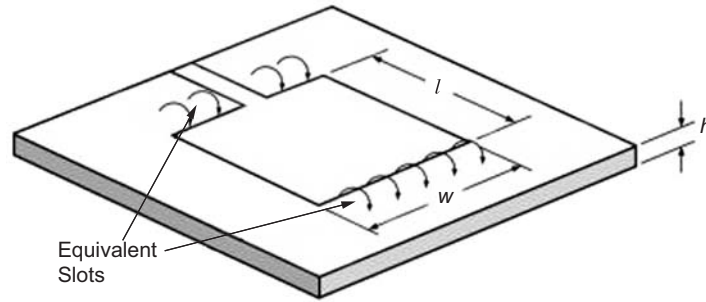


Fig. 1-18. Microstrip patch with two equivalent radiating slots.

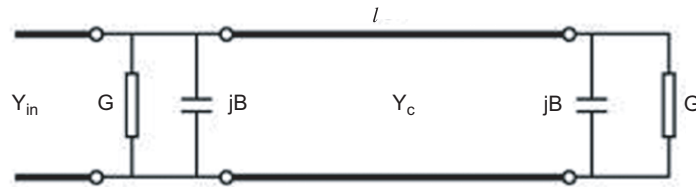


Fig. 1-19. Equivalent network of microstrip patch element.

where C_{mn} is a constant that depends on the feed location, w and l dimensions, and the dielectric constant. Due to the very thin substrate, the fields are assumed to be z -directed only with no variation in the z -direction. The most important dominant mode is the TM_{10} mode, which can be obtained if the dimension l is approximately $\lambda_g/2$ (λ_g is the effective wavelength in the dielectric). By knowing the fields at the edges of the patch, the equivalent edge magnetic currents can be determined and integrated to find the far-field radiation patterns. By knowing the total radiated power and the input power, one can also determine the input impedance. The cavity model technique allows one to know the mode structure underneath the patch; and therefore, its physical mechanisms are more easily understood, such as its resonating and cross-polarization behaviors. However, because it assumes the field has no z -variation, its solution is not very accurate; in particular, when the substrate becomes thick (for wider bandwidth consideration). Also the calculation of mutual coupling between patches in an array environment is very tedious and not accurate.

1.4.3.1.3 Moment Method. The radiated fields of a microstrip antenna can be determined by integrating all the electrical currents on its metallic surfaces via the integral equation approach whose solution is obtained by the so-called moment method. This integral equation approach [72–75] is analyzed by first

solving the vector potential $\vec{A}(x,y,z)$ which satisfies the wave equation with J_s being the patch surface current:

$$\nabla^2 \vec{A}^I + k^2 \vec{A}^I = -j\omega J_s(x,y) \quad \text{in the dielectric (region I)} \quad (1.4-2)$$

and

$$\nabla^2 \vec{A}^{II} + k_0^2 \vec{A}^{II} = 0 \quad \text{in the free space (region II)} \quad (1.4-3)$$

then the vector potential may be given as

$$\vec{A}^{I,II}(x,y,z) = \iint_{\text{patch}} \vec{J}_s(x',y') \cdot \vec{\vec{G}}^{I,II}\left(\frac{x,y,z}{x',y',z'}\right) dx', dy' \quad (1.4-4)$$

where $\vec{\vec{G}}^{I,II}$ is the dyadic Green's function for regions I and II. Region I contains the substrate, while region II being the free-space area above the substrate. The electric field \vec{E} everywhere is given by

$$\vec{E}(x,y,z) = -j\omega \vec{A} + \frac{j\omega}{k^2} \vec{\nabla}(\vec{\nabla} \cdot \vec{A}) \quad (1.4-5)$$

By weighting the Green's function of Eq. (1.4-4) with the unknown electrical current density and integrating over the patch, the radiated electric or magnetic field can be calculated anywhere outside the dielectric. An integral equation for the unknown current is obtained by forcing the total tangential electric field on the patch surface to zero. Using the proper basis and testing functions for the unknown current, the integral equation is then discretized and reduced to a matrix equation:

$$[E] = [Z_{mn}] [J] \quad (1.4-6)$$

where the impedance matrix element has the form:

$$Z_{mn} = \int_x \int_y \int_{x'} \int_{y'} \int_{k_x} \int_{k_y} J^m(x,y) \cdot G(k_x, k_y) \cdot J^n(x',y') \cdot e^{-jk_x(x-x')} \cdot e^{-jk_y(y-y')} dk_y dk_x dy' dx' dy dx \quad (1.4-7)$$

where $G(k_x, k_y)$ is the Fourier transform of the Green's function given in Eq. (1.4-4), J^m is the m th expansion mode, and J^n is the n th weighting or testing mode. Equation (1.4-7) has been solved by two different approaches. One uses the space domain approach [74,75], where the spectral variables k_x

and k_y are transformed to spatial polar coordinates α and β . The other approach uses the spectral domain approach [72,73] where the spatial integrations in Eq. (1.4-7) are done in closed form, which results in an integral in spectral domain only. Nevertheless, both approaches are derived to solve, via the method of moment and matrix inversion, for the patch surface current, which is then used to determine the properties of the microstrip antenna, such as the input impedance and radiation patterns. The moment method, a two-dimensional integration technique, is considered very accurate and includes the effects of mutual coupling between two surface current elements as well as the surface wave effect in the dielectric. It is computationally more time consuming than the transmission-line model and the cavity model. However, it is more computationally efficient than the three-dimensional technique to be discussed in the following subsection.

1.4.3.1.4 Finite-Difference Time-Domain (FDTD) Method. The previous moment method is basically a two-dimensional solver. It solves for the 2-D surface current on the microstrip patch. The FDTD method, on the other hand, is a three-dimensional solver. It solves for the electromagnetic fields in a 3-D volumetric space. Thus, it can solve more complex problems with 3-D interfaces and connections, such as the multi-layer microstrip antenna with complicated multi-layer connections. However, it suffers from laborious computation time, and it is not suitable (with current computer capability) for solving large microstrip array problems. The FDTD method [76–78] uses Yee's algorithm [79] to discretize Maxwell's equation in three-dimensional space and in time. The volume-space of interest is discretized into many cubes, and the E and H fields are then solved through Maxwell equations with given boundary conditions from cube to adjacent cubes. This is illustrated briefly in the following Maxwell's curl equations:

$$\mu \cdot \frac{\partial H}{\partial t} = -\nabla \times E \quad (1.4-8)$$

$$\epsilon \cdot \frac{\partial E}{\partial t} = \nabla \times H \quad (1.4-9)$$

With time and space discretized, the E- and H-fields are interlaced within the spatial 3-D grid. For example, Eq. (1.4-9) can be discretized for the x-directed E field:

$$E_x^{n+1}(i, j, k) = E_x^n(i, j, k) + \frac{\Delta t}{\varepsilon} \left[\frac{H_z^{n+1/2}(i, j+1, k) - H_z^{n-1/2}(i, j, k)}{\Delta y} \right] - \frac{\Delta t}{\varepsilon} \left[\frac{H_y^{n+1/2}(i, j, k+1) - H_y^{n-1/2}(i, j, k)}{\Delta z} \right] \quad (1.4-10)$$

where Δx , Δy , and Δz are the space steps in the x -, y -, and z -directions, and Δt is the time step. The same discretization can be carried out for Eq. (1.4-8).

Now, Maxwell's equations have been replaced by a set of computer-recognizable finite-difference equations, which can be solved sequentially from cube to cube once the known boundary conditions are applied. Certainly, this cube-to-cube solver cannot continue indefinitely outside the volume of interest and must be terminated. However, the fields will bounce back from any terminating boundary (which does not happen in reality) and disturb the correct solution. The solution is to use the electromagnetic absorbing boundaries to be set up outside the areas of interest and to absorb all outgoing fields. One significant advantage of the FDTD method is that, by discretizing time, one is able to see on a computer screen how the field is actually traveling and radiating in time sequence in a complicated antenna/circuit configuration.

1.4.3.2 Design Methodology. The previous section presented different techniques to analyze the microstrip antenna. To ease the design process, these different analysis techniques have been developed into several user-friendly computer-aided-design (CAD) tools by several institutions. However, an analysis technique or a CAD tool, by itself, cannot generate an antenna design. It can only analyze a design and provide calculated performance results for a design. The basic antenna design has to originate from human experience, knowledge, and innovation, even though an optimal and accurate design often cannot be achieved without an analysis tool. Figure 1-20 depicts a typical microstrip antenna development process. The block labeled "Computer Analysis Software" represents the central processing unit into which a human must enter the proper design data to initiate the design process. The block labeled "Antenna Design Techniques" represents the knowledge for generating a set of preliminary input design data, which is the main subject of this section. It includes techniques to design array configurations, patch elements, and power division transmission lines, which are separately discussed in the following subsections.

1.4.3.2.1 Array Configuration Design. Before performing a detailed design, it is critically important to lay out the most suitable array configuration for a particular application. Array configuration variables include series feed or parallel feed, single layer versus multiple layers, substrate thickness, dielectric

constant, array size, patch-element shape, element spacing, etc. The selection of the proper configuration depends upon many factors, such as the required antenna gain, bandwidth, insertion loss, beam angle, grating/sidelobe level, polarization, and power-handling capability. Several important microstrip array configurations that often challenge the skills of antenna designers are presented below.

Series feed. In a series feed configuration [45,80], multiple elements are arranged linearly and fed serially by a single transmission line. Multiples of these linear arrays can then be connected together serially or in parallel to form a two-dimensional planar array. Figure 1-21 illustrates two different configurations of the series feed method. The in-line feed [81,82] has the transmission line serially connected to two ports of each patch and is sometime called the two-port series feed. The out-of-line feed [63] has the line connected to one port of each patch and is thus called one-port series feed. The in-line

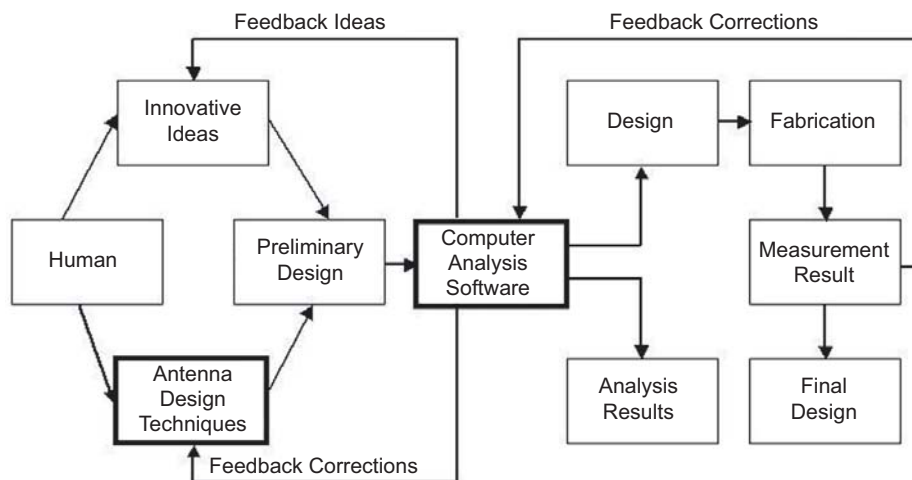


Fig. 1-20. Microstrip antenna development procedures.

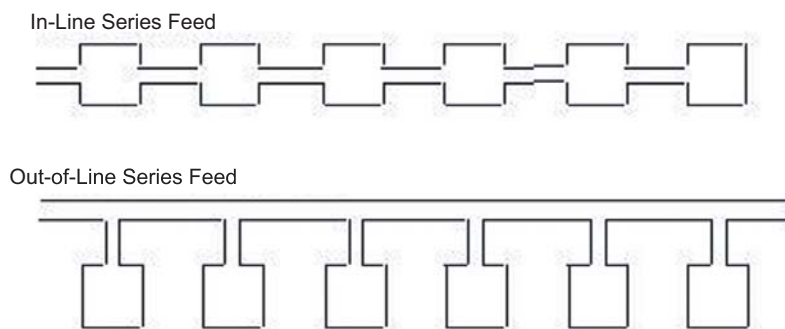


Fig. 1-21. Series-fed microstrip arrays.

feed array occupies the smallest real estate with the lowest insertion loss, but it generally has the least polarization control and the narrowest bandwidth. The in-line feed, as shown in Fig. 1-21, is generally more suitable for generating linear polarization than circular polarization. It has the narrowest bandwidth because the line goes through the patches, and, thus, the phase between adjacent elements is not only a function of line length but also of the patches' input impedances. Since the patches are amplitude weighted with different input impedances, the phases will be different for different elements and will change more drastically as frequency changes due to the narrow-band characteristic of the patches.

The series feed can also be classified into two other configurations: resonant and traveling-wave [45,80]. In a resonant array, the impedances at the junctions of the transmission lines and patch elements are not matched. The elements are spaced multiple integrals of one wavelength apart so that the multiply bounced waves, caused by mismatches, will radiate into space in phase coherence in the broadside direction. Because of this single- or multiple-wavelength element spacing, the beam of the resonant array is always pointed broadside. For the same reason, the bandwidth of a resonant array is very narrow, generally less than 1 percent. With a slight change in frequency, the one-wavelength spacing no longer exists, thereby causing the multiply bounced waves not to radiate coherently but, instead, to travel back to the input port as mismatched energy. Both the in-line and out-of-line feed arrays can be designed to be of the resonant type.

For the traveling-wave array type, the impedances of the transmission lines and the patches are generally all matched, and the element spacing can be one wavelength for broadside radiation, or less than one wavelength for off-broadside radiation. Because the energy travels toward the end of the array without multiple reflections, there is generally a small amount of energy remaining after the last element. This remaining energy can be either absorbed by a matched load or reflected back to be re-radiated in phase for broadside radiation [63]. The array can also be designed such that the last element radiates all of the remaining energy [63]. The traveling-wave array has a wider impedance bandwidth, but its main beam changes in direction as frequency changes. A general rule-of-thumb for the frequency-scanned beam of a traveling-wave array is one degree of beam scan per one percent of frequency change. For an instantaneous wideband signal, such as a pulsed system, a beam broadening effect will occur. Both the in-line and out-of-line series-fed arrays of Fig. 1-21 can be designed as the traveling-wave type. There are also other forms of series-fed microstrip arrays: chain, comb line, rampart line, Franklin, and coupled dipole [45,80]. These arrays operate similarly to the arrays shown in Fig. 1-21, except that they use microstrip radiators with different radiating mechanisms.

Parallel feed. The parallel feed, also called the corporate feed [83], is illustrated in Fig. 1-22. In the parallel feed, the patch elements are fed in parallel by the power-division transmission lines. The transmission line divides the power into two branches, and each branch divides again until it reaches the patch elements. In a broadside-radiating array, all the parallel division lines have the same length. For a series-fed array, the insertion loss is generally less than that of a parallel-fed array because most of the insertion loss occurs in the transmission line at the first few elements, and very little power remains at the end of the array. Most of the power has already been radiated by the time the end elements are reached. Despite its higher insertion loss, the parallel-fed array does have one significant advantage over the series-feed, which is its wideband performance. Since all elements in a parallel-fed array are fed by equal-length transmission lines, when the frequency changes, the relative phases between all elements will remain the same; and thus, no beam squint will occur. The bandwidth of a parallel-fed microstrip array is limited by two factors: the bandwidth of the patch element and the impedance matching circuit of the power-dividing transmission lines, such as the quarter-wave transformer. Whereas a series-fed array can only achieve a bandwidth of 1 percent or less, a parallel-fed array can achieve a bandwidth of 15 percent or more.

Hybrid series/parallel feed. An example of a hybrid series/parallel-fed array is depicted in Fig. 1-22, where a combination of series and parallel feed lines is used. In a hybrid array [63], the smaller series-fed subarray has a broader beamwidth, which will suffer only a small gain degradation due to beam squint with frequency change. Hence, a hybrid array will achieve a wider bandwidth than a purely series-fed array having the same aperture size. Of course, because of its partial parallel feed, the insertion loss of hybrid array is higher than that of a purely series-fed array. This hybrid technique gives the

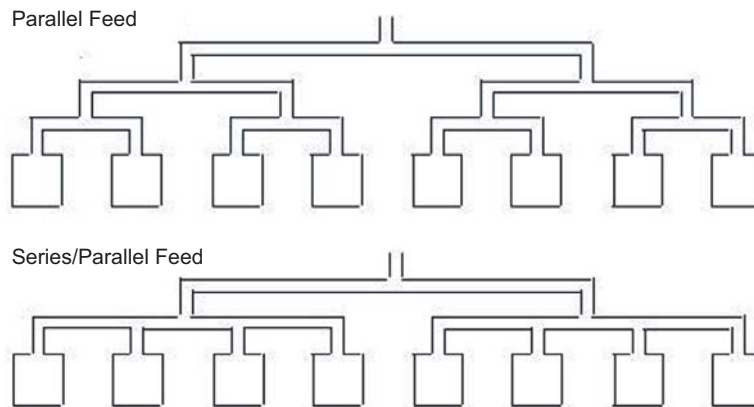


Fig. 1-22. Configurations of parallel feed and hybrid parallel/series feed microstrip arrays.

designer an opportunity to make design trade-offs between bandwidth and insertion loss.

Regardless of whether the array is parallel or series fed, two recently developed arraying techniques can be employed to significantly improve the array's performance. The first is to reduce cross-polarization (cross-pol) radiation in a planar array by oppositely exciting adjacent rows or columns of elements in phase and in orientation [63], as shown in Fig. 1-23(a). Another technique is shown in Fig. 1-23(b) for a circularly polarized array, in which every adjacent four elements placed in a rectangular lattice can be sequentially

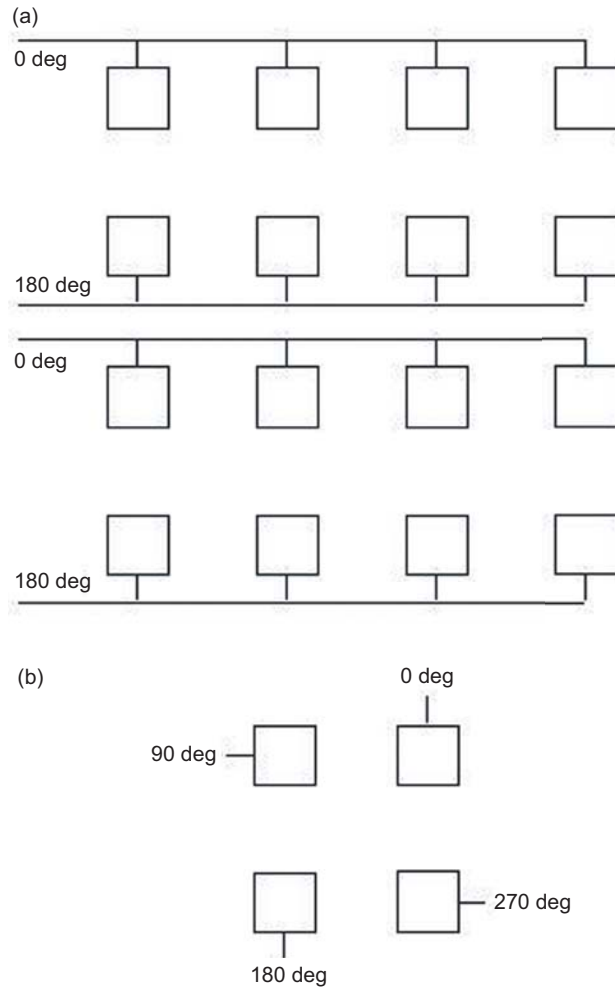


Fig. 1-23. Microstrip array configuration: (a) rows excited by opposite phases and orientations and (b) sequentially arranged four-element subarray.

arranged in both phase and orientation to achieve good circular polarization over a wide bandwidth [56,57].

Single-layer or multilayer design. A microstrip array can be designed in either a single-layer or multilayer configuration. The factors that determine this choice are complexity and cost, sidelobe/cross-pol level, number of discrete components, polarization diversity, bandwidth, and so on. When the given electrical requirements are relaxed, a single-layer design will generally suffice. If all transmission lines and patch elements are etched on the same layer, it will be low in manufacturing cost. However, when extremely low sidelobe or cross-pol radiation (e.g., less than -30 dB) is required, the double-layer design seems to be the better choice. With all transmission lines etched on the second layer behind the radiating patch layer, the ground plane in the middle will shield most of the leakage radiation of the lines from the patch radiation. This leakage radiation becomes more pronounced when discrete components, such as monolithic microwave integrated circuit (MMIC) T/R modules and phase shifters, are placed in the transmission line circuits. Thus, it is more desirable to place all discrete components behind the radiating layer in a multilayer configuration. When dual-linear or dual-circular polarization is required with high polarization isolation, it is often more desirable to design the feed circuits of the two polarizations on two separate layers, as shown in Fig. 1-24. When a radiating patch having a thick substrate is used to achieve wider bandwidth, it is best to design the transmission lines on a separate layer because the lines may become too wide to be practical if designed on the same thick layer as the radiating patches. In other cases, when an extremely wide bandwidth requirement can be met only by using multiple stacked patches [53], the multilayer design becomes the obvious choice. With the advancement of the

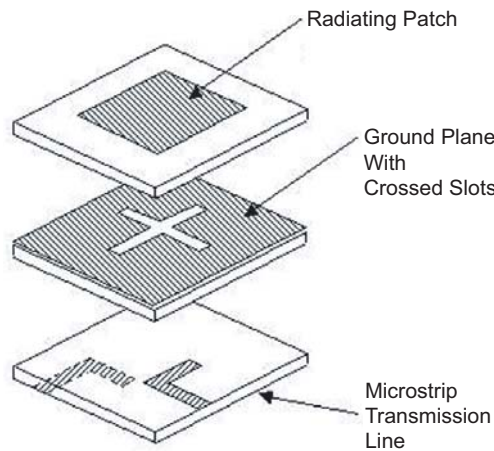


Fig. 1-24. Multilayer dual-polarized microstrip patch element.

aperture-coupling technique that allows the transmission line to feed the patch, the multilayer design becomes much more feasible than those using many feed-through pins.

Other array configuration. When designing a microstrip array, various antenna parameters, such as substrate thickness, dielectric constant, and element spacing, can all play important roles in determining an array's performance. Substrate thickness determines bandwidth, as well as the antenna's power handling capability [61]. The thicker the substrate, the more power it can handle. For ground applications, a thicker microstrip antenna ($>0.05 \lambda_0$ thick) can generally handle several hundred to a few thousand watts of peak power. For space applications, due to the effect of multipacting breakdown [62], only tens of watts are attainable. The dielectric constant of the substrate material also affects the bandwidth: the higher the dielectric constant, the narrower the bandwidth. Because of the loading effect, a higher dielectric constant reduces the patch resonant size and, hence, increases the element beamwidth. A wider element beamwidth is desirable for a large-angle-scanning phased array. Another important array design parameter is element spacing. It is often desirable to design a microstrip array with larger element spacing so that more real estate can be made available for transmission lines and discrete components. However, to avoid the formation of high grating lobes, element spacing is limited to less than $1 \lambda_0$ for broadside beam design and less than $0.6 \lambda_0$ for a wide-angle scanned beam. In designing a wide-angle scanned microstrip phased array, substrate thickness, dielectric constant, and element spacing are all important parameters that need to be considered for reducing mutual coupling effects and avoiding scan blindness [84].

1.4.3.2.2 Patch Element Design. Patch elements come in various shapes, such as rectangular, square, circular, annular ring, triangular, pentagonal, and square or circular with perturbed truncations. These different shapes can often be used to meet various challenging requirements. For example, the rectangular patch, used for linearly polarized applications, can achieve slightly wider bandwidth than the square or circular patch. However, the square or circular patch, unlike the rectangular patch, can be excited orthogonally by two feeds to achieve circular polarization. In addition, the circular patch can be designed to excite higher-order modes for generating different-shaped patterns [85,86]. The pentagonal patch, as well as the square or circular patch with a small perturbation, can be used to generate circular polarization with only a single feed [45], which is often a desirable feature when simplicity and low insertion loss are required.

It should be noted that all of these patch shapes can be accurately analyzed and designed by the full-wave moment method discussed in Section 1.4.3.1.3. However, designing a patch using the moment method or any other rigorous technique requires a priori knowledge of the approximate size of the patch so

that appropriate dimensions, rather than random numbers, can be input to the analysis computer code. With a few iterations of the computer code, the designer should be able to determine the precise dimensions of the microstrip antenna. Once the dimensions are known, other parameters (e.g., input impedance, bandwidth, and radiation patterns) can be accurately computed by the full-wave moment method. The above-mentioned a priori knowledge of the approximate patch size can be acquired through experience, or derived by simple closed-form equations if available. Fortunately, the two most popular and often-used patch shapes, rectangular (or square) and circular, do have simple closed-form equations available. These equations, in predicting the resonant frequency, can generally achieve an accuracy of within 2 percent. For the fundamental-mode rectangular patch, the simple equation [44] is given by

$$f = \frac{c}{2(L+h)\sqrt{\epsilon_e}} \quad (1.4-11)$$

where

$$\epsilon_e = \frac{\epsilon_r + 1}{2} + \frac{\epsilon_r - 1}{2} \left(1 + \frac{12h}{w} \right)^{-1/2} \quad (1.4-12)$$

f is the resonant frequency, c is the speed of light, L is the patch resonant length, h is the substrate height, ϵ_r is the relative dielectric constant of the substrate, and w is the patch non-resonant width.

For the circular patch with TM_{mn} mode, the simple design equation is given by [44,85]

$$f = \frac{\chi_{mn}c}{2\pi a_e \sqrt{\epsilon_e}} \quad (1.4-13)$$

where

$$a_e = a \left\{ 1 + \frac{2h}{\pi a \epsilon_r} \left[\ln \left(\frac{\pi a}{2h} \right) + 1.7726 \right] \right\}^{1/2} \quad (1.4-14)$$

f , c , h , and ϵ_r are as defined for the rectangular patch design equation, a is the patch's physical radius, χ_{mn} is the m th zero of the derivative of Bessel's function of order n , n represents the angular mode number, and m is the radial mode number.

There is no significant difference in performance between the fundamental-mode rectangular patch and a fundamental-mode circular patch. A circular patch does have the advantage of offering higher-order-mode performance with

different diameters and differently shaped radiation patterns [85,86]. These patterns can be either linearly or circularly polarized, depending on the configuration of the feed excitations.

1.4.3.2.3 Power Division Transmission Line Design. One of the principal shortcomings of a microstrip array with a coplanar feed network is its relatively large insertion loss, especially when the array is electrically large or when it is operating at a higher frequency. Most of the losses occur in the power-division transmission line's dielectric substrate at microwave frequencies. At millimeter-wave frequencies, the loss in the copper lines becomes significant. It is thus crucially important to minimize insertion loss when designing the power division transmission lines. In order to minimize insertion loss, the following principles should be observed: The impedances of the power-division lines should be matched throughout the circuit; low-loss material should be used for the substrate; at higher frequencies, the roughness of the metal surfaces that face the substrate should be minimized; and the array configuration should be designed to minimize line length (as described in Section 1.4.3.2.1). This section discusses the impedance-matching techniques for power division circuits. Every designer has a somewhat different approach to design a microstrip circuit, but they all require the knowledge of the fundamental circuit theory and basic equations presented in the following subsections. In a good design with well matched lines, the microstrip circuit will suffer less from mismatch losses and radiation leakage losses. Although most of the microstrip circuit components shown here are very fundamental and have been presented elsewhere in separate articles, they are collected here for microstrip array designs.

A very important circuit component in most microstrip array design is the quarter-wave transformer (see Fig. 1-25), which transforms one impedance to another. The proper impedances for this transformation are given by the following equation:

$$Z_2 = \sqrt{Z_1 \times Z_3}. \quad (1.4-15)$$

In Fig. 1-25, the symbol λ_g is the effective wavelength in the microstrip line, and its equation is given in [87]. This quarter-wave transformer is not only used to transform between two different impedances, but it also should be used where there is a possible impedance mismatch. For example, for the single-patch circuit shown in Fig. 1-26, the quarter-wave section should be used at the coax input feed location and at the input to the patch. At both of these locations, there may be some residual mismatches. For instance, the 250-ohm input impedance of the patch may not be accurately predicted by a CAD due to inaccuracy in the model or inaccurate specification of the dielectric constant by the manufacturer, and the coax feed may not be perfectly matched to the

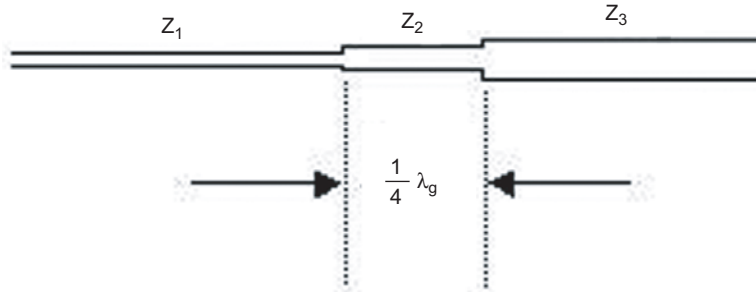


Fig. 1-25. Microstrip quarter-wave impedance transformer.

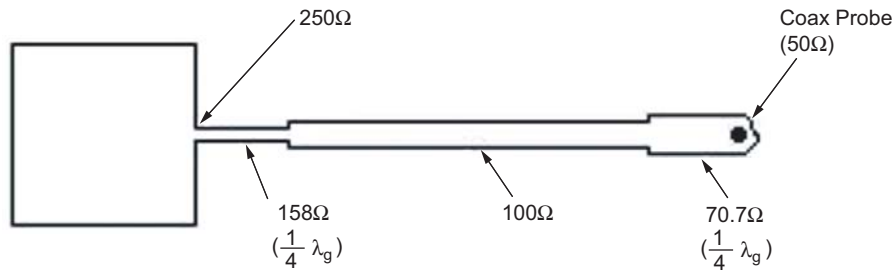


Fig. 1-26. Microstrip line feeding a patch element with impedance-matched quarter-wave sections.

microstrip line due to possible air gap, fabrication tolerance, etc. The quarter-wave transformer can be used to minimize such mismatches. This is because of the quarter-wave line's round-trip phase delay (180 deg), and thus the reflected signal due to mismatch occurring at one location will cancel with that reflected from another location a quarter-wave distance away.

In a microstrip line with a given substrate height and dielectric constant, the width of line governs the characteristic impedance. To determine the microstrip line width with a specified line impedance, simple closed-form equations are given in [87]. These equations are generally accurate enough without resort to a full-wave analysis or a CAD tool, unless there is a significant amount of mutual coupling between lines.

Another important microstrip circuit component used quite often is the two-way power divider illustrated in Fig. 1-27. In this figure, the input power P_1 with microstrip line width W_1 and impedance Z_1 is split into powers P_2 and P_3 with line widths W_2 and W_3 and impedances Z_2 and Z_3 , respectively. The fundamental equations for this simple power division are

$$Z_1 = Z_2 \times Z_3 \div (Z_2 + Z_3), \quad P_2 = (Z_1 / Z_2) \times P_1, \quad P_3 = (Z_1 / Z_3) \times P_1 \quad (1.4-16)$$

$$\text{angle } A = \arctan(W_3 / W_1)$$

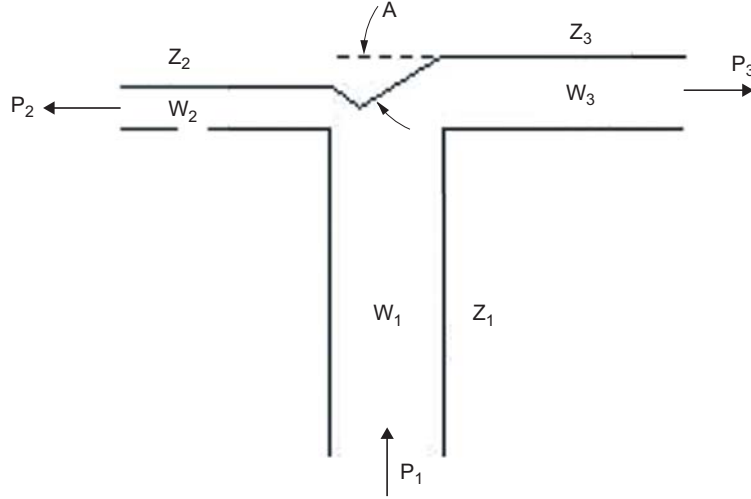


Fig. 1-27. Microstrip two-way power divider.

Since there could be a small amount of impedance mismatch due to fabrication tolerance or other types of inaccuracies, it is more practical, as explained previously, to design the power divider with a quarter-wave transformer as shown in Fig. 1-28.

A three-way power divider, illustrated in Fig. 1-29, can also be designed based on the equations of the two-way power divider. The design equations for this three-way divider are

$$\begin{aligned} Z_1 &= \frac{Z_4 \times Z_s}{Z_4 + Z_s}, & Z_s &= \frac{Z_2 \times Z_3}{Z_2 + Z_3} \\ P_4 &= \frac{Z_1}{Z_4} \times P_1, & P_3 &= \frac{Z_1}{Z_3} \times P_1, & P_2 &= \frac{Z_1}{Z_2} \times P_1 \end{aligned} \quad (1.4-17)$$

With the above equations for the two-way and three-way power dividers, one should be able to derive the equations for any multiple power division with different combinations of power ratios.

The above power dividers are named reactive power dividers because the power divisions are based on the reactive impedances of the lines. In addition to these reactive power dividers, two other types of power dividers are briefly presented here. One is the branch-line hybrid divider shown in Fig. 1-30, and the other is the Wilkinson power divider shown in Fig. 1-31. A reactive power divider does not provide isolation between the divided ports. Any mismatch at the end of a divided port will send portion of the returned power into other

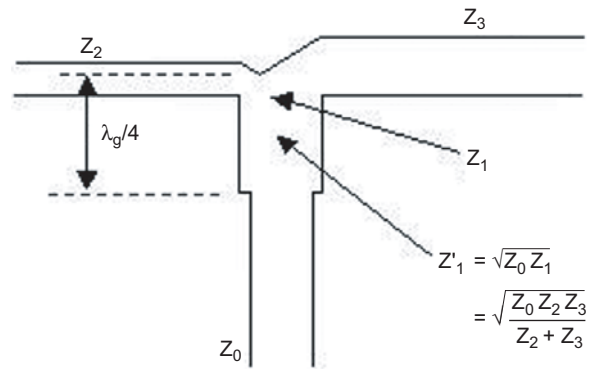


Fig. 1-28. Microstrip two-way power divider with a quarter-wave transformer.

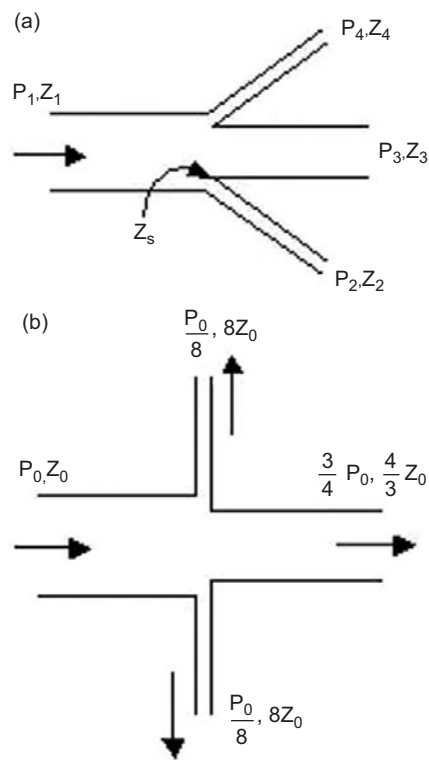
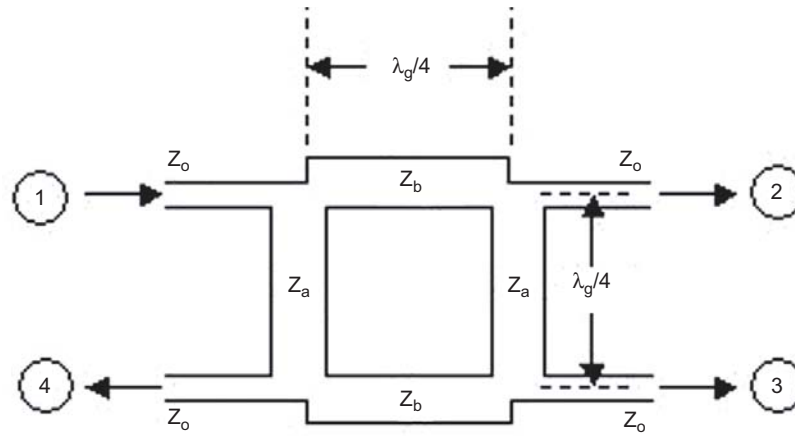


Fig. 1-29. Two methods (a and b) to configure microstrip three-way power dividers.



$$\text{Impedances: } \frac{Z_o}{Z_a} = a; \frac{Z_o}{Z_b} = b$$

$$b^2 - a^2 = 1 \dots\dots \text{Matched Condition}$$

$$\text{Power Ratios: } \frac{P_2}{P_1} = \left(\frac{1}{b}\right)^2; \frac{P_3}{P_1} = \left(\frac{a}{b}\right)^2$$

Fig. 1-30. Microstrip hybrid branch-line power divider.

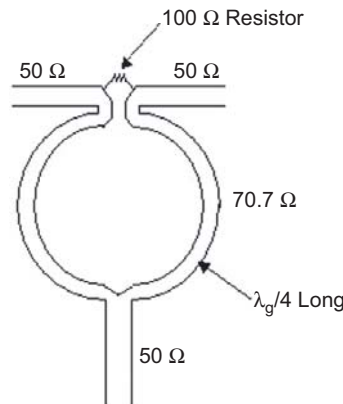


Fig. 1-31. Microstrip Wilkinson power divider.

ports, which can cause high radiated sidelobe and cross-pol levels. Both the branch-line hybrid and the Wilkinson dividers can generally provide more than 20 dB of isolation between divided ports. The branch-line hybrid, in addition to its capability of providing 90-deg phase difference between its two output ports, can also achieve different power divisions. In Fig. 1-30, any mismatch-reflected power from port 2 or 3 will go into the loaded port 4 and not into the input

port 1. For the Wilkinson divider depicted in Fig. 1-31, mismatch-reflected power from the two divided ports will be mostly absorbed by the 100-ohm resistor.

1.4.3.3 CAD Tools. In the previous section, design methodology, a typical microstrip antenna development process is depicted in a block diagram (see Fig. 1-20). Although all CAD tools available today can only provide analysis and not a design, they do assist significantly in achieving the final design. For example, an engineer generates an initial design and then inputs the design dimensions and configuration into a CAD to calculate a set of performance results, such as input return loss and radiation patterns. Generally, the initial results will not meet the given requirements, in particular, for a complicated design. The engineer, using his experience and knowledge, will perform corrections on the design and then input to the CAD again as indicated in Fig. 1-20. This iterative process may take several times until satisfactory results are achieved. Before CAD tools were available, the engineer could only perform hardware verification of the design and might have needed many iterations. This hardware verification step requires significantly longer time with higher cost than computer simulation. For a large array, the cost of iterative hardware verification soars with array size and complexity. Academic researchers have been prolific in generating analytical and numerical solutions for a wide variety of microstrip antennas and arrays, often with a high degree of accuracy and efficiency. But this area of work is generally performed primarily for graduate student theses or publications, and the software are seldom completely written, validated, or documented for other users. Researchers in industry may be more pragmatic when developing comparable solutions for specific antenna geometry, but such software is often considered proprietary.

From the above discussion, there is a clear need for a CAD tool. The first commercial CAD tool for microstrip antennas became available in the early 1990s, and in the past decade, the number of commercial tools has mushroomed with more than ten available in the world. Table 1-5 lists some commercial software packages that can be used for microstrip antenna analysis and design.

Among the CAD tools, the Ensemble and IE3D, that use full-wave moment method, are the most popular. These two PC-based software were on the market much earlier than the other ones for microstrip antenna application. Through up-grades and modifications, they became more efficient, less prone to errors, and with more capabilities. Designs with multilayer, conductive via connections, finite ground plane, etc. can all be accurately analyzed. With a 1-gigabyte (GB) random-access memory (RAM) capability, a current personal computer (PC), by using either Ensemble or IE3D, can handle a microstrip array with approximately 30 elements and some microstrip power-division lines. Some of the other softwares, which use finite difference time domain (FDTD) or finite element (FE) methods, take a three-dimensional approach by

Table 1-5. Some commercially available microstrip antenna CAD tools.

Software Name	Theoretical Model	Company
Ensemble	Moment method	Ansoft
IE3D	Moment method	Zeland
Momentum	Moment method	HP
EM	Moment method	Sonnet
PiCasso	Moment method/Genetic	EMAG
FEKO	Moment method	EMSS
PCAAD	Cavity model	Antenna Design Associates, Inc
Micropatch	Segmentation	Microstrip Designs, Inc.
Microwave Studio (MAFIA)	FDTD	CST
Fidelity	FDTD	Zeland
HFSS	Finite element	Zeland

modeling the entire antenna space, including dielectric, metal components, and some surrounding volume. This approach allows a high degree of versatility for treating arbitrary geometries, including inhomogeneous dielectrics and irregularly shaped structures, but the price paid is computer time. With a current PC, only a few patch elements can be calculated. Regardless of the method used, future advancement in CAD tools is vested in two areas: (1) PCs with high capacity and faster computation; and (2) more efficient mathematical algorithms. With these advancements, large microstrip arrays can be more effectively analyzed and designed.

One important conclusion [88] should be made here for all CAD users that, while CAD software can be an invaluable analysis/design tool, it is not a substitute for design experience or a thorough understanding of the principles of operation of microstrip antennas and arrays. While microstrip antenna design is based on solid science, it also retains a strong component of intuitive understanding and a creative problem-solving approach that can only come from experience. It also can be concluded that, at least for the near future, CAD tools will continue to aid, rather than actually replace, the experienced designers.

1.4.4 Spacecraft Applications

1.4.4.1 Introduction. The demand for microstrip antenna application has been increasing rapidly in the past two decades. Initial applications have been primarily in the defense sector. Because of their extremely thin profiles and lightweight, printed microstrip antennas have found many applications for conformal mounting on military aircraft, missiles, rockets, etc. In the commercial sector, the adoption of microstrip antennas had not been as rapid during the 1980s, primarily due to their relatively higher material cost and the newness of the technology. During the earlier years, the costs of the microstrip antenna's substrate material, design effort, and manufacturing processes were considered non-competitive when compared to monopole, helix, horn, or parabolic reflector antennas. In addition, at the time, the configuration and environment of most terrestrial communication systems did not warrant the use of microstrip antennas. During the past decade, however, the cost to develop and manufacture microstrip antennas has dropped significantly. This is because the maturity of the microstrip antenna technology, the reduction in cost of the substrate material and manufacturing processes, and the simplified design process using newly developed versatile CAD tools. Furthermore, modern communication systems, such as cellular phone and station antennas, benefit greatly from the small size and low profile features of the microstrip antenna. In the space sector, the demand for using microstrip antennas is also increasing, but rather gradually since spacecraft are not produced in large quantities. Because of the increasing demand for smaller spacecraft and high-capability large-aperture antennas, smaller antenna mass to save launch vehicle fuel, and smaller antenna stowage volume to save launch vehicle space, there is an increasing need for more applications of microstrip antennas.

1.4.4.2 JPL/NASA Programs. Starting in the late 1970s, JPL/NASA began using microstrip antennas for space applications. For JPL-related programs, the following spacecraft have used or are using microstrip antennas: Seasat [89], Shuttle Imaging Radar (SIR) – A, B, C series [90,91], Mars Pathfinder, and Mars Exploration Rovers (MER). Among these programs, the antennas for Seasat and the SIR-A, -B, and -C series are all large-panel microstrip arrays (>10-m dimension) operated at L-band and/or C-band frequencies. These antennas are part of the synthetic-aperture radars (SARs) used to perform Earth remote sensing functions. These large arrays, except the SIR-C, are all designed with fixed main beams.

The SIR-C/X-SAR antenna is the most massive piece of hardware (10,500 kg) ever assembled at JPL, and measures 12 m by 4 m. The SIR-C instrument was built by JPL and the Ball Communication Systems Division for NASA and provides the L-band and C-band measurements at different polarizations. The L-band and C-band antennas employ phased-array

technology, which allows the antenna beam pointing to be adjusted electronically. The X-SAR instrument was built by the Dornier and Alenia Spazio companies for the Deutsche Agentur für Raumfahrtangelegenheiten (DARA, German Space Agency) and the Agenzia Spaziale Italiana (ASI, Italian space agency), and it operates at a single frequency, X-band. The X-SAR antenna is a slotted waveguide type ($12\text{ m} \times 0.4\text{ m}$ at the top of Fig. 1-32), which uses a mechanical tilt to change the beam pointing direction.

The SIR-C antenna, flew three times (1994, 1995, and 2000) on the Space Shuttle, has electronic beam scanning capability with solid-state transmit/receive (T/R) modules and phase shifters. The antenna, shown in Fig. 1-32, has separate L-band ($12\text{-m} \times 3\text{-m}$ aperture size) and C-band ($12\text{ m} \times 0.75\text{ m}$ at bottom of Fig. 1-32) microstrip array panels developed by Ball Aerospace Corporation under a JPL contract.

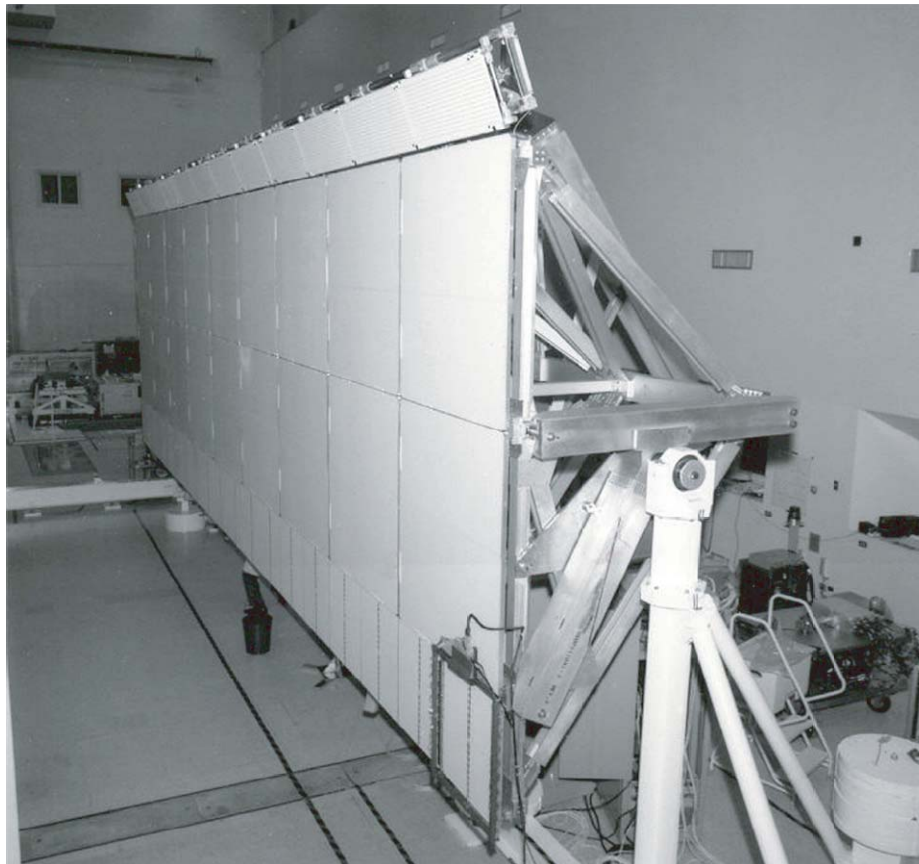


Fig. 1-32. SIR-C antenna in laboratory configuration. (The middle large L-band panels and the bottom small C-band panels are microstrip phased arrays with distributed T/R modules and phase shifters; the top slightly tilted panels are a fixed-beam X-band slotted waveguide array.)

For the Mars Pathfinder program, a relatively small (25-cm diameter) X-band microstrip dipole array, developed by Ball under JPL contract, was used as a telecommunication high-gain antenna on the Mars Pathfinder spacecraft launched in 1996 for Mars exploration. This antenna provided circular polarization with a peak gain of 25 dB. It was constructed with a corporate feed power divider and electromagnetically coupled dipoles, which allowed the antenna to have wide bandwidth and operate at both the transmit frequency of 8.4 GHz and the receive frequency of 7.1 GHz. The divider and the dipoles were printed on multilayer honeycomb substrates with open vented cells for space application. A polarizing cover sheet was used to achieve circular polarization.

Another Mars exploration program launched two MER spacecraft in 2003 to send two rovers to further explore the Mars surface. The two spacecraft successfully landed in late 2003 and in early 2004. On each lander vehicle, there are four petals (protective shielding panels) that opened up after landing to allow the rover to exit. An X-band antenna is mounted on the outside of one of the petals. It sent an indicator signal to Earth to confirm that the lander had landed and was functioning on the Martian surface. This X-band antenna is a single-element square patch with two orthogonal input ports to provide circular polarization. The patch and its microstrip lines are gold plated to avoid moisture corrosion in Earth environment prior to its launch. It is mounted in a circular protective cavity with a protective radome cover. The cavity has a 7-cm diameter, and the complete antenna has a mass of only 20 g. This single-patch antenna provides a peak gain of 7 dB with a -3 dB beamwidth of 85 deg. The microstrip patch antenna was selected for this application because of its unique features of small size and very little mass. Pictures of the Mars Pathfinder and MER microstrip antennas can be found in Chapter 4.

1.4.4.3 Areas of Attention for Space Application. In designing microstrip antennas for space applications, several critical areas need to be considered. In addition to the substrate material's radiation, outgassing, and temperature characteristics (discussed in Section 1.4.2.3.1), there are three other critical areas to be briefly discussed here. One is that the antenna must be able to survive the violent vibration during launch from the Earth. Generally, a vibration shock on the order of 10 gs or more must be tolerated. The soldering points of the coax connectors, via-through-hole connectors, discrete component attachments, and laminating epoxy material between different layers of a multilayer design all need to be made strong enough to survive the vibration.

The second area of attention is the large temperature variations that can occur in space. At an Earth-like distance from the Sun, the temperature can vary between 173 and 373 K (± 100 K). At Venus the temperature can exceed 473 K, and at Jupiter it can get as low as 50 K. A spacecraft like Cassini that uses a gravity assist from Venus to get to Jupiter must be designed for both extremes.

The substrate material, as well as its laminating adhesive material, must survive physically and electrically throughout a wide temperature range over the lifetime of the spacecraft. In particular, the microstrip antenna is a narrow-band device. Its resonant frequency may shift out of the required operating bandwidth and lose its performance due to the temperature change.

The third area of attention is the antenna's RF power-handling capability. The power-handling capability of a microstrip antenna is generally an order of magnitude less in space than in Earth's atmosphere. Due to the vacuum in space, a particular breakdown phenomenon known as multipacting [62] generally occurs at pressures lower than 10^{-2} torr (1.3 Pa). At this low gas pressure, the electrons are freer to leave an electrode and move across to the opposite electrode. For a microstrip antenna, the two electrodes are the patch and its ground plane. Thus, in order to handle higher power in space, the microstrip antenna or microstrip transmission line must be designed with the proper thickness. The thicker it is, the more power it can handle. For a patch with conventional thickness ($<0.02 \lambda_0$), a few tens of watts or less may be considered to be safe in space. For more than 50 watts of average power, one should perform theoretical power breakdown analyses [62] and actual high-power-in-vacuum tests.

1.4.5 Summary and Conclusion

In this chapter, the design methodologies and various analysis techniques for microstrip antennas have been presented. In particular, the full-wave moment method is the most popular technique due to its computation accuracy and efficiency. Practical design techniques for the array configuration, radiating patch element, and power-division lines have been thoroughly discussed. Commercial available CAD tools were also presented. Space applications of microstrip antennas were highlighted. It is expected that, because of their small size and low mass, the demand for microstrip antennas in space applications will continue to increase. On the other hand, there is also an unabated demand for improving the performance of microstrip array antennas, such as widening of the bandwidth, reduction of the insertion loss, and improving the computation efficiency to handle large-size arrays. By utilizing the analysis techniques and design methods presented in this chapter, in conjunction with innovative ideas, the performance of microstrip antennas can be further enhanced to broaden their applications in the future.

1.5 Antenna Measurements

Mark S. Gatti

One area where spacecraft and ground antennas differ significantly is in the methods used to verify antenna performance parameters. Because of the requirements for low mass and the need to fit into the launch vehicle,

spaceborne antennas are generally small and quite amenable to direct measurements of their antenna radiation patterns. There are even standards written that define such measurements [92]. Two basic techniques have been developed to measure spacecraft far-field antenna parameters. A direct measurement of the far-field pattern can be done if enough distance can be reached between a source antenna and the antenna under test (AUT). In this mode a transmitter can be connected to either antenna, but traditionally, the source antenna is connected to a transmitter that radiates a signal at the frequency or frequencies of interest, and the AUT is connected to a suitable receiver. If the separation distance between the two antennas is sufficient that spherical phase error is negligible, then accurate main-beam and sidelobe measurements of the AUT are possible. This type of measurement is referred to as a “far-field” antenna measurement. An alternate method of determining the far-field antenna performance makes use of the relationship between the field surrounding the antenna on a closed surface at any distance from the antenna and the field at a great distance. One could, for example, measure the entire field around an antenna and use a Fourier relationship to calculate the field at an infinite distance. Typically, the enclosing surface chosen is in the immediate vicinity of the antenna and measures the near-field power of the antenna. The far-field performance of an antenna is calculated using this indirect measurement and is referred to as a “near-field” measurement. Figure 1-33 illustrates both the direct and indirect categories of antenna measurements. This section discusses both of these measurements and how they have been applied to several spacecraft antennas over the past 40 years.

In deciding which technique to use, an antenna engineer must determine the shortest distance that defines the beginning of the far field. Other factors include the ruggedness of the AUT, its total size, compatibility with the environment (for outdoor measurements), deformation in the effects of gravity, etc. Some spacecraft antennas are susceptible to gravity such that they distort. Others can only be rotated around one axis to measure patterns. An example of an antenna that should be tested indoors is a fragile deployable antenna similar to the Galileo high-gain antenna (HGA) (see Chapter 5). The long “stick” antenna used on the NASA Scatterometer and SeaWinds is easily rotated about its long axis, whereas a special fixture is required to rotate about any other axis. Some antennas, such as the HGAs used on the Mariner, Viking, Voyager, Magellan, and Cassini spacecraft, are not only stiff, but are rugged and lend themselves to periodic cleaning of any dust that may accumulate due to being in the outdoors. More flexibility in choosing the type of measurement is allowed for such antennas. Finally, the symmetric properties of the AUT can also be used in determining which type of measurement to be done. Often, rotating the AUT about an axis of mechanical symmetry provides a smaller

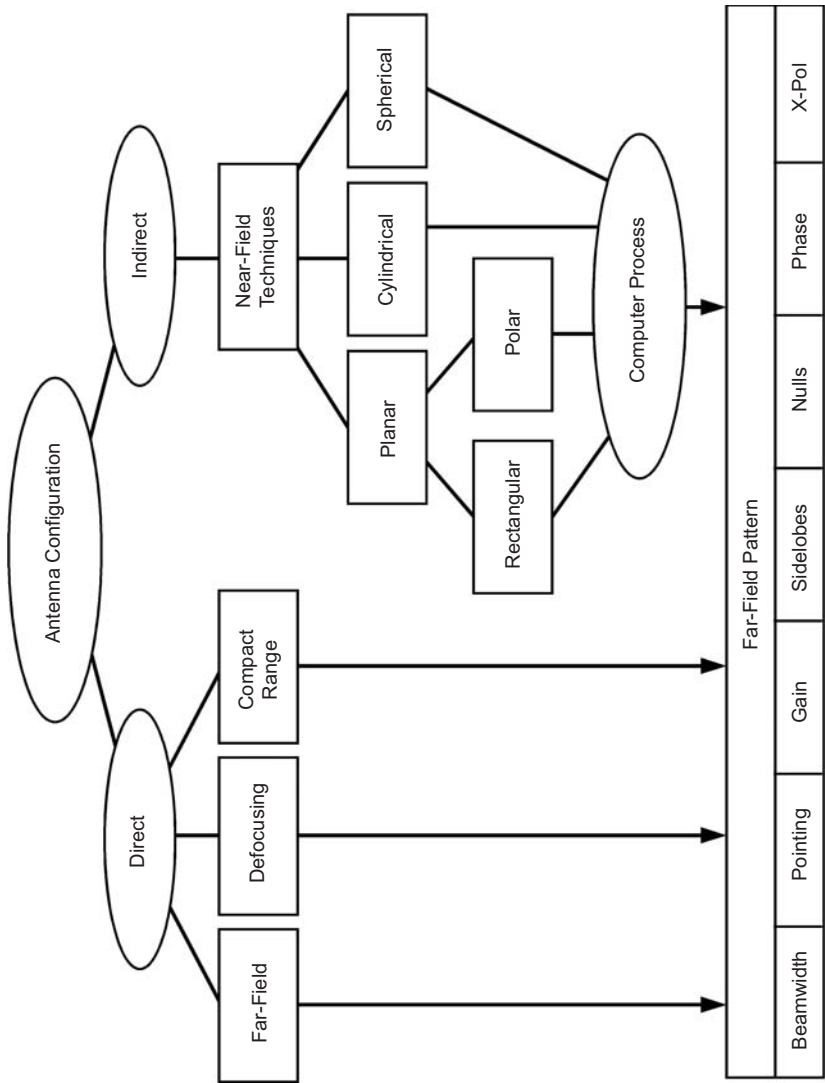


Fig. 1-33. Categorization of measurement techniques for antenna far-field patterns.

total suspended moment and a smaller total size of the required measurement facility.

1.5.1 Far-Field Measurements

The far-field measurement of an antenna's performance is the most straightforward technique as the quantity measured is exactly what is desired. The techniques described in this section are fully developed in great detail in [93] as well as most texts on antenna theory and design. The AUT and another source antenna, either of which can be connected to either a transmitter or receiver, are placed at a distance such that the measurements of the coupled power represent the far-field parameters of the AUT (see Fig. 1-34). This separation distance is somewhat arbitrary; however, it has been shown that the measured parameters very closely match the infinite distance far-field when the phase across the aperture of the antenna is less than 22.5 deg (equivalently 1/16 of a wavelength). This minimum separation is at a distance defined by the *largest* antenna in the measurement (either the AUT or the source antenna), and is given by $2D^2/\lambda$ where λ is the wavelength of the measurement and D is the diameter of the *largest* antenna in the measurement setup. For microwave antennas this can be quite far, ranging from 100–1000 meters. Finally, when making far-field measurements, one has to be aware that the reflection off objects between the source antenna and AUT will effect the measurement. The main error comes from the reflection off the ground between the antennas. Other reflections include the towers that the antennas are mounted on as well as other structures. Careful test-range design and characterization are required before an antenna should be calibrated on any far-field range. Typical difficulties with far-field antenna ranges are the huge real estate required, the uncontrolled environment (especially for fragile spacecraft antennas), the unbalanced gravitational forces, and the ground reflections. Nevertheless, for many spacecraft antennas a far-field range measurement is the most direct method to verify antenna performance.

1.5.1.1 Antenna Pattern Measurements. For this discussion, assume that the source antenna is transmitting a signal at the frequency or frequencies of interest. Furthermore, assume that this source antenna is of the same polarization as the AUT. Alternatively, the source antenna can be of linear polarization regardless of the AUT's polarization. The AUT is connected to an appropriate receiver and detector to measure the power received from the transmitter. To measure the patterns of the AUT, it is often mounted on a fixture such that it can be rotated about (or close to) the phase center. In doing so the measured power is directly proportional to the antenna pattern. Figure 1-34 shows such a configuration. For this measurement, one can either

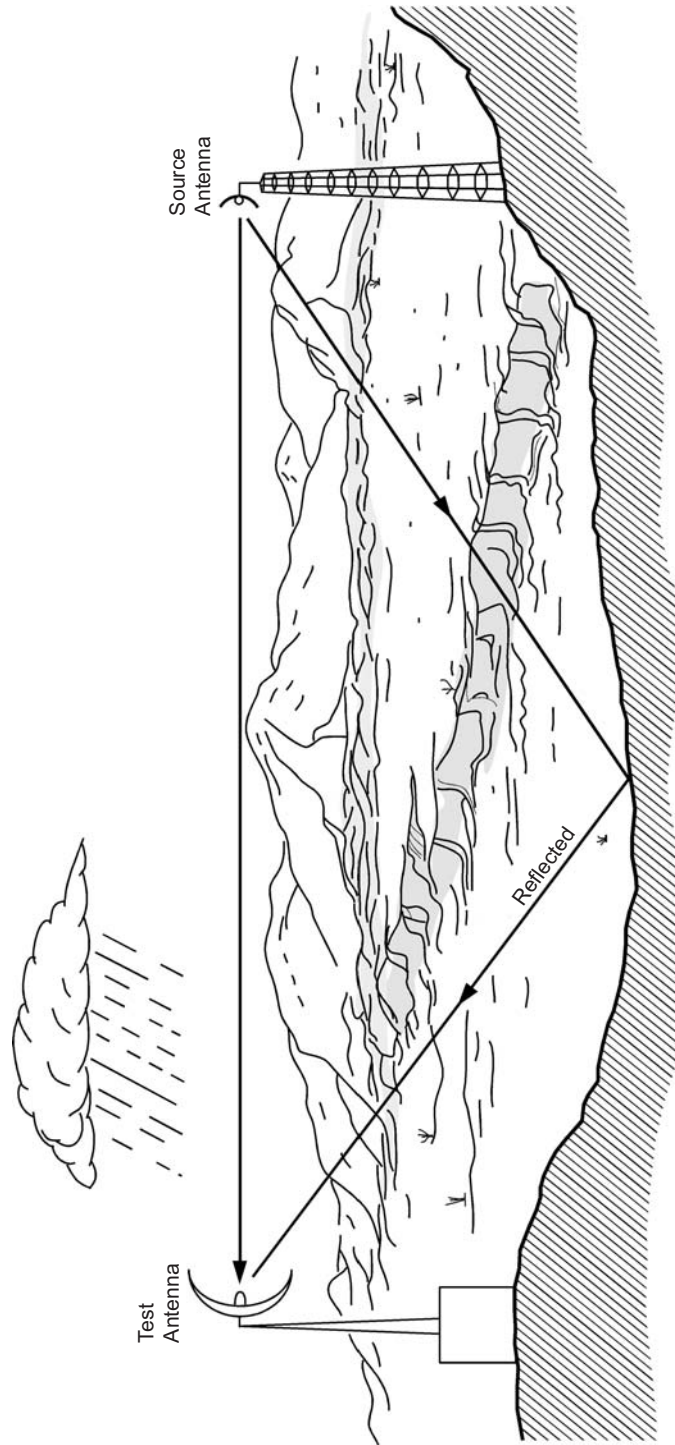


Fig. 1-34. Typical far-field antenna range.

eliminate reflections from the ground by using screens or by taking measurements at slightly different distances (separated by multiples of $\frac{1}{4}\lambda$). Alternatively, one can use geography to advantage. By placing the source antenna and the AUT on the sides of a hill, one will be able to reduce the ground reflections by as much as 60 dB.

Modern antenna ranges include the capability to rotate the AUT in the presence of the transmitted wave, detect the signal, and record the data in digital form. The antenna engineer will then display the data as the power versus direction in an appropriate coordinate system for the AUT. Throughout this book there will be examples of measured radiation patterns describing the performance of various antennas.

Given that the antenna test range has been properly constructed and that any extraneous objects are not within the field of view of either the test antenna or the AUT, the “free-space” far-field patterns can be measured. The term free-space refers to the performance of the AUT when not perturbed by any other object. After the antenna is characterized, the antenna engineer will often have to estimate the effects of the surrounding equipment, including the spacecraft body itself or booms, masts, and other antennas.

Finally, a careful comparison of the measurements of a particular antenna before and after an event can be useful in identifying if the event affected the antenna. Typical events for a spacecraft antenna include thermal tests, vibration tests, acoustic tests, launch pressure profile tests, among others. Careful measurement of antenna patterns is required to properly qualify an antenna for space flight.

1.5.1.2 Gain. Here we assume that the reader is familiar with the concept of antenna gain. There are two basic types of gain measurements. The first is an absolute gain measurement where no prior knowledge of the gain of any antenna in the measurement is required. The second is a gain transfer measurement requiring knowledge of the gain of at least one of the antennas, called a “standard gain antenna.” Sometimes this second method is referred to as a gain-comparison method.

If two antennas having gains of G_a and G_b , are separated by a distance R , then the power received at one antenna as transmitted by the other is given by Friis’ transmission formula as:

$$P_{rB} = P_{tA} G_A G_B \left(\frac{\lambda}{4\pi R} \right)^2 \quad (1.5-1)$$

It is sometimes useful to express this equation in decibels (dB) by taking the appropriate logarithms. Then, Eq. (1.5-1) can be written as:

$$P_{rb} = P_{ta} + g_a + g_b - SL \quad (1.5-2)$$

where the powers and gains are $p_r = 10\log_{10}(P_r)$, $p_t = 10\log_{10}(P_t)$, $g_a = 10\log_{10}(G_A)$, $g_b = 10\log_{10}(G_B)$, and the SL is the term that relates to the separation distance and is given by $SL = 20\log_{10}(4\pi R/\lambda)$. Note that the SL term is the reciprocal of the factor in Eq. (1.5-1). The literature refers to this as the space loss, or the loss in signal due to the distance between the transmitter and receiver. Therefore, in Eq. (1.5-2) the negative sign for space loss is used to suggest a loss in power.

By measuring the received power between a pair of antennas, one can use these equations to determine the gain of the antenna under test. In Eq. (1.5-1) it is assumed that the two antennas are perfectly matched to the transmission lines connecting their receiver and transmitter and that each is of exactly the same polarization. This equation and the subsequent development of gain measurement can be done with these factors included. The following describes the most commonly used gain measurement techniques used.

1.5.1.2.1 Substitution (Two-Antenna Technique). There are two useful versions of the two-antenna technique. In one case, in which the AUT and the source antennas are the same, the gain is calculated from the direct measurements. In this case, no knowledge of the gain of either antenna is required. Another case is where one knows very accurately the gain of one of the antennas. This is often referred to as the “standard gain antenna” (SGA). Usually, some other method (see the three-antenna technique below) is used to determine the gain of the SGA.

If the two antennas are identical, then G_A and G_B are equal. In this case Eq. (1.5-2) simplifies, and the gain of either antenna is given in decibels by:

$$g_a = g_b = \frac{1}{2}(p_r - p_t - SL) \quad (1.5-3)$$

This technique is simple in principle; however, it can be difficult in practice to implement. Small differences in the antenna manufacture also reflect in gain-measurement errors. As always, proper care should be given to the range and proper correction for errors.

The two-antenna substitution method is nearly as simple as above, with the exception that the standard gain antenna must be calibrated by some other technique. A calculation (as opposed to measurement) of the gain is also possible if the antenna is simple in nature, for example that of a horn antenna. In this case, the gain of the AUT is measured directly and calculated by rearranging either Eq. (1.5-1) or Eq. (1.5-2) as appropriate. Here Eq. (1.5-2) is used to yield the gain of the AUT.

$$g_b = p_r - (p_t + g_a - SL) \quad (1.5-4)$$

1.5.1.2.2 Three-Antenna Technique. The measurement of gain using the three-antenna technique is similar to the two-antenna technique. However, in this technique no two antennas need be the same. The measured parameters are such that one can solve for the gain of all three antennas without the knowledge of any one antenna. A generalized three-antenna method has been described that even accounts for the finite separation distance between the antennas [94] allowing for measurements to be done at less than the requisite far-field distance. This method of measuring gain consists of three separate measurements similar to that of the two-antenna method. In particular, measurements are made with each possible pair of antennas. For each measurement, Eq.(1.5-2) can be written. Subsequently, a system of three equations and three unknowns is developed for which any one of many methods can be used to solve for the individual antenna gains. For this technique the measurements can be expressed in the following equations:

$$\begin{aligned} g_a + g_b &= p_{rb} - p_{ta} + SL \\ g_a + g_c &= p_{rc} - p_{ta} + SL \\ g_b + g_c &= p_{rc} - p_{tb} + SL \end{aligned} \quad (1.5-5)$$

This set of equations can be cast in matrix form as:

$$\begin{bmatrix} 1 & 1 & 0 \\ 1 & 0 & 1 \\ 0 & 1 & 1 \end{bmatrix} \begin{bmatrix} g_a \\ g_b \\ g_c \end{bmatrix} = \begin{bmatrix} p_{rb} - p_{ta} + SL \\ p_{rc} - p_{ta} + SL \\ p_{rc} - p_{tb} + SL \end{bmatrix} \quad (1.5-6)$$

1.5.1.2.3 Polarization. The polarization characteristics of an antenna are important to know prior to using it in a communications link. The coupling of an antenna with the free-space wave is at a maximum when each shares the same polarization. Polarization of an elliptical wave includes the sense and the tilt angle. For elliptically polarized antennas, both the sense of polarization and the axial ratio are important. Both sense and polarization can be measured in one of several ways. The simplest way to measure the polarization as a function of direction is to use a linearly polarized antenna that is spinning around the polarization axis. When such a signal is received by the AUT, the measured signal will describe an envelope of polarization. Several examples of this type of measurement are given elsewhere in the book. Other measures of polarization are possible and are described in [93].

1.5.1.2.4 Input Impedance. Modern network analyzers make simple the measurement of impedance. Prior to that, other techniques were used including slotted lines and systems of couplers and power meters.

1.5.2 Near-Field Measurements

The basis of this technique is that the measured fields on a closed surface surrounding the antenna under test can be related to the far-field patterns, gain, and polarization by a Fourier transform-type relationship. See for example Fig. 1-35. If the tangential field is known on a closed surface S , then the field anywhere external to S is given by

$$\begin{aligned} \vec{E}(\vec{R}) = \int_S \int \left\{ j\omega\mu_0 [\hat{n} \times \vec{H}(\vec{R}')] \cdot \vec{G}(\vec{R}', \vec{R}) \right. \\ \left. + [\hat{n} \times \vec{E}(\vec{R}')] \cdot \nabla' \times \vec{G}(\vec{R}', \vec{R}) \right\} ds' \end{aligned} \quad (1.5-7)$$

where

- $\vec{E}(\vec{R})$ is the electric field at \vec{R}
- $\vec{H}(\vec{R})$ is the magnetic field at \vec{R}
- \hat{n} is the unit normal
- $\vec{G}(\vec{R}', \vec{R})$ is the Green's function

Theoretically, the far field of an antenna can be calculated from measurements over any arbitrary surface surrounding an antenna; however, it is advantageous to select a surface for which the relationship between the near field and the far field can be easily determined. Typically, measurements are

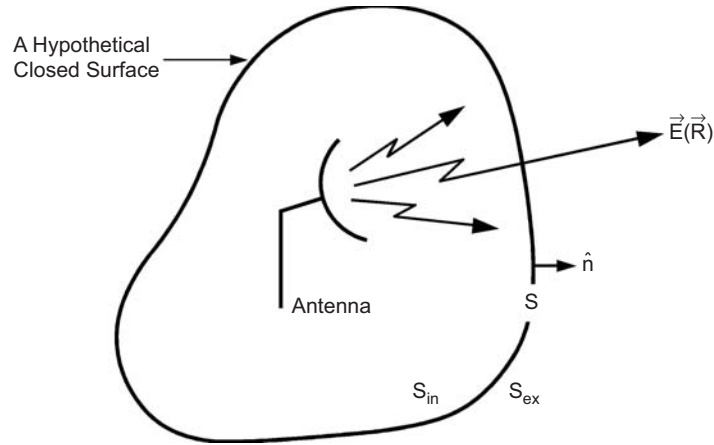


Fig. 1-35. Generalized Huygens theorem.

made over either a planar, a cylindrical, or a spherical surface as illustrated in Fig. 1-36. Early development [95–98] of this indirect technique for planar measurements suggested that very accurate measurements could be made. By the mid 1980s, near-field measurements became popular due to the fact that

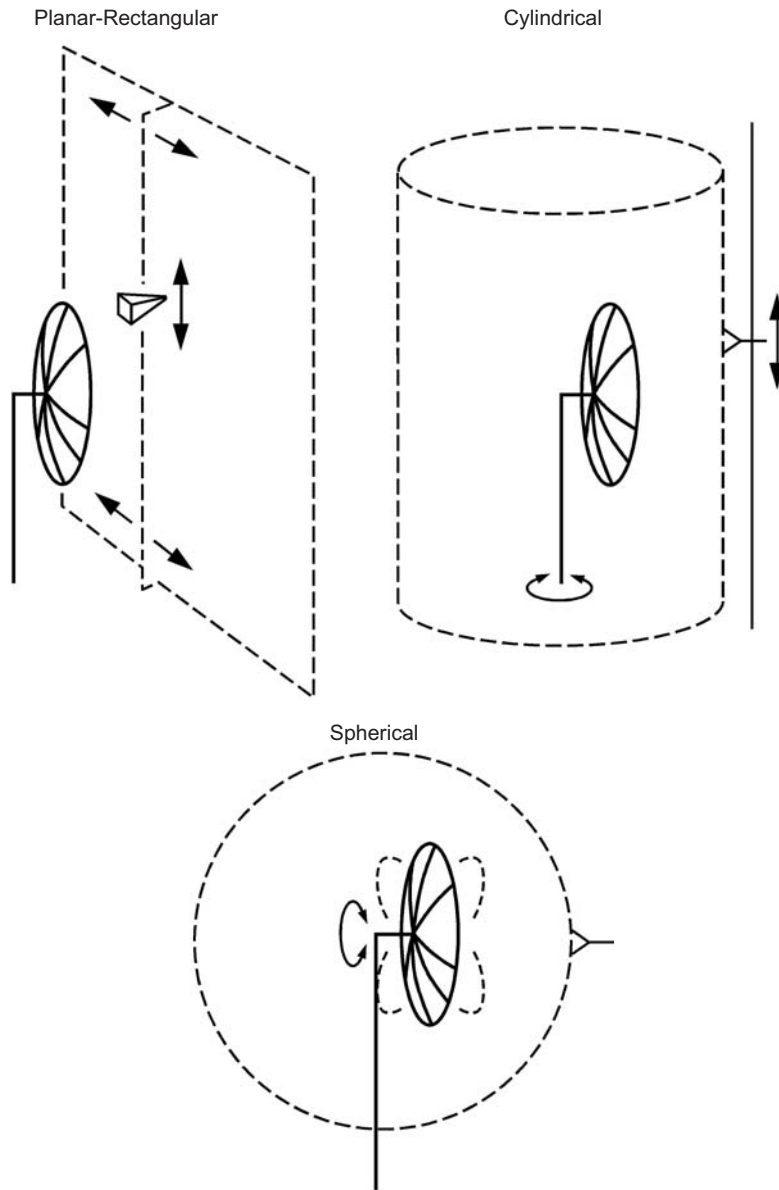


Fig. 1-36. Conventional mechanical setups for near-field measurements.

most ranges were indoors, lending themselves to the measurement of delicate or even classified antennas. Many developments were made during this time [99,100] during which JPL made the first deep-space spacecraft antenna calibrations using a near-field range [101]. Also during this time, the collection of many of these techniques was published in a special issue of the IEEE Transactions on Antennas and Propagation [102]. Note that both a Cartesian and a polar coordinate system of measurement have been developed for the planar measurement system. Even the use of Cartesian formulations using data measured on plane-polar ranges was developed [103]. Also, while planar near-field measurements were the most popular, being the most developed, there was a need for cylindrical near-field measurements as well. As a result JPL developed a cylindrical near-field range to augment its plane-polar facility [104] and measured the NASA Scatterometer and SeaWinds antenna performances [105,106]. Of these three types of surfaces, only the spherical surface can provide a complete near-field measurement. Measurements of the near field of an antenna on a planar or cylindrical surface are, by their very nature, truncated measurements of the entire antenna field. This truncation will cause some error in the calculation of the far field. Much work has been done to quantify the calculated far-field error due to this truncation as well as other effects, including the effects of the probe that is used to sense the fields, and the interaction of the probe with the antenna under test. Even in the early development of near-field measurements, experimenters knew that errors and corrections were necessary [107]. Since then, there has been much development in the analysis of these truncation errors, their causes, and mitigating steps to be taken in making such measurements [108–111]. It has been demonstrated that exceptionally accurate calculations of an antenna's far-field performance can be made using near-field measurements.

1.5.2.1 Calculation of Far-Field Patterns. The near-field measurement scheme normally consists of an AUT connected to a transmitter and a small probe antenna located in the near field of the AUT that samples the resulting electric and magnetic fields, \bar{E}_a and \bar{H}_a . Application of the Lorentz reciprocity theorem shows that the output voltage of this probe is proportional to these fields. Also, it can be shown that the relation between the motion of the probe and the antenna is a convolution expression of the probe fields and the antenna fields. Finally, for the case of an open-ended waveguide probe sensitive to the magnetic field, an expression can be written to relate the apparent induced current given by $\bar{q}_m(\bar{\rho}') = 2\hat{n} \times \bar{H}_a$ as defined in the scan plane to an integration integral, which is in the form of a Fourier transform as given in Eq. 1.5-7 [99,103]. This radiation integral can be written in any of several coordinate systems depending on the scanning motion of the probe with respect to the AUT. Many spacecraft microwave antennas lend themselves to a planar

measurement system. There are two planar coordinate systems frequently used; the polar and Cartesian systems. The plane-polar geometry is shown in Fig. 1-37. The probe moves along the x -axis, and the antenna rotates on the z -axis to measure a set of ring data at various radii from the center of the antenna.

In the plane-polar system, the radiation integral can be written by:

$$\vec{T}(\theta, \phi) = \int_{-\infty}^{\infty} \int_{-\infty}^{\infty} \overline{q_m(\rho')} e^{jk(\hat{r} \cdot \overline{\rho'})} \rho \delta \rho \delta \phi \quad (1.5-8)$$

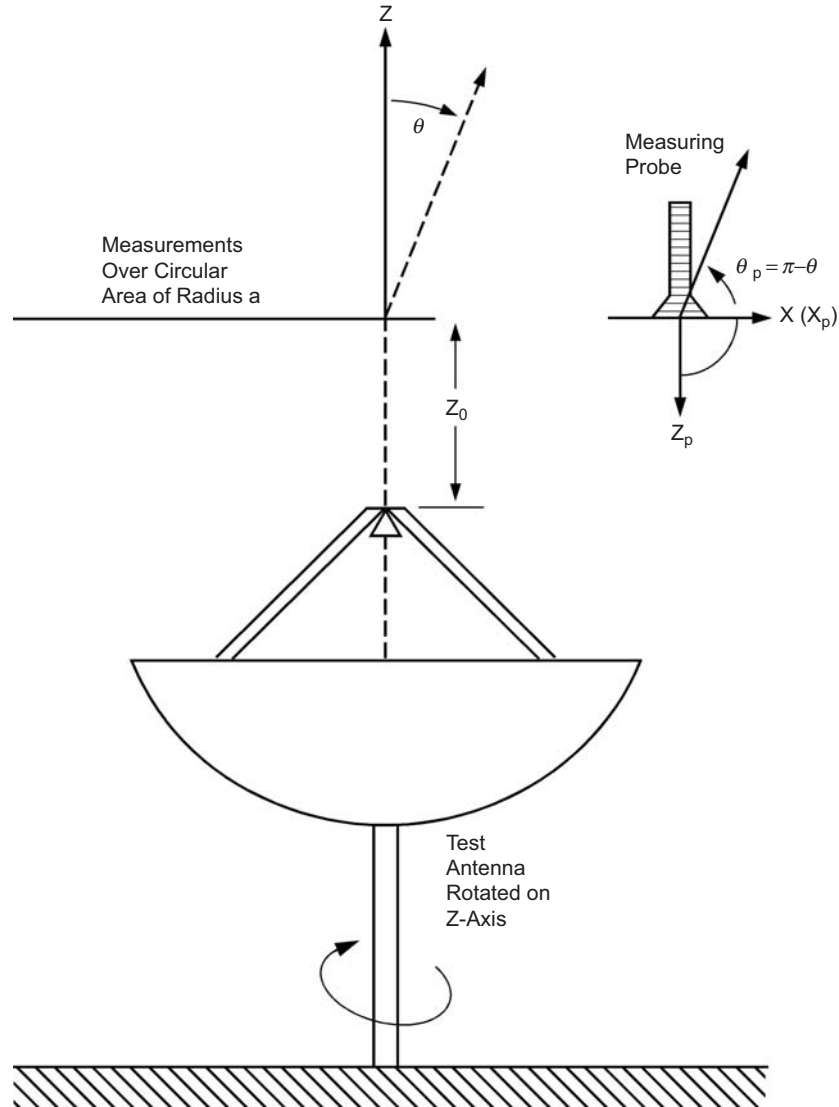


Fig. 1-37. Plane polar geometry.

Given that the measured data are from a plane-polar measurement, the numerical solution to Eq. 1.5-8 can be most readily be solved using the Jacobi-Bessel expansion of the integrand. The resulting expressions yield a set of coefficients for which the integrand is replaced by a summation given by:

$$\begin{aligned} \vec{T}(\theta, \phi) = 2\pi a^2 \sum_n \sum_m \left[\bar{C}_{nm} \cos n\phi + \bar{D}_{nm} \sin n\phi \right] \\ \times \sqrt{2(n+2m+1)} \frac{J_{n+2m+1}(ka \sin \theta)}{ka \sin \theta} \end{aligned} \quad (1.5-9)$$

where J is the Bessel function and one chooses n and m such that the resulting summation converges in the angular region of interest. This simple summation is used for all angles θ, ϕ . This suggests that, once the coefficients are calculated, all pattern information can be rapidly calculated for many directions. The calculation of the coefficients is where the time-consuming computations occur. These coefficients are given by

$$\bar{C}_{nm} = \frac{\varepsilon_n}{2\pi} \int_0^1 \int_0^{2\pi} \bar{Q}(\bar{a}s') \cos n\phi F_m^n(s') s' d\phi' ds' \quad (1.5-10)$$

$$\bar{D}_{nm} = \frac{\varepsilon_n}{2\pi} \int_0^1 \int_0^{2\pi} \bar{Q}(\bar{a}s') \sin n\phi F_m^n(s') s' d\phi' ds' \quad (1.5-11)$$

where ε is the Neumann factor (1 for $n = 0, 2$ otherwise) and s' is ρ'/a .

1.5.2.2 Measurement of Gain. Measurement of gain using near-field techniques can be done in either of two ways. One technique uses a substitution method very similar to that described in the far-field gain measurement where a second antenna of known gain is also measured by near-field techniques, and a comparison of the peak fields is done. For this technique, no knowledge of the probe antenna characteristics is required. Another substitution technique uses the knowledge of the probe gain and the loss of the transmission line to make a direct measure of the gain. This is done by removing the transmission line between the transmitter and the probe and in the lab using a variable attenuator to duplicate power levels found in the near-field measurement. The gain is determined directly from the settings of the attenuator. These techniques have been described in detail for near-field measurements using any of the typical coordinate systems.

1.5.2.3 The JPL Near-field Ranges

1.5.2.3.1 The Plane-Polar Range. A plane-polar near-field range was developed in the early 1980s and first used for the Galileo project high-gain

antenna test program [99,101]. The plane-polar technique, together with the series expansion algorithm, has a number of important mechanical and computational features.

The mechanical features can be readily inferred from the geometry shown in Fig. 1-37. The advantages of the plane-polar geometry are that both the probe and the antenna are gravitationally balanced and that the probe only moves in one direction. This allows for larger antennas for the same near-field facility than the planar-rectangular geometry. Also, the antennas always point in the same direction, which can be skyward. This is especially important for the measurement of gravitationally sensitive lightweight spacecraft antennas. Thus, this geometry is very suitable for high-gain reflector-type spacecraft antennas.

From the use of the Jacobi-Bessel series expansion from the plane-polar geometry, the following computational features apply:

- 1) Plane-polar data are used directly without interpolation in a rectangular grid.
- 2) The Jacobi-Bessel series computations require numerical manipulations proportional to N for N data and N observation points.
- 3) The numerical value of N that is required is determined only by the informational content of the measured field. No aliasing errors are introduced no matter how sparsely spaced the data points are located, and no zero fill is required.
- 4) The value of N can be substantially reduced by taking full advantage of any rotational symmetry in the antenna patterns.
- 5) The choice and number of observation points are not constrained.
- 6) The integrations involved can be performed piecewise over the aperture plane with no added complexity. Thus, large quantities of data can be readily handled.
- 7) Once the far field is computed at one observation point, it can be determined at any other observation point with relatively little effort.

For the early use of near-field ranges, it was extremely important to verify that the computation of the far-field patterns from near-field data actually matched the data measured on a far-field range. The first verification of this with the JPL plane-polar range was made using the 1.47-m Viking high-gain antenna (HGA). The Viking antenna was first measured on a far-field range and then measured in the plane-polar near-field range (see Fig. 1-38). The comparison of the direct far-field measurement and the constructed far field from the near-field measurement is shown in Fig. 1-39. As can be seen in the figure, there is good agreement, validating the use of the near-field range. Subsequently, the Galileo HGA performance was verified by near-field measurements in the plane polar near-field facility [101].



Fig. 1-38. Viking spacecraft HGA in the near-field facility.

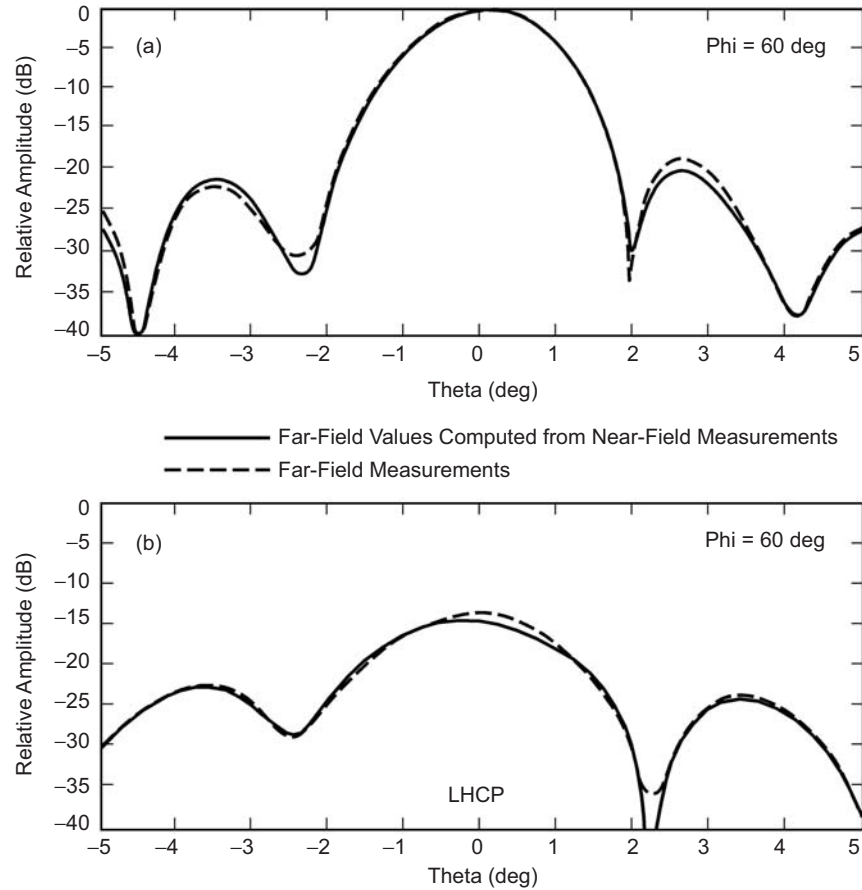


Fig. 1-39. Far-field patterns of the circular-polarized Viking HGA at X-band: (a) RHCP and (b) LHCP.

1.5.2.3.2 Cylindrical Range. Several of JPL's instrument antennas to be described in Chapter 7 (NSCAT, SeaWinds Radar Antenna, and Wide Swath Ocean Altimeter) have a very long slender footprint and are best measured in the near field using a cylindrical rather than a planar geometry. Consequently, a cylindrical near-field scanning range [104–106,110,111] was assembled at JPL and used in the measurement of these antennas.

1.5.3 Conclusions

Regardless of the method chosen to characterize an antenna, such characterization is paramount in validating the performance of the antenna. Telecommunications systems engineers develop their system with specific performance expectations and associated tolerances. Verification of the performance assures the telecommunications system engineer that adequate

margin will exist over the life of the mission. The accuracy with which the performance is known is sometimes even more important than the actual performance itself. Antennas in instrument systems often fall into this category. The gain defines the total sensitivity; however, the precision is often affected by the total accuracy in performance prediction. This chapter has exposed some of the methods available to the antenna engineer to provide this validation. The amount of literature available to support antenna measurements seems limitless, possibly because of the importance placed on the activity. Research into the available methods for antenna measurements, development of the test facility to support the measurements, validation of the test facility, and a thorough analysis of the potential errors is mandatory prior to the measurement of any antenna. Only then will the final results of a validation and verification program be full acceptable.

References

- [1] W. A. Imbriale, *Large Antennas of the Deep Space Network*, John Wiley & Sons, Inc., Hoboken, New Jersey, 2003.
- [2] C. D. Edwards, Jr. and F. M. Naderi, "Telecommunications and Navigation Strategies for Mars Exploration," *52nd International Astronautical Congress*, Toulouse, France, 1–5 October 15, 2001, IAF-01-M.4.08, International Astronautical Federation, Paris, France, 2001.
- [3] C. D. Edwards, J. T. Adams, D. J. Bell, R. Cesarone, R. DePaula, J. F. Durning, T. A. Ely, R. Y. Leung, C. A. McGraw, and S. N. Rosell, "Strategies for Telecommunications and Navigation in Support of Mars Exploration," *Acta Astronautica*, vol. 48, issue 5-12, pp. 661–668, March–June 2001.
- [4] *Recommendation for Space Data Systems Standards, Proximity-1 Space Link Protocol–Physical Layer*, CCSDS 211.1-B-1, Consultative Committee for Space Data Systems, Matera, Italy, April 2003.
- [5] R. F. Harrington, *Time Harmonic Electromagnetic Fields*, McGraw-Hill, New York, New York, 1961.
- [6] W. V. T. Rusch and P. D. Potter, *Analysis of Reflector Antennas*, Academic Press, New York, New York, 1970.
- [7] W. A. Imbriale and R. E. Hodges, "Linear-Phase Approximation in the Triangular Facet Near-Field Physical Optics Computer Program," *Telecommunications and Data Acquisition Progress Report 42-102*, April–June 1990, Jet Propulsion Laboratory, Pasadena, California, pp. 47–56, August 15, 1990.
http://ipnpr.jpl.nasa.gov/progress_report/issues.html

- [8] W. A. Imbriale and R. E. Hodges, "The Linear Phase Triangular Facet Approximation in Physical Optics Analysis of Reflector Antennas," *Applied Computational Electromagnetic Society*, vol. 6, no. 2, pp. 74–85, Winter 1991.
- [9] S. W. Lee and R. Mittra, "Fourier Transform of a Polygonal Shape Function and Its Application in Electromagnetics," *IEEE Transactions on Antennas and Propagation*, vol. 31, no. 1, pp. 99–103, January 1983.
- [10] Y. Rahmat-Samii, "Useful Coordinate Transformations for Antenna Applications," *IEEE Transactions on Antennas and Propagation*, vol. 27, pp. 571–574, July 1979.
- [11] J. R. Withington, W. A. Imbriale, and P. Withington, "The JPL Beamwaveguide Test Facility," *Antennas and Propagation Society Symposium*, London, Ontario, Canada, pp. 1194–1197, June 24–28, 1991.
- [12] P. D. Potter, "A New Horn Antenna with Suppressed Sidelobes and Equal Beamwidths," *Microwave Journal*, pp. 71–78, June 1963.
- [13] S. A. Brunstein, "A New Wideband Feed Horn with Equal E- and H-plane Beamwidths and Suppressed Sidelobes," *Space Programs Summary 37-58, Vol. II, The Deep Space Network*, Jet Propulsion Laboratory, Pasadena, California, pp. 61–64, July 1969.
- [14] D. Hoppe, "Scattering Matrix Program for Circular Waveguide Junctions," *Cosmic Software Catalog*, NASA-CR-179669, NTO-17245, National Aeronautics and Space Administration, Washington, D.C., 1987.
- [15] D. Hoppe, "Modal Analysis Applied to Circular, Rectangular, and Coaxial Waveguides," *Telecommunications and Data Acquisition Progress Report 42-95, July–September 1988*, Jet Propulsion Laboratory, Pasadena, California, pp. 89–96, November 15, 1988.
http://ipnpr.jpl.nasa.gov/progress_report/issues.html
- [16] D. J. Hoppe, W. A. Imbriale, and A. M. Bhanji, "The Effects of Mode Impurity on Ka-Band System Performance," *Telecommunications and Data Acquisition Progress Report 42-80, October–December 1984*, Jet Propulsion Laboratory, Pasadena, California, pp. 12–23, February 15, 1985.
http://ipnpr.jpl.nasa.gov/progress_report/issues.html
- [17] G. L. James, "Analysis and Design of TE_{11} and HE_{11} , Corrugated Cylindrical Waveguide Mode Converters," *IEEE Transactions on Microwave Theory and Techniques*, vol. MTT-29, pp. 1059–1066, October 1981.
- [18] S. Silver, *Microwave Antenna Theory and Design*, Radiation Laboratory Series, vol. 12, McGraw-Hill, New York, New York, pp. 336–338, 1949.

- [19] A. C. Ludwig, "Radiation Pattern Synthesis for Circular Aperture Horn Antennas," *IEEE Transactions on Antennas and Propagation*, vol. AP-14, pp. 434–440, July 1966.
- [20] P. H. Stanton, D. J. Hoppe, and H. Reilly, "Development of a 7.2-, 8.4-, and 32-Gigahertz (X-/X-/Ka-Band) Three-Frequency Feed for the Deep Space Network," *Telecommunications and Mission Operations Progress Report 42-145, January–March 2001*, Jet Propulsion Laboratory, Pasadena, California, pp. 1–20, May 15, 2001.
http://ipnpr.jpl.nasa.gov/progress_report/issues.html
- [21] A. C. Ludwig, "Spherical Wave Theory," section in *Handbook of Antenna Design* (A. W. Rudge, K. Milne, A. D. Olver, and P. Knight, editors), Peter Peregrinus, Limited, London, England, 1982.
- [22] A. C. Ludwig, *Calculation of Scattered Patterns from Asymmetrical Reflectors*, Ph.D. dissertation, University of Southern California, Los Angeles, 1969. Also Technical Report 32-1430, Jet Propulsion Laboratory, Pasadena, California, February 1970.
- [23] V. Galindo, "Design of Dual-Reflector Antennas with Arbitrary Phase and Amplitude Distributions," *IEEE Transactions on Antennas and Propagation*, vol. AP-12, pp. 403–408, July 1964.
- [24] W. F. Williams, "High Efficiency Antenna Reflector," *Microwave Journal*, vol. 8, pp. 79–82, July 1966.
- [25] V. Galindo-Israel, W. A. Imbriale, and R. Mittra, "On the Theory and Synthesis of Single and Dual Offset Shaped Reflector Antennas," *IEEE Transactions on Antennas and Propagation*, vol. AP-35, no. 8, pp. 887–896, August 1987.
- [26] V. Galindo-Israel, W. A. Imbriale, R. Mittra, and K. Shogen, "On the Theory of the Synthesis of Offset Dual-Shaped Reflectors—Case Examples," *IEEE Transactions on Antennas and Propagation*, vol. 39, no. 5, pp. 620–626, May 1991.
- [27] A. G. Cha, "The JPL 1.5-meter Clear Aperture Antenna with 84.5 Percent Efficiency," *Telecommunications and Data Acquisition Progress Report 42-73, January–March 1983*, Jet Propulsion Laboratory, Pasadena, California, pp. 1–14, May 15, 1983.
http://ipnpr.jpl.nasa.gov/progress_report/issues.html
- [28] V. D. Agrawal and W. A. Imbriale, "Design of a Dichroic Cassegrain Subreflector," *IEEE Transactions on Antennas and Propagation*, vol. AP-27, pp. 466–473, July 1979.
- [29] J. P. Montgomery, "Scattering by an Infinite Periodic Array on Thin Conductors on a Dielectric Sheet," *IEEE Transactions on Antennas and Propagation*, vol. AP-23, pp. 70–75, January 1975.

- [30] V. Galindo, N. Amitay, and C. P. Wu, *Theory and Analysis of Phased Array Antennas*, Wiley-Interscience, New York, New York, 1972.
- [31] W. A. Imbriale, V. Galindo, and Y. Rahmat-Samii, "On the Reflectivity of Complex Mesh Surfaces," *IEEE Transactions on Antennas and Propagation*, vol. AP-39, pp. 1352–1365, September 1991.
- [32] R. F. Harrington, *Field Computations by Moment Methods*, The Macmillan Company, New York, New York, 1968.
- [33] W. A. Imbriale and P. G. Ingerson, "On Numerical Convergence of Moment Solutions of Moderately Thick Wire Antennas using Sinusoidal Basis Functions," *IEEE Transactions on Antennas and Propagation*, vol. AP-21, pp. 363–366, May 1973.
- [34] W. A. Imbriale, "Applications of the Method of Moments to Thin-Wire Elements and Arrays," Chapter 2 in *Topics in Applied Physics*, vol. 3, *Numerical and Asymptotic Techniques in Electromagnetics*, Editor: R. Mittra, Springer-Verlag, Berlin, Germany, and New York, New York, 1975.
- [35] G. A. Deschamp, "Microstrip microwave antennas," *Proceedings of the Antenna Applications Symposium*, Robert Allerton Park, Monticello, Illinois, University of Illinois, [no page numbers in proceedings], September 1953.
- [36] H. Gutton and G. Baissinot, "Flat Aerial for Ultra High Frequencies," French patent No. 703113, 1955.
- [37] R. E. Munson, "Conformal microstrip antennas and microstrip phased arrays," *IEEE Transactions on Antennas and Propagation*, vol. AP-22, pp. 74–78, January 1974.
- [38] K. R. Carver and J. W. Mink, "Microstrip antenna technology," *IEEE Transactions on Antennas and Propagation*, vol. AP-29, pp. 2–24, January 1981.
- [39] R. J. Mailloux, J. McIlvenna, and N. Kernweis, "Microstrip array technology," *IEEE Transactions on Antennas and Propagation*, vol. AP-29, pp. 25–38, January 1981.
- [40] J. Q. Howell, "Microstrip antenna," *IEEE Transactions on Antennas and Propagation*, vol. AP-23, pp. 90–93, January 1975.
- [41] A. G. Derneryd, *Linear microstrip array antennas*, Tech. Rep. 7505, Chalmers University of Technology, Goteborg, Sweden, October 1975.
- [42] J. L. Kerr, "Microstrip polarization techniques," *Proceedings of the Antenna Applications Symposium*, Robert Allerton Park, Monticello, Illinois, University of Illinois, [no page numbers in proceedings], September 1953.

- [43] J. Huang, "Microstrip antennas for commercial applications," *Microstrip Antennas*, D. M. Pozar and D. H. Schaubert, editors, IEEE Press, Piscataway, New Jersey, pp. 371–379, 1995.
- [44] I. J. Bahl and P. Bhartia, *Microstrip Antennas*, Artech House, Dedham, Massachusetts, 1980.
- [45] J. R. James and P. S. Hall, *Handbook of Microstrip Antennas*, Peter Peregrinus Limited, London, England, 1989.
- [46] D. M. Pozar, "Microstrip antenna aperture-coupled to a microstripline," *Electronics Letters*, vol. 21, pp. 49–50, January 1985.
- [47] L. Murphy, "Seasat and SIR-A microstrip antennas," *Proceedings of the Workshop on Printed Circuit Antenna Technology* (Las Cruces, New Mexico), paper 18, October 1979.
- [48] J. Huang, M. Lou, B. C. Lopez, and E. Gama, "Foldable Frame-Supported Thin-Membrane Array," *Proceedings of the International Symposium on Antennas and Propagation (ISAP)*, Institute of Electronics, Information and Communications Engineers, Fukuoka, Japan, pp. 213–216, August 2000.
- [49] S. A. Long and M. D. Walton, "A Dual-Frequency Stacked Circular Disc Antenna," *IEEE Transactions on Antennas and Propagation*, vol. AP-27, pp. 270–273, March 1979.
- [50] S. S. Zhong and Y. T. Lo, "Single-Element Rectangular Microstrip Antenna for Dual-Frequency Operation," *Electronics Letters*, vol. 19, pp. 298–300, 1983.
- [51] J. L. Kerr, "Terminated Microstrip Antenna," *Proceedings of the Antenna Applications Symposium*, Robert Allerton Park, Monticello, Illinois, University of Illinois [no page numbers in proceedings], September 1978.
- [52] J. Huang, "Microstrip reflectarray," *IEEE AP-S/URSI Symposium* (London, Ontario, Canada, June 1991), pp. 612–615, 1991.
- [53] F. Crog and D. M. Pozar, "Millimeter Wave Design of Wideband Aperture Coupled Stacked Microstrip Antennas," *IEEE Transactions on Antennas and Propagation*, vol. 39, pp. 1770–1776, December 1991.
- [54] R. Q. Lee, K. F. Lee, and J. Bobinchak, "Characteristics of a Two-Layer Electromagnetically Coupled Rectangular Patch Antenna," *IEEE Transactions on Antennas and Propagation*, vol. AP-38, pp. 1298–1302, August 1990.
- [55] H. F. Pues and A. R. Van De Capelle, "An Impedance-Matching Technique for Increasing the Bandwidth of Microstrip Antennas," *IEEE Transactions on Antennas and Propagation*, vol. AP-37, pp. 1345–1354, November 1989.

- [56] T. Teshirogi, M. Tanaka, and W. Chujo, "Wideband Circularly Polarized Array with Sequential Rotation," *Proceedings of the International Symposium on Antennas and Propagation (ISAP)*, Institute of Electronics, Information and Communications Engineers, Fukuoka, Japan, pp. 117–120, August 1985.
- [57] J. Huang, "A Technique for an Array to Generate Circular Polarization with Linearly Polarized Elements," *IEEE Transactions on Antennas and Propagation*, vol. AP-34, pp. 1113–1123, 1986.
- [58] D. H. Schaubert and F. G. Farrar, "Some Conformal Printed Circuit Antenna Designs," *Proceedings of the Workshop on Printed Circuit Antenna Technology* (State University Las Cruces, New Mexico), pp. 5/1–5/21, October 1979.
- [59] K. F. Lee, K. M. Luk, K. F. Tong, and T. Huyuh, "Experimental Study of the Rectangular Patch with a U-Shaped Slot," *1996 International IEEE Antennas and Propagation Symposium Digest* (Baltimore, Maryland), vol. 1, pp. 10–13, 1996.
- [60] C. L. Mak, K. M. Luk, K. F. Lee, and Y. L. Chow, "Experimental Study of a Microstrip Antenna with an L-Shaped Probe," *IEEE Transactions on Antennas and Propagation*, vol. 48, pp. 777–783, May 2000.
- [61] H. Howe, Jr., "Stripline Is Alive and Well," *Microwave Journal*, vol. 14, p. 25, July 1971.
- [62] R. Woo, *Final Report on RF Voltage Breakdown in Coax Transmission Lines*, JPL Technology Report 32-1500, Jet Propulsion Laboratory, Pasadena, California, October 1970.
- [63] J. Huang, "A Parallel-Series-Fed Microstrip Array with High Efficiency and Low Cross-Polarization," *Microwave and Optical Technology Letters*, vol. 5, pp. 230–233, May 1992.
- [64] *Radiation Resistance of Teflon in a Simulated Space Environment*, TM-6871, Components and Material Laboratory, Hughes Aircraft Company, August 1961.
- [65] "Radiation Tolerance of Teflon Resins," *The Journal of Teflon*, vol. 10, no. 1, Dupont Company, January–February 1969.
- [66] W. A. Campbell, Jr. and R. S. Marriott, *Outgassing Data for Selecting Spacecraft Materials*, NASA Reference Publication 1124, National Aeronautics and Space Administration, Washington, District of Columbia, August 1987.
- [67] "Standard Test Method for Total Mass Loss and Collected Volatile Condensable Materials from Outgassing in a Vacuum Environment," *Annual Book of Standards*, ANSI/ASTM E595-77, American Society for Testing and Materials, West Conshohocken, Pennsylvania, pp. 1–8, 1980.

- [68] R. K. Kirby, "Thermal Expansion of PTFE Teflon from -190 to 300°C," *Journal of Research of the National Bureau of Standards*, vol. 57, pp. 91–94, 1965.
- [69] A. G. Derneryd, "A Theoretical Investigation of the Rectangular Microstrip Antenna," *IEEE Transactions on Antennas and Propagation*, vol. AP-26, pp. 532–535, July 1978.
- [70] H. Pues and A. Van de Capelle, "Accurate Transmission-Line Model for the Rectangular Microstrip Antenna," *Proceedings of the IEE*, vol. 131, part H, pp. 334–340, December 1984.
- [71] W. F. Richards, Y. T. Lo, and D. Harrison, "An Improved Theory for Microstrip Antennas and Applications," *Transactions on Antennas and Propagation*, vol. AP-29, pp. 38–46, January 1981.
- [72] M. D. Deshpande and M. C. Bailey, "Input Impedance of Microstrip Antennas," *IEEE Transactions on Antennas and Propagation*, vol. AP-31, pp. 740–747, September 1983.
- [73] D. M. Pozar, "Input Impedance and Mutual Coupling of Rectangular Microstrip Antennas," *IEEE Transactions on Antennas and Propagation*, vol. AP-30, pp. 1191–1196, November 1982.
- [74] I. E. Rana and N. G. Alexopoulos, "Current Distribution and Input Impedance of Printed Dipoles," *IEEE Transactions on Antennas and Propagation*, vol. AP-29, pp. 99–105, January 1981.
- [75] J. R. Mosig and F. E. Gardiol, "General Integral Equation Formulation for Microstrip Antennas and Scatterers," *Proceedings of the IEE*, vol. 132, Part H, pp. 424–432, 1985.
- [76] A. Reineix and B. Jecko, "Analysis of Microstrip Patch Antennas Using Finite Difference Time Domain Method," *IEEE Transactions on Antennas and Propagation*, vol. 37, pp. 1361–1368, November 1989.
- [77] X. Zhang and K. K. Mei, "Time-Domain Finite-Difference Approach to the Calculation of the Frequency-Dependent Characteristics of Microstrip Discontinuities," *IEEE Transactions Microwave Theory and Techniques*, vol. 36, pp. 1775–1787, 1988.
- [78] C. Wu, K. L. Wu, Z. Q. Bi, and J. Litva, "Accurate Characterization of Planar Printed Antennas Using Finite-Difference Time-Domain Method," *IEEE Transactions on Antennas and Propagation*, vol. 40, pp. 526–534, May 1992.
- [79] K. S. Yee, "Numerical Solution of Initial Boundary Value Problems Involving Maxwell's Equations in Isotropic Media," *IEEE Transactions on Antennas and Propagation*, vol. AP-14, pp. 302–307, 1966.
- [80] J. R. James, P. S. Hall, and C. Wood, *Microstrip Antenna: Theory and Design*, Peter Peregrinus, Limited, London, England, 1981.

- [81] A. G. Derneyd, "Linearly Polarized Microstrip Antennas," *IEEE Transactions on Antennas and Propagation*, vol. AP-24, pp. 846–851, November 1976.
- [82] T. Metzler, "Microstrip Series Array," *IEEE Transactions on Antennas and Propagation*, vol. AP-29, pp. 174–178, January 1981.
- [83] T.-S. Horng and N. G. Alexopoulos, "Corporate Feed Design for Microstrip Arrays," *IEEE Transactions on Antennas and Propagation*, vol. 41, pp. 1615–1624, December 1993.
- [84] D. M. Pozar, "Scanning Characteristics of Infinite Arrays of Printed Antenna Subarrays," *IEEE Transactions on Antennas and Propagation*, vol. 40, pp. 666–674, June 1992.
- [85] J. Huang, "Circularly Polarized Conical Patterns from Circular Microstrip Antennas," *IEEE Transactions on Antennas and Propagation*, vol. AP-32, pp. 991–994, September 1984.
- [86] G. Kumar and L. Shafai, "Generation of Conical Patterns from Circular Patch Antennas and Their Performance," *Canadian Electrical Engineering Journal*, vol. 10, pp. 108–112, 1985.
- [87] I. J. Bahl and D. K. Trivedi, "A Designer's Guide to Microstrip Line," *Microwaves*, pp. 174–181, May 1977.
- [88] D. M. Pozar and J. R. James, "A Review of CAD for Microstrip Antennas and Arrays," in *Microstrip Antennas*, IEEE Press, New York, D. M. Pozar and D. H. Schaubert, editors, pp. 51–56, 1995.
- [89] A. G. Brejcha, L. H. Keeler, and G. G. Sanford, "The Seasat-A Synthetic Aperture Radar Antenna," presented at *Synthetic Aperture Radar Technology Conference*, Las Cruces, New Mexico, March 1978.
- [90] H. Schaeper and H. A. Nitschke, "Spaceborne SAR Antenna Technology and the Shuttle Imaging Radar – B (SIR-B) Antenna Development," *IEEE International Radar Conference* (Arlington, Virginia), May 1985.
- [91] R. L. Jordan, B. L. Huneycutt, and M. Werner, "The SIR-C/X-SAR Synthetic Aperture Radar System," *IEEE Transactions on Geoscience and Remote Sensing*, vol. 33, pp. 829–839, July 1995.
- [92] Antenna Standards Committee, *IEEE Standard Test Procedures for Antennas*, IEEE, distributed in cooperation with Wiley, 1979.
- [93] J. S. Hollis, T. J. Lyon, L. Clayton, Jr., *Microwave Antenna Measurements*, Scientific-Atlanta, Inc., Atlanta, Georgia, 1969.
- [94] A. C. Newell, R. C. Baird, and P. F. Wacker, "Accurate Measurement of Antenna Gain and Polarization at Reduced Distances by an Extrapolation Technique," *IEEE Transactions on Antennas and Propagation*, vol. 21, pp. 418–431, July 1973.

- [95] R. C. Johnson, H. A. Ecker, and J. S. Hollis, "Determination of Far Field Antenna Pattern from Near Field Measurements," *Proceedings of the IEEE*, vol. 61, pp. 1668–1694, December 1973.
- [96] D. T. Parris, W. M. Leach, Jr., and E. B. Joy, "Basic Theory of Probe-Compensated Near-Field Measurements," *IEEE Transactions on Antennas and Propagation*, vol. 26, pp. 373–379, May 1978.
- [97] G. V. Borgiotti, "Integral Equation Formulation for Probe Corrected Far-Field Reconstruction from Measurements on a Cylinder," *IEEE Transactions on Antennas and Propagation*, vol. 26, pp. 572–578, July 1978.
- [98] D. M. Kerns, *Plane-Wave Scattering-Matrix Theory of Antennas and Antenna-Antenna Interactions*, NBS Monograph 162, United States National Bureau of Standards, June 1981.
- [99] Y. Rahmat-Samii, V. Galindo-Israel, and R. Mittra, "A Plane-Polar Approach for Far-Field Construction from Near-Field Measurements," *IEEE Transactions on Antennas and Propagation*, vol. AP-28, pp. 216–230, March 1980.
- [100] A.D. Yaghjian, "An Overview of Near-field Antenna Measurements," *IEEE Transactions on Antennas and Propagation*, vol. 34, no. 1, pp. 30–45, January 1986.
- [101] Y. Rahmat-Samii and Mark S. Gatti, "Far-Field Patterns of Spaceborne Antennas from Plane-Polar Near-Field Measurements," *IEEE Transactions on Antennas and Propagation*, vol. AP-33, no. 6, pp. 638–648, June 1985.
- [102] Special Issue on Near-Field Scanning Techniques, *IEEE Transactions on Antennas and Propagation*, vol. AP-36, no. 6, June 1998.
- [103] M. S. Gatti and Y. Rahmat-Samii, "FFT Applications to Plane-Polar Near-Field Antenna Measurements," *IEEE Transactions on Antennas and Propagation*, vol. AP-36, no. 6, pp. 146–149, June 1988.
- [104] *Efficient and Fast Reconstruction of the Far-Field Radiation pattern from Knowledge of the Near-Field on a Cylindrical Surface*, JPL Document D-9124 (internal document), Jet Propulsion Laboratory, Pasadena, California, November 8, 1991.
- [105] Z. Hussein and Y. Rahmat-Samii, "Application of Cylindrical Near-Field Measurement Technique to the Calibration of Spaceborne Radar Antennas: NASA Scatterometer and SeaWinds," *IEEE Transactions on Geoscience and Remote Sensing*, vol. 37, no. 1, January 1999.

- [106] Z. A. Hussein and Y. Rahmat-Samii, "On the Accurate Calibration of the SeaWinds Radar Antenna: A Cylindrical near-Field Measurement Approach," *International Geoscience and Remote Sensing Symposium (IGARSS) Digest* (Lincoln, Nebraska, May 27–31) vol. 1, *Technical Papers*, A96-42751 11-43, Institute of Electrical and Electronics Engineers, Inc., Piscataway, New Jersey, pp. 515–519, 1996.
- [107] D.M. Kearns, "Correction of Near-Field Antenna Measurements Made with an Arbitrary But Known Measuring Antenna," *Electronics Letters*, vol. 6, pp. 347–347, May 1978.
- [108] *Upper Bound Errors in far-field antenna parameters determined from planar near-field measurements, Part 1: Analysis*, Technical Note 667, National Bureau of Standards, Boulder, Colorado, 1975.
- [109] A. C. Newell, "Error Analysis Technique for Planar Near-Field Measurements, *IEEE Transactions on Antennas and Propagation*, vol. AP-36, pp. 754–768, June 1988
- [110] Z. Hussein and Y. Rahmat-Samii, "Cylindrical Near-Field Measurement Error Models for NASA Scatterometer Fan-Beam Array Antenna, *1992 IEEE AP-S International Antennas and Propagation Symposium Digest* (Chicago, Illinois, July 1992), pp. 1558–1561, 1992.
- [111] Z. A. Hussein and Y. Rahmat-Samii, "Probe Compensation Characterization in Cylindrical Near-Field Scanning," *IEEE AP-S International Symposium Digest* (Ann Arbor, Michigan), vol. 3, pp. 1808–1811, July 1993.